Ministero dell'Universitá e
della Ricerca

Dipartimento di Scienze
Fisiche ed Astronomiche

Universitá degli Studi
di Palermo

DIPARTIMENTO DI SCIENZE FISICHE E ASTRONOMICHE
DOTTORATO DI RICERCA IN FISICA – XXII CICLO

Structural Modification Processes in Bulk and Nano-sized Amorphous SiO_2 Systems

Gianfranco Vaccaro

Ph.D Thesis

(S.S.D FIS/01)

Palermo, Febbraio 2011

Supervisore: Dott. Simonpietro Agnello

Coordinatore: Prof. Antonio Cupane

Contents

Introduction

Amorphous silicon dioxide, or silica (a-SiO_2), has been one of the most used and investigated materials for more than 50 years. Indeed, thanks to its exceptional properties, as for example a high transparency in the visible and ultraviolet spectral regions, the low conductivity and considering its natural abundance as well as the low manufacturing costs, silica plays a determinant role in many different applicative ambits from optics, to microelectronic, to telecommunication. On the other hand, research has been motivated by the fact that silica for its simple structure is considered a model system useful to understand and deepen the general properties of amorphous materials.

The tendency of today's research toward nanotechnology has significantly increased the interest on the nanometer-sized silica materials for their potential applications in a lot of technological and scientific ambits. Indeed, nanotechnologies do not simply represent another step towards miniaturization, but they allow to build up materials with properties that often are significantly different from those of larger-size (bulk) materials with the same chemical composition. In this context, the different structural properties of the network of bulk and nanosized systems are considered a key factor in determining many fundamental properties of the amorphous materials. In the case of the so called fumed silica, an aggregate/agglomerate of silica nanoparticles, many studies were carried out in the last years. The reason for this attention is due to the fact that the investigation of this material as archetype can help to understand how the macroscopic properties of a system are modified when it is confined into nanometric scale and, at the same time, to exploit the potentialities of these new nanometric systems. Moreover, it is worth noting that fumed silica is used in many fields as adsorbent, filler for strength reinforcement, starting material for optical fibers, etc. Notwithstanding the numerous investigations carried out on the more common bulk silica materials as well as on fumed silica, many questions still remain open or not completely understood. In particular, many unsolved questions concern the structural properties and their modifications both in bulk and fumed silica materials and, besides, how the different structural properties of silica network affect the features of the point defects.

In the present Ph.D. Thesis, experimental investigation of the structural properties and their relaxation features has been carried out in a wide set of bulk silica materials, differing in the production methods and impurities content, and in various fumed silica types, characterized by different particle mean diameters from 7 to 40 nm. Particular attention was devoted on the fumed silica and on its uncommon features, highlighting the properties that depend on its nanometric nature. Isochronal and isothermal treatments on the bulk and fumed silica materials were carried out in order to induce gradual modifications in their structural networks. Several spectroscopic techniques were employed to obtain new information, to highlight connection among optical, structural (by Raman and IR) and point defect properties, and to clarify the microscopic mechanisms that are still poorly understood. Indirect structural information were also obtained by a detailed study on different kinds of point defects, which were used as microscopic probes. In order to induce a detectable concentration of some of these point defects, the bulk and fumed silica materials were subjected to proper thermal treatments and to β- and γ-ray irradiations.

This Thesis is so organized:

- A general overview on the current knowledge about the main physical properties of bulk and nanosized silica systems is briefly reviewed in Chapter 1.
- In Chapter 2 the experimental methodologies used in this work are illustrated from a physical point of view.
- Chapter 3 is dedicated to describe the materials chosen for our analysis, the treatments carried out and the different instruments used in our investigation.
- The results obtained for the bulk and fumed silica are reported in Chapters 4 and 5, respectively.
- The final Chapter is dedicated to resume the conclusions of our study and to discuss about perspectives.

Experimental results found during this Ph.D. study and presented in this Thesis have been published (or accepted for publication) in scientific journals specialized on solid state physics. A complete list is reported at the end of the Thesis in a dedicated section.

Chapter 1

Background

In this chapter we briefly introduce the properties of amorphous silicon dioxide (silica or a-SiO_2) from a structural point of view. These topics are fundamental to understand the scientific questions that are tackled and discussed afterward. We will pay special attention to compare the known properties of the most common *bulk silica*, an a-SiO_2 system of macroscopic size (typically bigger than some μm^3), with that of *nanosized silica* characterized by size falling into nanometric scale.

1.1 Bulk silica: models and structural properties

SiO_2 exists in nine different crystalline polymorphs (eight natural and one synthetic) [1]. By X-ray and neutron diffraction studies [2, 3], it was shown that the atomic network of SiO_2 crystalline polymorphs is characterized by a regular spatial repetition of the same structural unit. This property, typical of crystalline solids, is usually indicated as *spatial periodicity.* Apart from stishovite, a natural polymorph obtained at very high pressure, all of the SiO_2 forms are constituted by a network of SiO_4 tetrahedra corners connected each others. As showed in Figure 1.1(a), each tetrahedron is characterized by a central silicon atom bonded to 4 oxygen atoms, positionated at the tetrahedron vertices, in such a manner that an oxygen atom is linked to two silicon atoms. The most known and common SiO_2 crystalline polymorph is the α-quartz. It is characterized by the $O-\widehat{Si}-O$ (φ) and $Si-\widehat{O}-Si$ (θ) bond-angles of 109.5 ° and 143.6 °, respectively [4]. The bond-lengths are 0.1608 nm (*short-bond*) and 0.1611 nm (*long-bond*); in particular, each oxygen atom is linked by a short- and long-bond to the 2 silicon atoms, so that each tetrahedron has 2 short-bonds and 2 long-bonds [4] (see the Figure 1.1(a)).

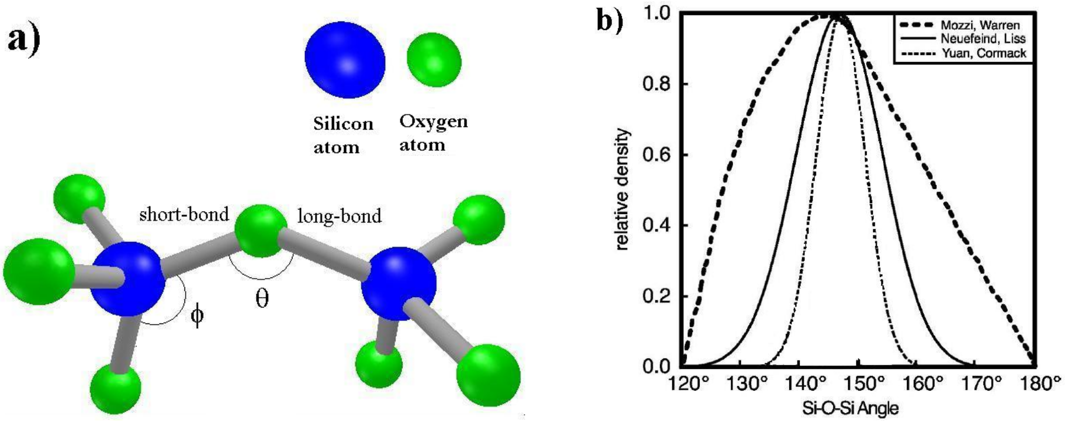

Figure 1.1: (a) Two edge sharing SiO_4 tetrahedra and (b) comparison of the $Si - \widehat{O} - Si$ bond-angle distribution in silica obtained by Mozzi and Warren (thick dashed line), Neuefeind and Liss (solid line) Yuan and Cormack (thin dashed line). Figure adapted from Clark et al. [5].

In addition to crystalline polymorphs, SiO_2 exists also in the amorphous form, commonly known as silica. The main difference between silica and SiO_2 crystalline polymorphs is that the former lacks of the spatial periodicity [6, 7]. This is well evident by X-ray spectroscopy and neutron-diffraction, in which the typical diffraction peaks of crystalline polymorphs are absent. From a thermodynamic point of view, the amorphous and crystalline forms of silicon dioxide are fundamentally different. Indeed, when SiO_2 is allowed to relax from the high temperature melt with a slow cooling rate, an almost perfect packing of tetrahedra with minimum distances and thus high density (2.65 g/cm^3 for α-quartz) is possible and a crystal is formed. On the other hand, when the melt is cooled rapidly, the system is almost frozen at the "liquid" distribution of tetrahedra, typical of the high temperature, and silica with lower density ($\sim$2.20 g/cm^3) is obtained. This is the most common way of preparing the silica materials and it is called *melt and quenching*. However, various preparation methods exist and they give different material types (see Section 3.1.1).

Despite of the intensive studies on silica, many questions related to the atomic network structure and its properties are still open and not well understood. Many models were proposed to describe the structure of silica and one of the most successful, first proposed by Zachariasen in 1932, is the *Continuous Random Network* (CRN) [7, 8]. This model assumes that the structural unit of silica is the SiO_4 tetrahedron, characterized by the same properties of that of α-quartz in terms of Si-O bond-lengths and $O-\widehat{Si}-O$ bond-angle. The amorphous nature of silica, characterized by the lack of spatial periodicity, is supposed to arise from a wide distribution of $Si-\widehat{O}-Si$ bond-angles as well as a random distribution of dihedral angles (relative rotation angle of adjoining SiO_4 tetrahedra) [7, 8]. This model was confirmed by different experimental works [6, 9, 10]. Mozzi and Warren [6], by X-ray diffraction technique and assuming an uniform distribution of the dihedral angles from 0 to 360 °[11], found a $Si-\widehat{O}-Si$ bond-angle probability distribution peaked at ~144 ° with a full width at half maximum (FWHM) of 37 ° (see the thick dashed line in Figure 1.1(b)). Afterwards, Neuefeind and Liss, combining high-energy neutron and X-ray techniques [9] and without the assumption of uniformly distributed dihedral angles, obtained a $Si-\widehat{O}-Si$ bond-angle distribution peaked at ~147 ° and with a FWHM nearly half as compared with that previously found (see the solid line in Figure 1.1(b)). These differences do not surprise, since diffraction techniques do not measure directly the $Si-\widehat{O}-Si$ bond-angle distribution but obtain it by the measure of Si-O and Si-Si bond-length distributions and under opportune assumptions. More recently, Yuan and Cormack by molecular dynamics simulations [10] confirmed that the $Si-\widehat{O}-Si$ bond-angle distribution is peaked ~147 ° (higher than the 144 ° value found by Mozzi and Warrer), but with a FWHM narrower than that reported by Neuefeind and Liss (see the thin dashed line in Figure 1.1(b)). These results are qualitatively in agreement each other and corroborate the CRN model, in which the silica $Si-\widehat{O}-Si$ bond-angle is not fixed, such as in the case of crystalline polymorphs, but it can assume different values with a bell-like probability distribution peaked at about the same value of α-quartz.

It is worth noting that the similitude between silica and α-quartz in terms of fundamental unit SiO_4 tetrahedron, covalent bonds and electron configurations gives to these two SiO_2 forms many similar macroscopic properties, as for example good mechanical resistance, low electrical conductivity and high optical transparency in a wide spectral range (visible, infrared and ultraviolet) [3, 12]. On the other hand, many other properties well evidenced by X-ray, Raman, electron paramagnetic resonance, luminescence, infrared and visible absorption techniques are strongly influenced by the intrinsic differences in the topological arrangement of the atoms in crystalline and amorphous SiO_2 forms.

On the basis of the CRN model and by X-ray and neutrons-diffraction studies, four ranges of order were defined in silica network [2, 3]:

- *range-I*; involves the fundamental units of the system: the SiO_4 tetrahedron consisting of a central silicon atom bridged to oxygen atoms with ∼1.6 $\mathring{A}$ Si-O bond lengths and $O - \widehat{Si} - O$ bond-angle distribution centered on ∼109.5 °, at its vertex. Length scale of 1÷2 $\mathring{A}$.

- *range-II*; this range involves the interconnection ($Si - \widehat{O} - Si$ bond-angles) and relative orientation (two torsion angles) of the adjacent structural units. Length scale of 2÷5 $\mathring{A}$.

- *range-III*; associated to larger features of the network topology, including n-membered rings. A ring is defined as following: start from any silicon atom and pick two of its nearest neighboring oxygen atoms (neighbors are defined by means of the minimum in the radial distribution function). Find the shortest consecutive sequence of SiO elements that connects these two oxygen atoms. In this way a closed loop of SiO segments is obtained and the length of the ring (n-membered ring) is defined as the number n of silicon or oxygen atoms in this loop. Length scale of 5÷50 $\mathring{A}$.

- *range-IV*; assigned to density fluctuations, which give rise to microheterogeneity on long length scale. Length scale >50 $\mathring{A}$.

To give a simple view of silica structure and its range of order, an example of silica atomic structure is illustrated in Figure 1.2, in which the bonds concerning range-I, -II and -III are highlighted. For this latter range of order, the 3-, 4- and 5- membered rings are highlighted. As discussed before, the properties characterizing the range-I are almost the same of that of α-quartz, hence the amorphous nature of silica is not strongly related to this range but to range-II, -III and -IV. Many experimental and theoretical studies were carried out to deepen the knowledge on the properties of these ranges and in particular on the II and the III ones, which are more sensible to the structural modifications of the network as compared with range-IV. For example, the $Si - \widehat{O} - Si$ bond-angle (the fundamental parameter of range-II) results flexible and can be modified by post-production external treatments, as for example thermal treatments, hydrostatic pressure, etc.

It was shown, by neutron-diffraction and molecular-dynamics study [14], that the $Si - \widehat{O} - Si$ bond-angle distribution for a densified (∼20 %) bulk silica material is shifted almost rigidly towards smaller angles than that of undensified silica material (see Figure 1.3(a)). The decrease of the mean $Si - \widehat{O} - Si$ angle on increasing the

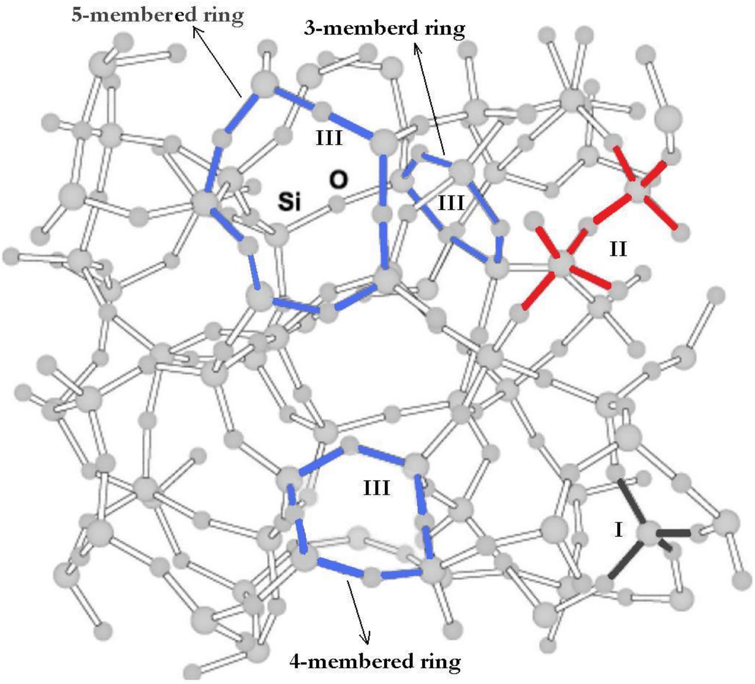

Figure 1.2: A schematic view of ranges of order of silica network. Range-I: the SiO_4 tetrahedron; range-II: the interconnections of two tetrahedra; range-III: the distribution of the n-membered rings, are highlighted. Some ring structures characterizing the range-III are indicated by arrows. Figure adapted from Uchino [13].

densification was confirmed by different experimental and simulative works [15, 16]. For example, using magic angle spinning nuclear magnetic resonance (MAS NMR), a shift of -5° of the $Si-\widehat{O}-Si$ bond-angle distribution was found in a $\sim 16\%$ pressure-densified bulk silica [16]. The comparison of the $Si-\widehat{O}-Si$ bond-angle distribution in the undensified and densified materials is reported in Figure 1.3(b).

Concerning the range-III and in particular the distribution of the n-membered rings, it is worth noting that a fundamental difference exists between amorphous and crystalline SiO_2 forms. Indeed, for various crystalline SiO_2 polymorphs, it was found that only few n-membered rings typologies can exist. For example, apart from Keatite and Coesite, the other SiO_2 polymorphs consist of only 6- and 8-membered rings [2, 3]. In contrast, silica shows a wide distribution of the n-membered rings, which was attributed to its amorphous form. In particular, it is widely accepted that the network of silica is characterized by a ring distribution centered on 6-membered

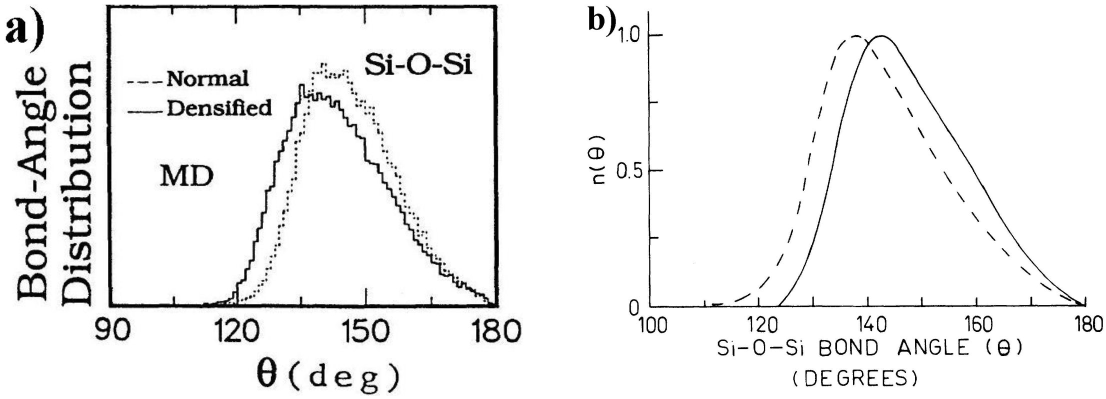

Figure 1.3: a) $Si-\widehat{O}-Si$ bond-angle distribution for undesified and densified (20 %) bulk silica materials obtained by molecular dynamics calculations (Figure taken from Clark et al. [5]). b) Experimental $Si-\widehat{O}-Si$ bond-angle distribution for undensified (solid line) and densified bulk materials (dashed line) (Figure taken from Devine et al. [16]).

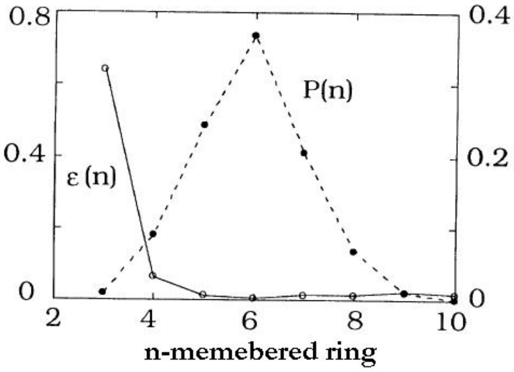

Figure 1.4: Energy (left scale) and population (right scale) as a function of the number of membered in the ring (Figure taken from Rino et al. [17]).

rings, in which 3- and 4- as well as n≥9 membered rings represent the tails [17–19].

The typical ring distribution and the energy associated to each n-membered ring, estimated by simulative analysis [17], are reported in Figure 1.4. As it is evident, 4- and in particular 3-membered rings are energetically unfavorable as compared with other rings. This finding was attributed by the authors to the very restrictive geometrical conditions associated to these small-membered rings.

Notwithstanding the low statistical population of 3- and 4-membered rings (see Figure 1.4), they play a crucial role in the study of order-III range, since a direct spectroscopic identification is possible only for these two types of rings [18]. Indeed, it is widely accepted that the two sharp Raman lines peaked at 495 and 605 cm^{-1}, well known as D$_1$ and D$_2$ lines, are assigned to the symmetric oxygen breathing vibrations of 4- and 3-membered rings respectively embedded in the silica network [15, 18, 20].

A typical Raman spectrum of a bulk silica material is reported in Figure 1.5(a) (blue curve) and the D$_1$ and D$_2$ lines are indicated. The vibration modes associated to them are reported in Figure 1.4(b). We note also the main Raman line peaked at about 440 cm^{-1}, indicated henceforth as R-line, is assigned to O-bending motion of n-membered rings with n>4 [15, 18, 20]. The area or amplitude of the D$_1$ and D$_2$ Raman lines is directly related with the population of 3- an 4-membered rings, but the same rule is not valid for the R-line. Indeed, the amplitude modification of this latter line was mainly attributed to changes of the $\frac{d\alpha}{dQ}$, where α and Q are the polarizability tensor and the vibration normal coordinate, respectively (see Section 2.1.1 for more details). However, from the shape and position changes of the R-line, qualitative information on the behavior of the n-membered rings with n>4 are usually obtained [15].

In Figure 1.5(a) the Raman spectrum acquired for a bulk silica material (blue curve) is compared with those of two materials mechanically densified at ~10% (green curve) and ~20% (red curve) [15]. The authors estimated that the area of the D$_2$ line increases by a factor of ~2.5 and ~3.5 for 10% and 20% densification, respectively [21]. A much smaller increase, by 1.1 and 1.5 for 10% and 20% densification was estimated for the 3-membered rings [21]. Besides, the evident shift towards higher energies of the R-line on increasing the densification was interpreted in terms of the shift towards smaller membered rings of the ring distribution.

As discussed before, the rings with n>4 represent over 90% of the population; so, the observed shift of the R-line position can be attributed with good approximation to the shift of the whole ring distribution. In this context, it is important to notice that the distribution of the n-membered rings, characterizing the range-III, and the $Si-\widehat{O}-Si$ bond-angle (θ), characterizing the range-II, are strongly related each others. Indeed, by geometrical considerations, the $Si-\widehat{O}-Si$ bond-angle in a planar ring was directly related with n by: θ=360°$(1-\frac{1}{n})-\varphi$, where φ is the $O-\widehat{Si}-O$ bond-angle [17]. Generally, on increasing the ring size the bond-angle θ should increase too. For example, 3- and 4-membered rings are characterized by θ angles of ~129 ° and ~136 °, respectively [18]. Obviously, it is not possible to attribute to n-membered

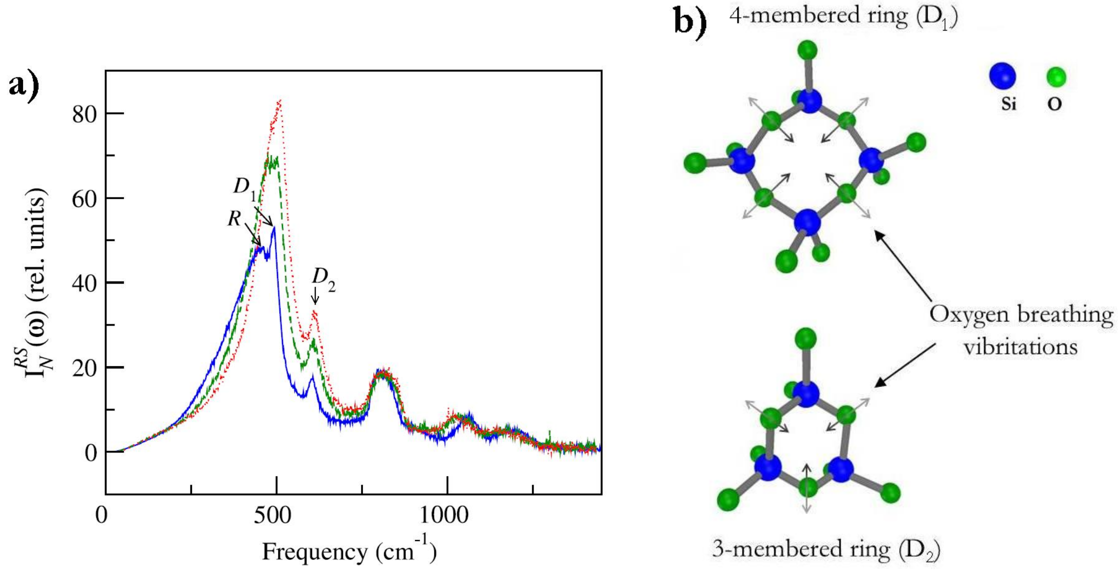

Figure 1.5: a) Raman spectra of an undensified bulk silica material (blue curve) and mechanically densified materials at ~10% (green curve) and ~20% (red curve). The D_2, D_1 and R-lines, involving 3-, 4- and n>4-membered rings respectively, are indicated (Figure taken from Hehlen et al. [15]). b) Breathing vibration modes associated to D_1 and D_2 Raman lines.

rings, with n>4, a specific bond-angle because these rings do not have in general a planar or quasi-planar geometrical shape, as for the 3- and 4-membered rings [18]. Nevertheless, as discussed above (see Figure 1.4), experimental and simulative works showed that θ mean bond-angles from 140 ° to 150 ° in bulk silica materials are mainly due to the population of 5-, 6- and 7-membered rings [18, 19]. A general rule indicates that the ring distribution shifts towards smaller-membered rings when the θ bond-angle distribution shifts toward smaller angle values [17, 21].

A more quantitative experimental relation that links the R-line position in cm^{-1} (ω_R) with the θ mean bond-angle was found by Hehlen et al. [15]:

$$cos(\theta/2) = \frac{cos(\theta_0/2)}{\omega_0}\omega_R, \tag{1.1}$$

where $\omega_0 = 437\ cm^{-1}$ and $\theta_0 = 144\ °$ are reference values.

Concerning IR spectra of silica materials, an important role is played by the band peaked at about 2260 cm^{-1}. This band, assigned to the first overtone of the SiOSi stretching vibration mode (1122 cm^{-1}), is correlated in bulk silica materials to the fictive temperature T_f (the high temperature at which silica is allowed to reach thermal equilibrium before the rapid quench to room temperature) [22]. From an operational viewpoint, when a silica sample is thermally treated at a constant temperature for an time interval long enough so that the structure reaches equilibrium, its fictive temperature approaches to the temperature of the thermal treatment. This latter is relevant because it is related to the average value of the $Si - \widehat{O} - Si$ bond-angle [23–25]. It was found that T_f increases on decreasing the $Si - \widehat{O} - Si$ bond-angle. By the analysis of IR spectra acquired for bulk silica samples, an empirical correlation between the peak position of the 2260 cm^{-1} band (ν_{2260}) and the T_f was obtained [22]:

$$\nu_{2260} = 2228.64 + \frac{43809.21}{T_f}. \tag{1.2}$$

It is important to remark that this relation was only verified in a narrow frequency range of ν_{2260}, from ~2255 to ~2263 cm^{-1}, corresponding to the temperature range 1400÷950 °C [23–25].

All of the above mentioned features have highlighted the complex nature of silica and its structural variability. In addiction, it has been shown that it is possible to obtain structural information from spectroscopic data.

1.2 Nanosized silica systems: models and structural properties

In nanotechnology, a nanosized system (or nanomaterial) can be defined as a system characterized by components with at least one dimension falling into nanometric scale. In particular, materials that have one dimension in the nanoscale are layers, such as thin films or surface coatings. Materials that have two dimensions in nanoscale include nanowires and nanotubes. Finally, materials that have all of the three dimensions in nanoscale are particles, porous system and quantum dots. Nanomaterials usually exhibit size-related properties that differ significantly from those observed in larger scale materials (bulk materials). For this reason, these materials open a wide range of potential applications in different scientific ambits as optics, mechanics, electrical devices, reactivity and biomedicine [26–34]. Indeed, nanotechnology research and its applications have been growing rapidly worldwide for the past decade, with an increasing number of nanotechnology products becoming commercially available. Besides, nanomaterials play an important role to deep the knowledge of the matter properties because they are effectively a bridge between bulk systems and atomic structures. In general, a bulk material exhibits physical properties independent of its size, whereas a strong size dependence in the nanomaterials is often observed. Thus, reducing the size down to the nanometer scale the properties of materials can drastically change [32–34].

In this context nanoparticles have attracted the attention in the last years for theirs uncommon properties (optical, electrical, magnetic, chemical and mechanical) as compared with bulk materials. Two of the major factors that gives to the nanoparticles these properties are the quantum effects, originating from the extremely reduced size, and the significantly increased of the surface area to mass ratio (*specific surface area* or S) [32–34]. For silica nanoparticles, S can assume values up to hundred of m^2/g, whereas for bulk silica materials of size $5 \times 5 \times 1$ mm^3 $S \sim 10^{-3}$ m^2/g. The number of atoms on the particle surface becomes dominant as compared with the number of atoms inside the particle when the nanometric sizes are reached. For example, a particle of 30 nm size has 5% of its atoms on the surface, whereas a particle of 3 nm size has 50% of its atoms on the surface. While, for bulk materials (larger than one micrometer), the amount of atoms at the surface is negligible if compared with the number of atoms inside the material. The predominance of surface effects can drastically change the individual properties of the particle and its interacts with the surroundings. For example, suspensions of nanoparticles in a solvent are often possible because the interaction of the particle surfaces with the solvent is strong enough to overcome the effect of different density, which otherwise should result in a system sinking or floating in a liquid. The nanoparticles are very interesting for the industry application since the large specific surface area is a critical factor for efficient catalysis as electrodes. Besides, the increase of specific surface area provides a relevant driving force for diffusion, especially at high temperatures; moreover, sintering effects can take place at lower temperatures and over shorter time scales as compared with larger particles.

Nanoparticle are currently made out of a very wide variety of materials, the most common are ceramics, which can be split into metal oxide ceramics, such as titanium, zinc, aluminium and iron oxides, and silicate nanoparticles. In this context, silica nanoparticles play an important role for their potential application in a lot of scientific fields and such as prototype system to study and deepen the uncommon properties of nanosized systems [26, 27, 30, 35, 36]. Many experimental and simulative

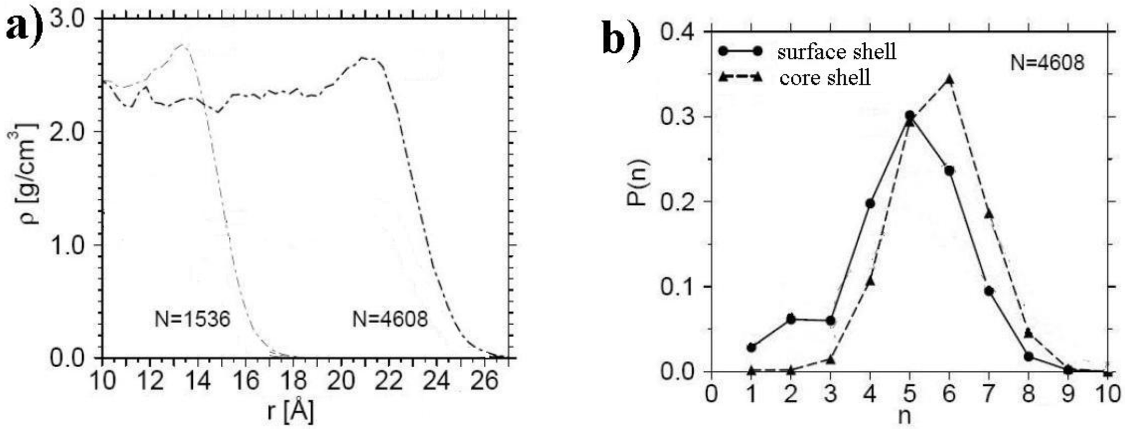

Figure 1.6: a) Radial-density profile for the cluster with ∼3 nm (thin curve) and ∼5 nm (bold curve) diameter. b) Ring distributions for the surface (circles) and interior (triangles) of the cluster. Figures adapted from Roder et al. [39]).

investigations were performed in order to understand how the atomic network of silica changes when the nanometric scale is reached [37–41].

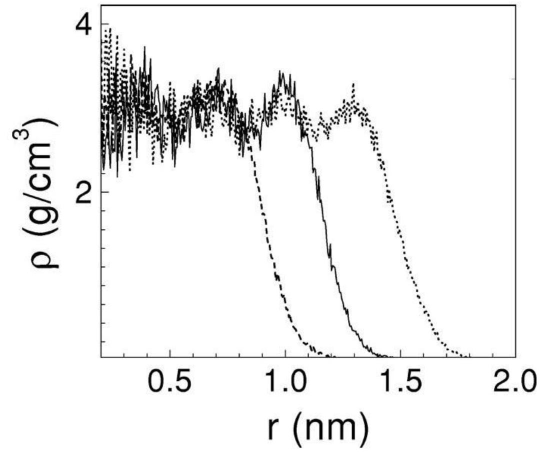

Figure 1.7: Radial-density profile for the cluster with diameter of 1.8 nm (dashed line), 2.3 nm (solid line) and 3 nm (dotted line). Figure adapted from Schweigert et al. [40]).

By molecular dynamics computer simulations, Roder et al. [39] evidenced that silica clusters show a characteristic radial-density profile attributed to the small size of the system. In details, two clusters consisting of 1536 and 4608 atoms in thermal equilibrium at different temperatures were considered. The shape of the clusters is independent of the temperature and becomes more spherical with increasing the size of clusters. As reported in Figure 1.6(a), the radial-density profile for both clusters, characterized by ∼3 and ∼5 nm diameter, shows a small peak just below the clusters surfaces. Besides, the ring distribution estimated for the interior and the surface region of a cluster is different. These distributions, reported for the largest system in Figure 1.6(b), show that the whole ring distribution for the near-surface of cluster is shifted a bit to smaller-membered rings as compared with that of the inner part of cluster. It is worth noting that, this latter region has a distribution similar to that reported for bulk silica, in which 6-membered rings are the most probable (Figure 1.4). A different atomic configuration between these parts of the cluster were corroborated by investigation of the bond-angle ϑ. Indeed, the mean value of this angle in the inner part of cluster is comparable with that of bulk silica, whereas it is smaller for the atoms near the surface region [39]. These findings were interpreted by the authors as the consequence of a different energy associated to the inner and surface parts of the cluster. In particular, the surface of the cluster is the region where the atomic-bonds are more affected by the strains resulting from the presence of the interface. For this reason, the surface part is characterized by a higher energy as compared with that of the inner one.

The evidence of a *shell-like structure* of silica clusters, characterized by an inner (hereafter indicated as *core-shell*) and a surface region (*surface-shell*), was confirmed by the simulations of clusters of different sizes (1.8, 2.3 and 3 nm diameter) [40]. Indeed, as shown in Figure 1.7, a density-profile characterized by a peak density near the surface and a constant value for the core part, was found for different clusters. Besides, the authors showed that smaller clusters had a larger mean density. In particular, mean densities of 3.2 and 2.8 g/cm^3 were found for clusters of 1.8 and 3 nm diameter, respectively. In agreement with Roder et al. [39], these findings were interpreted in terms of bond-strains, which are stronger near the surface of the clusters as compared with the core-shell.

In agreement with the investigations by computer simulations discussed above, many experimental works performed by different techniques showed the unique structural properties of silica nanoparticles [37–41]. Many of these works were done on the so called *fumed silica*, a powder of aggregate/agglomerate[a] of silica particles with sizes falling into nanometric scale. Since the mean diameter of nanoparticles can be

---

[a] An aggregate is defined as an assembly of particles loosely attached to each other. An agglomerate is an assemblage of particles rigidly joined together, as by partial fusion (sintering) or by growing together.

modified during the manufactory process (typically from few up to tens nanometers) and thanks to its potential application in widespread ambits, this material has attracted considerable interest in the last decade. A detailed description of the production method, common properties and fields of commercial use of the fumed silica materials will be presented in Section 3.1.2.

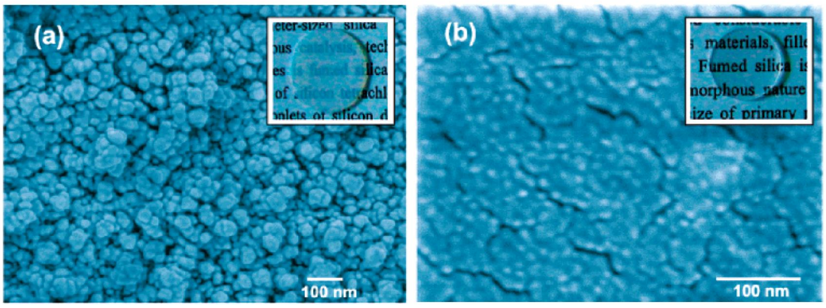

Figure 1.8: a) FESEM images of untreated and b) thermally treated (at 980 °C for 168 h in air) fumed silica in form of tablet. The photograph of each sample is reported in the inset. Figure taken from Yamada et al. [42].

Yamada et al. showed that, pressing in a uniaxial hydraulic press at 530 MPa the powder of fumed silica with 7 nm diameter particles, a translucent self-supporting tablet is formed (see the inset in Figure 1.8(a)) [42]. By thermal treatment at 980 °C in air, the tablet gradually increases its transparency to the naked eye and shrinks on increasing the treatment time. After 168 h of treatment, it becomes completely transparent such as a traditional bulk silica material (see the inset in Figure 1.8(b)). The authors investigated the morphology evolution of the tablet by acquiring the field emission scanning electron microscopy (FESEM) images before and after thermal treatments [42]. As evident in Figure 1.8, the FESEM image of untreated tablet shows particles of fumed silica packed closely together, while after the thermal treatment at 980 °C for 168 h, it is not possible to recognize the particles since they are fused together. However, boundaries on the microscopic length scale are still visible, suggesting that the system has not fully lost its original nanometric nature.

In the same work, Raman spectra were acquired in order to study in more details the structural modifications induced by thermal treatments on fumed silica [42]. In Figure 1.9, the Raman spectra of fumed silica before and after thermal treatment at 980 °C for different times (24, 96, 168 h) are shown. In the same figure, a typical Raman spectrum of bulk silica is reported for comparison. As it is well evident, untreated fumed silica exhibits a very different Raman spectrum as compared with

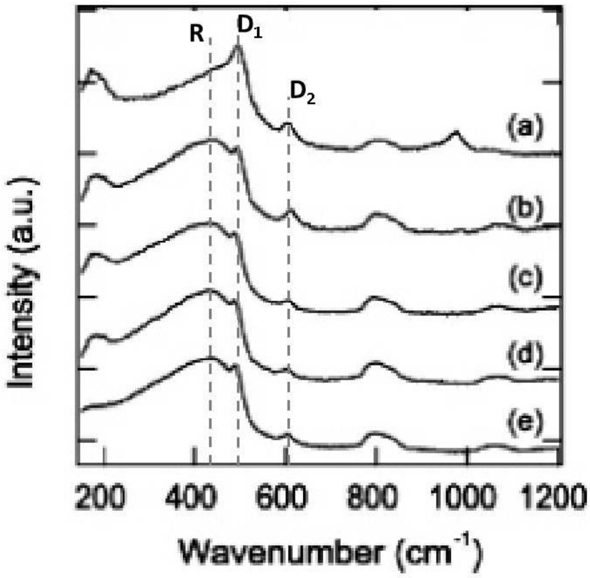

Figure 1.9: Raman spectra of fumed silica a) before and after thermal treatment at 980 °C for b) 24 h, c) 96 h and d) 168 h. For comparison, the Raman spectrum of normal bulk silica material is also shown in e). Figure adapted from Yamada et al. [42].

that of bulk silica (compare a) with e) spectra): the R-line is so shifted towards higher frequencies to overlap partially to D_1 line, the D_1 and D_2 lines are more intense and a peak at about 950 cm^{-1} is present. These findings suggested that 3- and 4-membered rings, assigned to D_2 and D_1 lines respectively, are more frequent in fumed silica than in the bulk silica, corroborating the idea that the structural network of fumed silica is different from that of the bulk one. The presence of the peak at about 950 cm^{-1}, associated with the Si-(OH) stretching, evidences a high concentration of silanol groups in fumed silica, which will be discussed in more details in the following section. The thermal treatments drastically modify the Raman spectrum of fumed silica so that the sample treated for 168 h becomes almost undistinguishable from that of bulk silica (compare d) with e) spectra in Figure 1.9).

By Raman and infrared spectroscopy, the authors proposed an arrangement of the fumed silica particles in which the untreated sample consists of numerous open pores, originated from the regions between the particles, as schematically shown in Figure 1.10(a). The thermal treatment enables the closure of the pores by the dehydroxylation reaction of silanol groups (Si-OH) on particle surfaces, formimg 2-membered rings (edge-sharing tetrahedral units): $2\equiv\text{Si-OH} \rightarrow \equiv\text{Si-O-Si}\equiv + H_2$

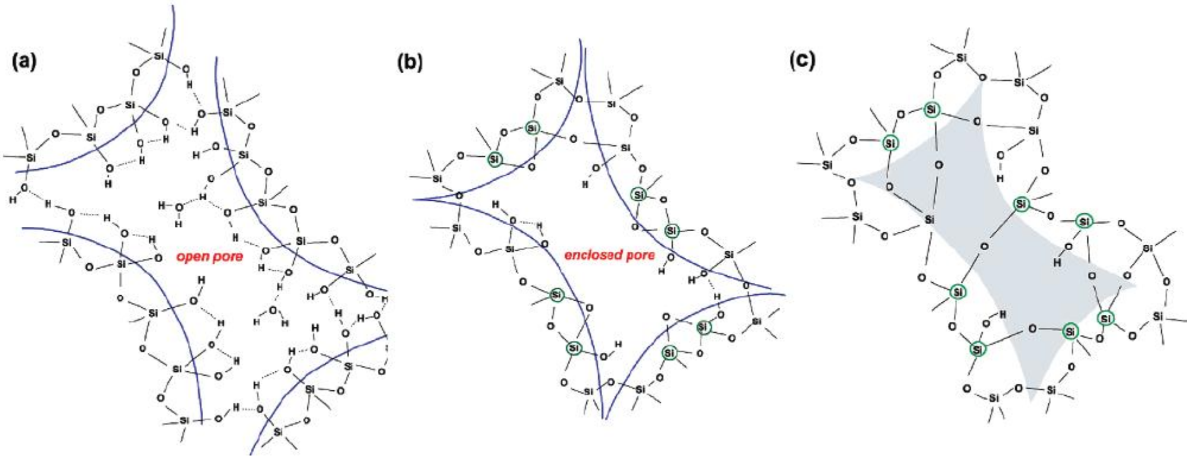

Figure 1.10: Schematic atomic arrangements of a) non-treated fumed silica sample with open pores, b) thermally treated sample with enclosed pores and c) thermally treated sample with no enclosed pores. The Si atoms involved in and derived from the edge-sharing tetrahedral units are circled in b) and c), respectively. The shaded part in c) indicates the region in which the interfacial atomic arrangements are not fully relaxed and are hence highly deformed. Figures taken from Yamada et al. [42].

(Figure 1.10(b)). Since these very small-membered rings are characterized by a large strain energy [43], they are instantaneously destroyed and form interparticle siloxane bonds, removing the enclosed pores (Figure 1.10(c)). The final structure obtained by this process is very similar to that of bulk silica, as suggested by the Raman spectra of thermally treated fumed silica. It is important to note that the thermal treatments considered in the Yamada work drastically modify the fumed silica Raman features (D_1, D_2 and R-line), so that already after the first step of thermal treatment (T=980 °C for 24 h, Figure 1.9(b)), the Raman spectrum is comparable with that of bulk silica.

A more gradual change of the Raman features were investigated by Uchino et al. [44]. In this work the same fumed silica typology considered in the work discussed above [42] was thermally treated in air between 900 and 1200 °C for 2 h. The FESEM images and Raman spectra of fumed silica for these treatments are displayed in Figure 1.11(a) and (b). The FESEM images reveal that a gradual sintering process takes place in this temperature range, consisting in the coalescence of the particles that generate grains of larger size. As anticipated, the Raman spectra show a gradual decrease of the intensity of D_1 and D_2 lines when T varies from 900 to 1200 °C (Figure

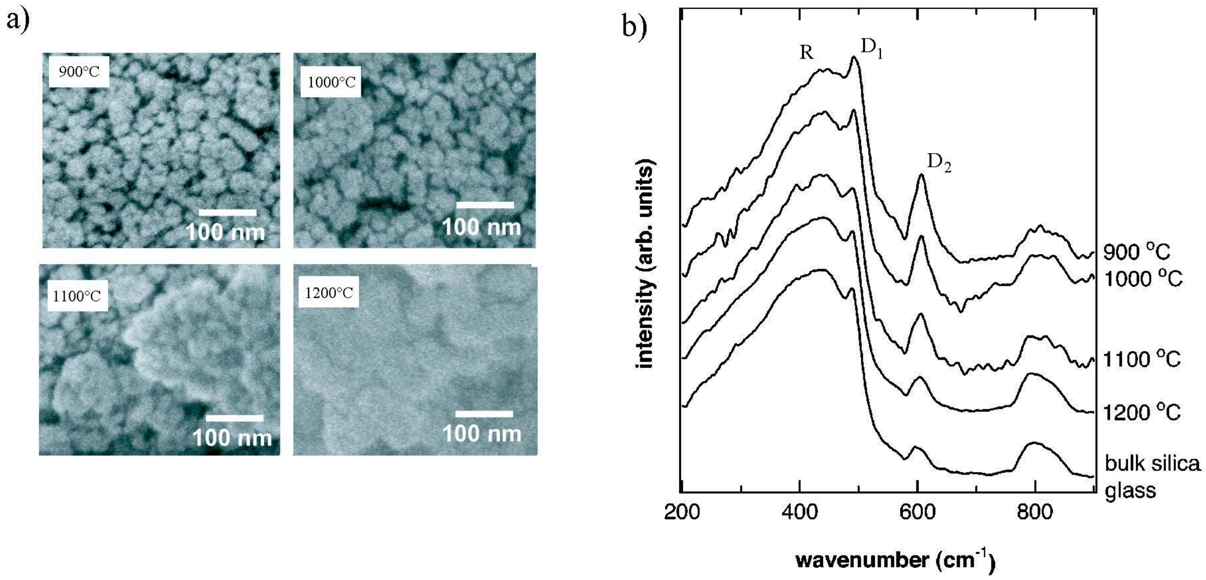

Figure 1.11: a) FESEM images and b) Raman spectra of fumed silica after heat treatment 900 and 1200 °C for 2 h. b) The correspondent Raman spectra of fumed silica after thermal treatments between 900 and 1200 C. The Raman spectrum of normal bulk silica glass is also shown for comparison. Figures adapted from Yamada et al. [44].

1.11(b)). In particular, at T=1200 °C the whole Raman spectrum is very similar to that of bulk silica. These findings corroborated also the idea that the network of as prepared fumed silica particles is characterized by a high population of 3- and 4-membered rings, which evidences structural strains on the atomic configurations. The authors suggested that these uncommon structural properties of the particles arise from the production method, in which during the early stages small SiO_2 clusters, consisting mainly of small membered rings and with a very stressed network, form. Subsequently, these clusters are fused together to build up the fumed silica particles and the original stress or strains are partially removed. In this scheme, the fumed silica particles have "memory" of the small isolated clusters formed originally at very high temperatures [44]. In this work the authors also observed by IR absorption measurements that the peak position of the 2260 cm^{-1} band for silica particles with 7 nm diameter falls below 2255 cm^{-1} [44]. They tried to estimate the corresponding fictive temperature by the Equation 1.2, obtaining values higher than 4000 °C. These findings were interpreted as a consequence that the above mentioned equation can not be simply extended for $\nu_{2260} < 2255$ cm^{-1}. However, the evident shift of the considered band toward lower energies suggested that the silica nanoparticles are characterized by higher T_f and hence smaller $Si - \widehat{O} - Si$ bond-angle, as compared with those of bulk materials.

Another difference between fumed and bulk silica from the structural point of view concerns its response to high pressure. Indeed, it is well known that the response of bulk silica pressed up to ∼10 GPa at room temperature falls into the *elastic regime*, characterized by the fact that the compression induced by hydrostatic pressure on the sample is elastic and reversible [3, 45, 46]. For higher pressures, an *anelastic regime* is observed and an irreversible densification is induced [3, 45, 46]. By X-ray diffraction investigation, Uchino et al. [47] found that fumed silica with 7 nm particles shows an anelastic response for pressure in the range from 4 to 8 GPa, which is well below the corresponding counterpart anelastic regime of bulk silica ($\gtrsim$10 GPa). This anomalous property of fumed silica indicates a different compressibility of nanoparticles network as compared with that of bulk silica.

1.3 Point defects in bulk and nanosized silica systems

A point defect can be defined as a local distortion of the atomic network structure due to the presence of one or more broken atomic bonds, of an over or undercoordinated atom, of an impurity atom, etc. [2, 48]. Points defects are classified as *intrinsics* if they are due to network distortions involving the same atoms that constitute the material (O and/or Si atoms in the case of silica) and *extrinsics* if they involve impurities. Besides, on the basis of their electronic configurations, points defects are indicated as *paramagnetic* when they have a non-zero electronic magnetic moment (unpaired electrons), otherwise they are indicated as *diamagnetic*. The presence of point defects in bulk and nanosized silica materials is mainly due to the manufacturing process or to the exposure to particle or ionizing radiation. Generally, the point defects found in the *as-grown* material (before any post manufacturing treatments) are prevalently diamagnetic, whereas paramagnetic centers are under the concentration detectable by typical experimental techniques. By an opportune *dose*[b] of irradiation (for example laser, X-ray, γ-ray, β-ray, etc), a measurable concentration

---

[b] Dose (D) is the deposited energy (E) in a target of thickness x: $D = \frac{\phi \Delta t}{x} \int_0^x |\frac{dE}{dx}| dx$, where $\phi \Delta t$ is the fluence of projectile particles (particles per unit area) [3, 49].

of paramagnetic centers can be induced in bulk and nanosized silica materials.

1.3.1 Silanol groups

Silanol groups are among the most common diamagnetic centers of silica. They affect many macroscopic properties of the bulk and nanosized silica materials. In the former case, many studies were performed and evidenced that the presence of silanol groups modifies the viscosity, the refraction index, the density, the thermal expansion coefficient, the radiation-sensitivity etc. [50–53]. In particular, silanol groups play a fundamental role in telecommunications by optic fibers because they limit the spectral windows for the signal transmission. On the other hand, the large specific surface area of nanosized silica materials makes the silanol group mainly surface reactive sites, which determine the chemical activity of these materials [54]. The types of silanol groups, the concentration, the accessibility, etc. are parameters which can strongly modify many properties of nanomaterials, as for example the desiccant and sintering features [35, 36].

Raman and infrared (IR) absorption spectroscopies are the techniques most used to study the properties of silanol groups in bulk as well as in nanosized silica materials. In particular, since the vibration mode of silanol groups (stretching vibrations) involves mainly the change of dipole moment, the IR spectroscopy results more sensitive than Raman spectroscopy [c]. For this reason, numerous works on silanol groups were mainly carried out by IR spectroscopy.

The IR spectrum of silica bulk materials is characterized by an asymmetric band peaked at ~ 3670 cm^{-1}, which is believed to arise from the superposition of several sub-bands involving the OH bond stretching vibration of different types of silanol groups [55–60]. The number of sub-bands and their attributions were debated for a long time. Here we report the results of one of the latest works, which was done by Plotnichenko et al. [56]. By IR spectroscopy and computational analysis, Plotnichenko et al. showed that the shape and the position of the IR band is the same for all of the investigated silica materials and proposed that this band can be decomposed into 4 sub-bands [56]. The IR band and its decomposition are shown in Figure 1.12. The vibrational frequencies and the different types of silanol groups (see Figure 1.13) were assigned in the following way [56]:

- 3630 ± 6 cm^{-1}: single Si-OH groups H-bonded with Si-O-Si linkages and pairs

---

[c] For a more detailed discussion see Sections 2.1.1 and 2.1.2

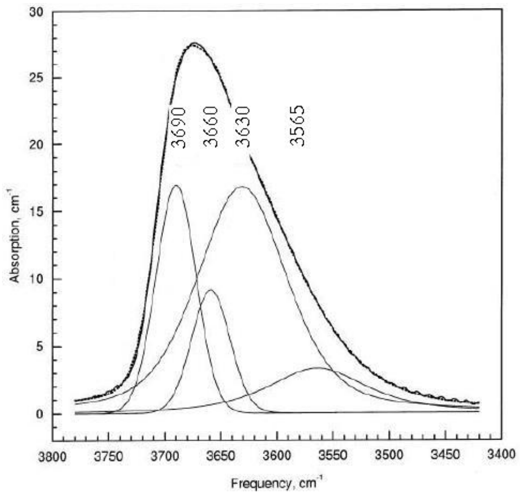

Figure 1.12: a) Experimental IR absorption band of silanol groups in bulk silica and its decomposition into four components. Figure taken from Plotnichenko et al. [56].

of Si-OH groups H-bonded with each other in linear configuration through one H bond (vibration of only one of the OH groups of the pair, namely the one involved in the hydrogen bond);

- 3660 ± 4 cm^{-1}: single Si-OH groups slightly bound with bridging oxygen atoms and pairs of Si-OH groups H-bonded with each other in linear configuration (vibration of only one of the OH groups of the pair, namely the one not taking part in the hydrogen bond);
- 3565 ± 14 cm^{-1}: pairs of Si-OH groups H-bonded with each other in cyclic configuration and pairs of Si-OH groups H-bonded with each other in linear configuration (vibration of only one of the OH groups of the pair, namely the one involved in the hydrogen bond);
- 3690 ± 2 cm^{-1} free single Si-OH groups interacting neither with each other nor with Si-O-Si linkages;

Many experimental works unambiguously confirmed the presence of silanol groups on the surface of both bulk and nanosized silica materials . From this point of view, it is worth noting that the broad IR band peaked at ~ 3670 cm^{-1} in bulk silica materials (shown in Figure 1.12) is mainly due to silanol groups localized in the inner part of system (bulk silanol groups). These latter kinds of point defects are indeed much

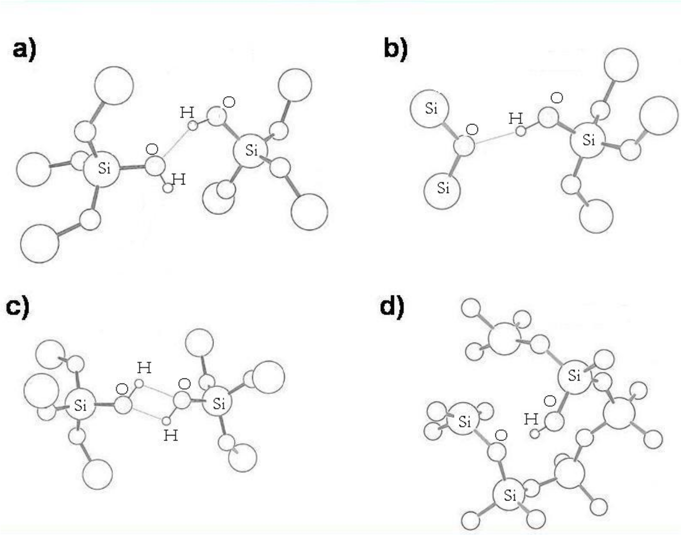

Figure 1.13: Possible bond configurations of bulk silanol groups: a) nearly linear structure, b) symmetric cyclic structure, c) asymmetric cyclic structure and d) free single Si-OH groups. Figure adapted from Plotnichenko et al. [56].

more numerous than those localized on the surface (surface silanol groups) in bulk silica. On the other hand, the large specific surface area characterizing the porous and nanosized systems makes the contribution of surface point defects predominant. In particular, it is well known that the surface properties of nanosized systems strongly depend on the presence of surface silanol groups. Indeed, if the concentration of these groups is sufficient, the material is characterized by a hydrophilic nature. That is, surface silanol groups act as the centers of molecular adsorption with the capability to form hydrogen bonds with other silanol groups, water molecules, CH_n groups, etc. As a consequence of the presence of surface silanol groups and of the species linked to them, the IR spectrum of a nanosized silica material can be very different as compared with its bulk counterpart. Typical IR spectra acquired for porous silica materials, characterized by S=270 m^2/g and 14 nm mean pore sizes, under room atmosphere (dotted line) and under vacuum (solid line) are reported in Figure 1.14 [59]. Both IR spectra show a main composite broad band, extending from 2500 to 4000 cm^{-1}, and two smaller bands peaked at 4600 and 5200 cm^{-1}. The authors, in agreement with many other works, interpreted the main IR band as the sum of different contributions [55, 57–60]:

- **bulk silanol groups**, 3670 cm^{-1} (the same band reported in Figure 1.12);

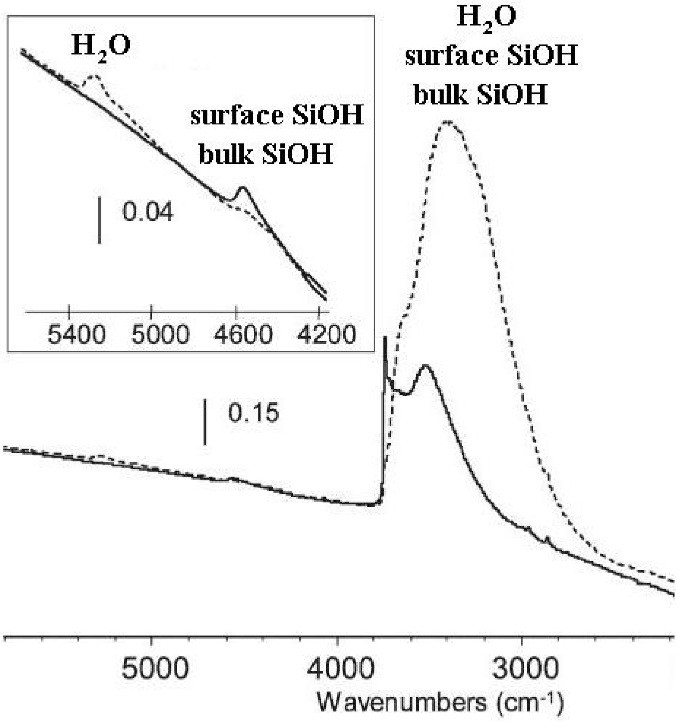

Figure 1.14: IR spectra of a porous silica material in the 2200-5800 cm^{-1} range. Dotted line: spectrum recorded under room atmosphere. Solid line: spectrum recorded after outgassing the sample under vacuum 10^{-5} hPa during 1 h. In the inset contributions of H_2O, surface and bulk SiOH groups to different bands are indicated. Figure adapted from Gallas et al. [59].

- **surface silanol groups**;
  - surface free single Si-OH groups not-perturbed and/or weakly perturbed by neighboring OH groups, 3730÷3750 cm^{-1};
  - surface SiOH groups engaged in H-bonding with each other and/or with water molecules, 3520 and 3680 cm^{-1};
- **water molecules physisorbed with surface silanol groups**;
  - first overtone of the H_2O bending (ν_2), 3250 cm^{-1};
  - H_2O symmetric stretching (ν_1), 3450 cm^{-1};
  - H_2O antisymmetric stretching (ν_3), 3610 cm^{-1};

The band in the range 4200÷4800 cm^{-1} is attributed to the combination of the stretching and bending modes of silanol groups (both bulk and surface), while the band in the range 5000÷5400 cm^{-1} is associated to nearly degenerate combination of water modes[d]. As shown in Figure 1.14 (solid line), water is removed from the silica surface after outgassing under 10^{-5} hPa for 1 h at room temperature because the 5250 cm^{-1} had completely vanished, while the narrow band at 3740 cm^{-1} appears. Before outgassing, this latter band is absent in the sample under room atmosphere because almost all of the “potential” surface free single Si-OH groups are bonded to some water molecule. Besides, by the comparison of the main IR band before and after outgassing, one can say that the main contribution to this band arises from water. This observation is in agreement with many experimental works on other nanosized silica materials [55, 57–59]. For example, it was reported for silica nanoparticles that water is multi-layer distributed with the first hydration layer hydrogen-bonded to surface silanol groups and the second layer constituted by water molecules linked together on the same particle and/or linked to water molecules of nearby particles [58]. A scheme of this multi-layer structure is reported in Figure 1.15(a).

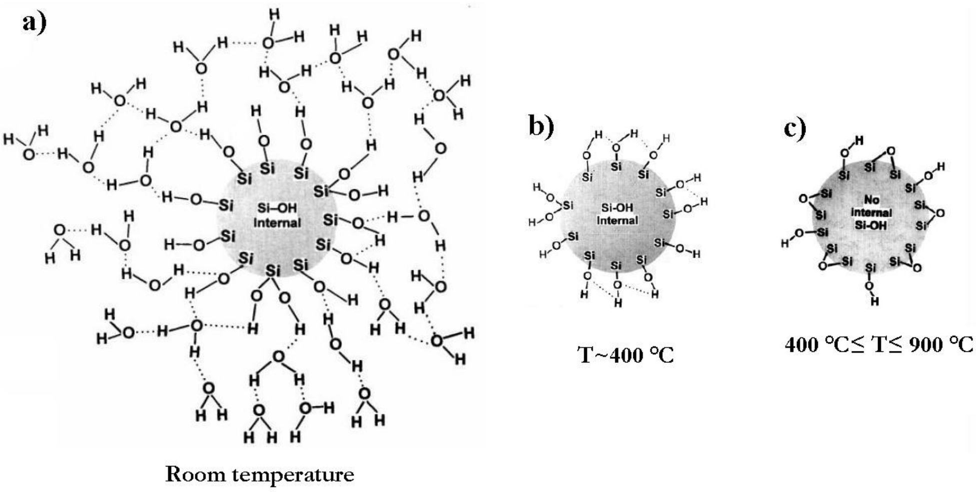

Figure 1.15: Schematic representation of water hydrogen-bonded to surface silanol groups of a silica nanoparticle under room atmosphere at different temperatures. Figure adapted from Zhuravlev et al. [58].

---

[d] In particular, this band is attributed to nearly degenerate $\nu_1 + \nu_2$ and $\nu_2 + \nu_3$ combination modes of bending (ν_2 ~1630 cm^{-1}), symmetrical stretching (ν_1 ~3560 cm^{-1}) and antisymmetrical stretching (ν_3 ~3650 cm^{-1}) modes of water[55, 61].

Many works on silica nanoparticles showed that the removal of water physisorbed on surface (dehydration) can be induced by thermal treatments under room atmosphere. In particular, water is completely removed at T∼400 °C and the only remaining surface point defects are Si-OH groups engaged in H-bonding with each other (bands at 3520 and 3680 cm^{-1}) and free single Si-OH groups (band at 3740 cm^{-1}) (see Figure 1.15(b)). However, the dehydration process is readily reversible at this temperature and the complete rehydroxylation takes place. For 400 °C $\leq$T$\leq$ 900 °C, surface Si-OH groups H-bonded decrease and form siloxane groups by the process: $\equiv$Si-OH HO-Si$\equiv$ $\rightarrow$ SiOSi + H_2O. At T∼900 °C, the particle surfaces are mainly constituted by siloxane and surface free single Si-OH groups (see Figure 1.15(c)).

1.3.2 Optical active point defects

As discussed above, the concomitance of large specific surface area and the presence of surface silanol groups strongly influences the absorption properties of nanosized materials in the IR range. The effects of the nanometric confinement are also evident in visible (Vis) and ultraviolet (UV) ranges. It was reported that silica nanoparticles are characterized by optical and photoluminescence (PL) activities which are absent in the corresponding bulk materials [13, 42, 62–68]. In particular, two different types of PL activities can be induced by thermally treating the fumed silica with particles of 7 nm diameter for few hours (<5h) at low temperature (T<500°C) [62–64] and for long time (>50h) at high temperature (T=900÷1000°C) [13, 42, 65, 66]. In the former case, a PL band peaked at about 460 nm (∼2.7 eV) (indicated hereafter as blue-band) with FWHM∼0.8 eV and life time of few nanoseconds is induced. The steady state PL spectra for fumed silica before and after thermal treatment at 300 °C for 2 hours are shown in Figure 1.16(a). The untreated spectrum is characterized by a complex PL band composed by a band peaked at ∼400 nm (∼3.1 eV), attributed to organic groups physisorbed on the particle surface, and by the blue-band. After the thermal treatment this latter contribution increases. In details, by isochronal thermal treatments of 2 h, it was shown that blue-band increases up to T=300÷400 °C, whereas it rapidly decreases for higher temperatures [63, 64]. The photoluminescence excitation spectrum (PLE) of the sample thermally treated at 300 °C for 2 h, monitored at 440 nm is shown in Figure 1.16(b). The authors attributed the blue-band to a defect pair formed by a dioxasilirane =Si=O_2 and a sililene center =$\mathrm{Si}^{\bullet\bullet}$, originated from the interaction of silanol groups (see the scheme in Figure 1.16(c))[62, 63].

On the other hand, a different PL activity can be induced in the same fumed si-

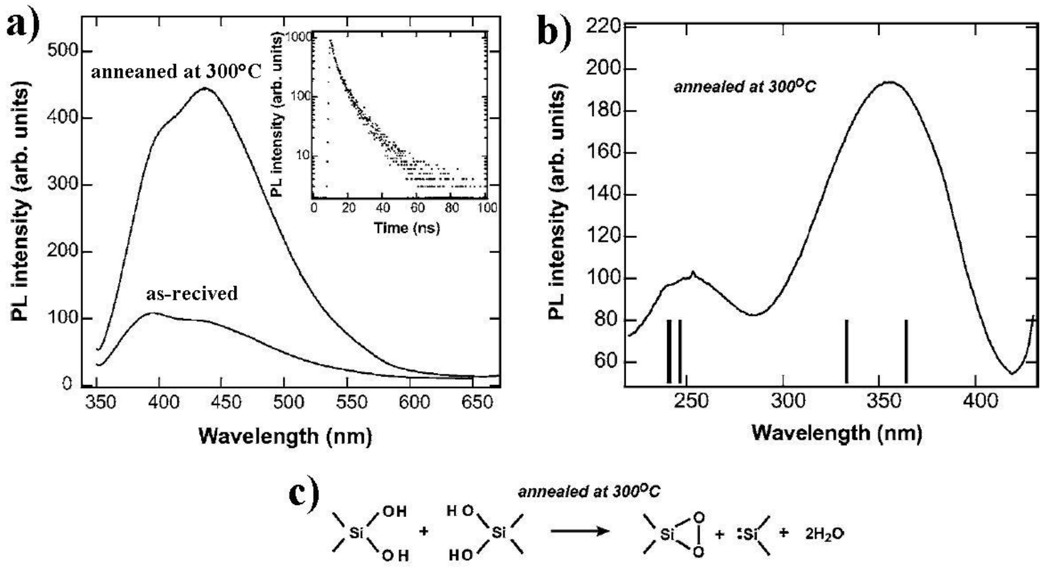

Figure 1.16: a) Steady state PL spectra of fumed silica with particles of 7 nm diameter before and after thermal treatment at 300 °C for 2 h. The PL spectra were measured under an excitation of 3.54 eV (350 nm). The inset shows a PL decay of the treated sample, for the same excitation of 3.54 eV (350 nm) and detected at 2.76 eV (450 nm). b) Photoluminescence excitation spectrum of treated sample monitored at 2.82 eV (440 nm). c) Reaction model leading to the formation of the point defects associated to the blue-band. Figures taken from Uchino et al. [62]

lica typology after thermal treatments at 980 °C. Indeed, as shown in Figure 1.17(a), a broad PL band peaked at about 510 nm (indicated by the authors as white-band since it exhibits a white light emission quite visible to the naked eye) under UV excitation gradually grows on increasing the thermal treatment time. The time-resolved PL signal, detected at 510 nm (∼2.43 eV) using a pulsed Nd:YAG laser at 266 nm (∼4.66 eV), is reported in Figure 1.17(b) for the sample thermally treated for 192 h. As evident, this band is characterized by a longer life time (∼200 ns) as compared with that of the blue-band (Figure 1.16). The authors highlighted a strong correlation between this band and the sintering process. Indeed, the growth of the PL emission on increasing the thermal treatment time is accompanied by a reaction transforming the sample from opaque to transparent (see the sequence of sample imagines taken at different treatment times in Figure 1.17(c)). It is important remembering that these PL activities (blue- and white-bands) have never been found in bulk silica and consequently they are assumed to be typical of the silica nanoparticles. Notwithstanding

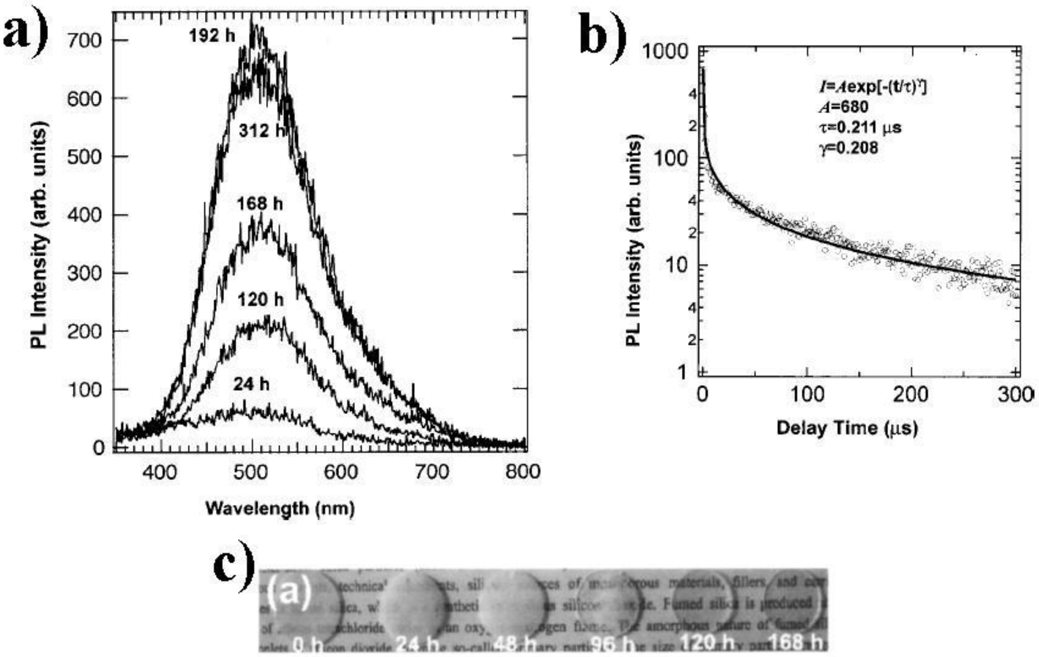

Figure 1.17: Steady state PL spectra of a fumed silica sample thermally treated at 980 °C for different hours from 24 to 192 h. The PL spectra were measured under an excitation of 5.44 eV (228 nm). b) A semilog plot of the PL decay signal for the sample thermally treated for 192 h. The time-resolved PL signal has been detected at 2.43 eV (510 nm) and excited at 4.66 eV (266 nm). The solid line is the best-fit curve using a stretched exponential function. c) Pictures acquired for the disk shaped samples after thermal treatments for different times at 980 °C. Figures adapted from Uchino et al. [66].

the studies carried out, the properties of these photoluminescence bands have not been fully clarified. In particular, the relation between the nanometric nature of silica and the exact physical origin of these emission band activities are lacking.

1.3.3 Paramagnetic point defects

The reduced size of a system can strongly affect many other properties of the matter as for example paramagnetic ones. Before to discuss these features in nanosized silica materials, it is useful introducing briefly some questions on more common bulk silica materials. The paramagnetic properties of these latter are mainly due to the point defects induced during the manufacturing process or after the exposure to particle or ionizing radiation. Among the point defects in silica, the so called E'_γ

center is one of the most known and investigated [3, 69]. This point defect can be detectable by EPR spectroscopy after an opportune irradiation dose by X-ray, γ-ray, laser, etc. The most accepted microscopic model for the E'$_\gamma$ center assumes that this defect is a positively charged oxygen vacancy; it has an atomic structure characterized by an unpaired electron highly localized in a sp^3 hybrid orbital of one of the silicon atoms constituting the vacancy: $O{\equiv}Si^\bullet\ {}^+Si{\equiv}O$ (where $\equiv$ represents the bonds with the three distinct oxygen atoms and $^\bullet$ is the unpaired electron) [2, 3, 70–72] (see Figure 1.18(a)).

It was shown that E'$_\gamma$ center line shape in the EPR spectrum depends on the radiation dose [73]. In Figure 1.18(b), the EPR spectra acquired with a frequency $\nu \sim$9.8 GHz (see Section 3.3.2 for more details) for a bulk silica material irradiated at doses of 0.5, 50, and 5000 kGy are reported. This figure shows a gradual line-shape variations: the zero-crossing point shifts towards smaller resonance fields on increasing of the irradiation dose. In particular, the line shape for low doses ($\sim$0.5 kGy) is characteristic of an almost axial symmetry (indicated by the authors by the symbol *L1*), which tends towards a more orthorhombic one at higher doses (*L2*). A more quantitative investigation was performed by the authors in terms of principal g values, g_1 , g_2 , and g_3, approximately determined from the field values at which the first maximum (g_1), the zero-crossing point (g_2), and the minimum of the EPR spectra (g_3) occur [74]. By this analysis it was found that the difference $\Delta g_{1,2}=g_1-g_2$ varies from 0.00124, at the dose=0.5 kGy (low-dose), up to 0.00115, at the dose=5000 kGy (high-dose). Whereas the variation of $\Delta g_{1,3}=g_1-g_3$ is less pronounced. The concentration of E'$_\gamma$ centers as a function of irradiation dose (*growth curve*) is shown in the inset of Figure 1.18(b). The initial growth and then the tendency to a constant value of concentration on increasing of irradiation dose is typical for bulk silica materials; it has been attributed to a generation process of E'$_\gamma$ centers from other point defects (*precursors*) [75]. However, a direct generation of E'$_\gamma$ centers from the matrix can also be possible for higher radiation doses. It is important saying that the many silica typologies (see Section 3.1.1) have a different radiation sensitivity therefore the growth curve strongly depends on the considered material. The L2 line shape, obtained after high irradiation doses, can be converted into the L1 one by thermal treatments. In particular, the authors observed that the EPR line shape of a sample irradiated at 4000 kGy gradually changes from L2 toward L1 after isochronal thermal treatments, at room atmosphere and with time fixed to 25 min, in the temperature range of 370÷460 K. These findings were interpreted

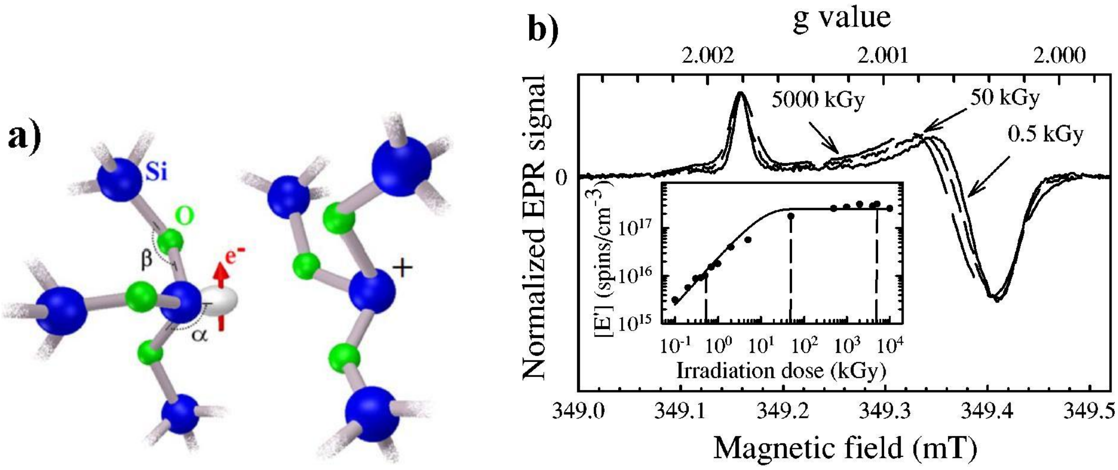

Figure 1.18: Microscopic structure of the E'$_\gamma$ center in a-SiO$_2$. The arrow represents an unpaired electron (e$^-$) in a Si sp^3 orbital and the symbol + indicates a trapped hole. b) EPR spectra of the E'$_\gamma$ centers normalized to the peak to peak amplitude and horizontally shifted to overlap at the first maximum. The samples were irradiated at doses 0.5 kGy (solid line), 50 kGy (short-dashed line) and 5000 kGy (long-dashed line); in the inset the E'$_\gamma$ center concentration as a function of the dose is reported (the solid line is a guide to the eye). Figure adapted from [73].

in terms of two different energetic configurations of the E'$_\gamma$ center: a stable state, associated to centers with almost uniaxial EPR line shape (L1) and a metastable state, attributed to an orthorhombic line shape (L2). From a more structural point of view, the former state corresponds to backward puckered configuration of Si$^+$ (see Figure 1.18(a)), while the metastable state is attributed with a migration of Si$^+$ through the plane of the bonding O atoms (unpuckered configuration).

Different EPR line shapes of the E'$_\gamma$ center were observed at low doses in pressure-densified bulk silica materials [76]. In Figure 1.19(a), the EPR spectra of the E'$_\gamma$ center acquired for an undesified and two densified bulk silica samples at 15 and 24%, after a γ irradiation dose of 760 kGy, are shown. The samples were permanently densified by hydrostatic press. The gradual change of the EPR line shape on increasing of the densification is also accompanied by an enhancement of the signal intensity improving the radiation sensitivity. Indeed, as reported in Figure 1.19(b) for two different silica material types, the creation efficiency of point defects in densified materials is 60 times that found in the undensified silica of the same type. These findings were interpreted by the authors in terms of a more strained network for the

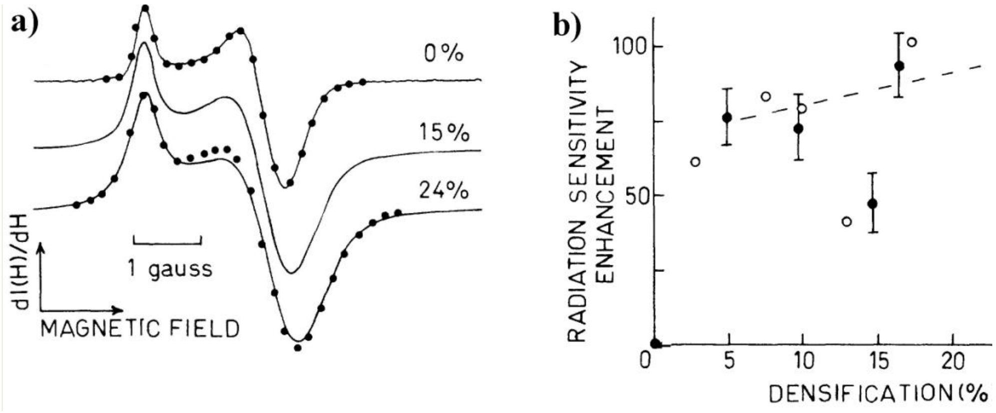

Figure 1.19: a) EPR spectra of E'$_\gamma$ center in an undesified and two densified bulk silica samples, after a γ irradiation of 760 kGy. b) The enhancement of the E'$_\gamma$ center creation efficiency as a function of densification. The two symbols (○ and ●) represent different silica bulk materials. The enhancement quoted is relative to the concentration of the point defects in the undensified silica. All of the samples were γ irradiated at 760 kGy. Figure adapted from Devine et al. [76].

densified samples, in which the point defects are more easily induced and with a different structural configuration.

To the E'$_\gamma$ center is also associated a EPR pair of lines split by ~41.8 mT, commonly indicated as *strong hyperfine structure* of the E'$_\gamma$ center. This doublet, reported in high power second-harmonic EPR (SH-EPR) mode[e] in Figure 1.20(b), originates from the hyperfine interaction of the magnetic moment of the unpaired electron with that of the ^{29}Si nucleus (having spin I=1/2 and a natural abundance ~4.7 %) on which the electron is localized (see Section 2.2.2 for the details on the hyperfine interaction) [2, 71, 78, 79]. First-principle calculations showed that the hyperfine splitting depends on the $Si-\widehat{O}-Si$, $O-\widehat{Si}-O$ bond-angles and Si-O bond-lengths at the oxygen vacancy [80]. Furthermore, it was experimentally found that the hyperfine splitting monotonically increases on increasing the densification, induced in bulk silica samples by hydrostatic press [77]. This effect is evident in Figure 1.20(a), where different EPR spectra acquired for an undesified and different densified

---

[e] SH-EPR mode, discussed in details in Section 3.3.2, reproduces the EPR absorption spectrum and gives a higher sensitivity as compared with FH-EPR mode, which reproduces the derivative of the absorption line. Generally, this latter method is used to detect the main EPR resonance line of the E'$_\gamma$ center, whereas the SH-EPR mode is used for the strong hyperfine structure whose intensity is very low [78].

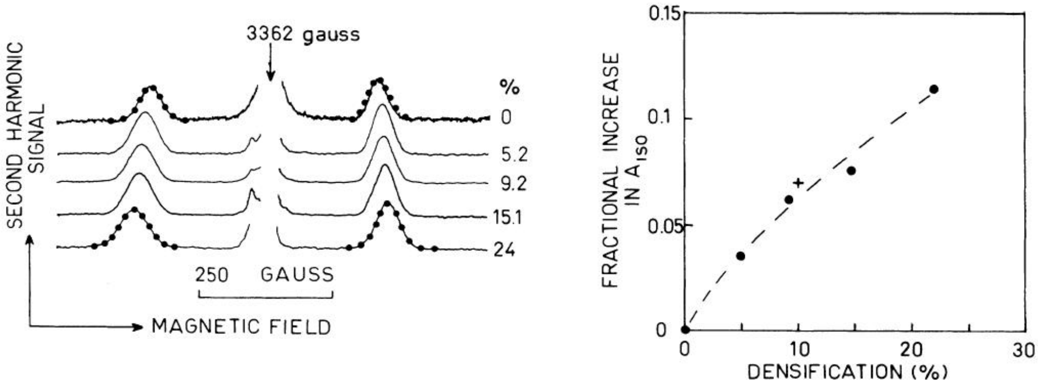

Figure 1.20: a) Strong hyperfine structure of E'$_\gamma$ center in an undesified and various densified bulk silica samples, after a γ irradiation dose of 760 kGy, acquired in high power second-harmonic (SH-EPR) mode. The densification value induced by hydrostatic press is indicated. The central line, largely out of scale, represents the E'$_\gamma$ center. b) Fractional increase of A$_{iso}$, directly estimated from the splitting of the hyperfine structure. The increase is referred to the value estimated for the undesified sample. Figures taken from Devine et al. [77].

bulk silica samples, after the same γ irradiation dose of 760 kGy, are reported [77]. In particular, the constant A^{iso}, the isotropic part of the hyperfine interaction (see Section 2.2.2), for each of these spectra was directly estimated by measuring the peak-to-peak splitting of the strong hyperfine structure of the E'$_\gamma$ center; it is reported as a function of densification in Figure 1.20(b). The authors concluded that the densification results in a reduction in the mean $O-\widehat{Si}-O$ tetrahedral bond angle and in an increase of the mean Si-O bond length on $\equiv Si^{\bullet}$ site.

All of the above findings evidence the fundamental role of the E'$_\gamma$ center in the study of the structural properties of silica. Indeed, its EPR line shape and the splitting of the strong hyperfine structure are commonly considered useful probes of the features of the range-II order. From this point of view, it is hence interesting to investigate by EPR spectroscopy if and how the properties of E'$_\gamma$ center and its strong hyperfine structure change in silica nanoparticles. By photon irradiation at $\sim$10 eV (VUV irradiation) of fumed silica powders with particles of 7 nm mean diameter, it was observed that different kinds of paramagnetic point defects could be detected [37, 81–83]. Among them, it was recognized an EPR signal which was attributed to the E'$_\gamma$ center. In particular, as reported in Figure 1.21(a1), the EPR spectrum acquired at 4.2 K immediately after VUV irradiation showed a central-line signal with an overall

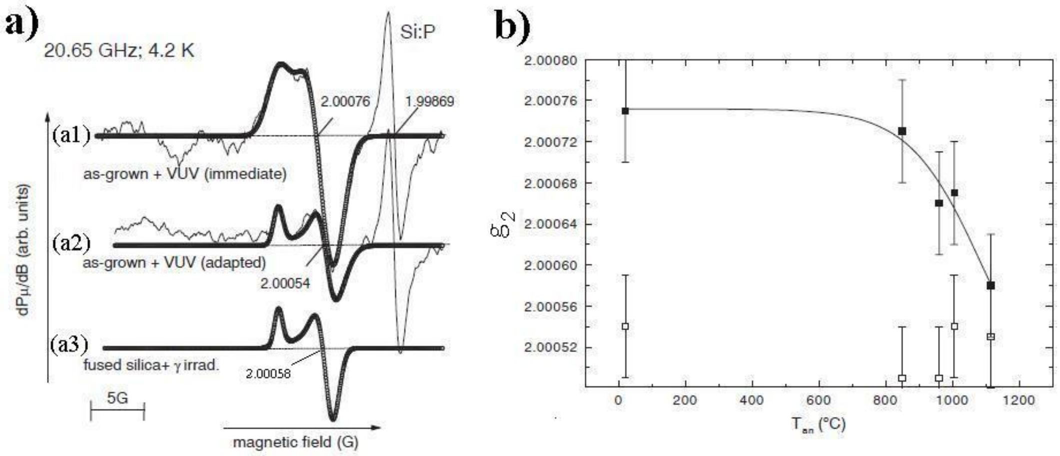

Figure 1.21: a) ESR spectra of E'$_\gamma$ centers measured at 4.2 K in a fumed silica sample a1) immediately after VUV irradiation and a2) several days later, the same sample being left in room ambient. a3) The typical spectrum of bulk silica γ-irradiated at 1 MGy. The thick lines represent spectra simulations. b) Zero-crossing g value (g_2) of the E'$_\gamma$ center as a function of the annealing temperature, measured immediately after VUV irradiation (closed symbols) and several days later (open symbols). Figures taken from Clémer et al. [81].

shape resembling the broadened spectrum of the common E'$_\gamma$ centers of bulk silica (see Figure 1.21(a3) for comparison) [81]. This EPR signal, observed immediately after VUV irradiation, changed when the spectrum of the fumed silica sample was acquired several days later. Indeed, as evident in Figure 1.21(a2), in this latter case the spectrum shows a line shape very similar to that of the common E'$_\gamma$ center. By computer simulations, the authors quantitatively estimated that g_2=2.00076 for the fumed silica sample immediately after VUV irradiation (Figure 1.21(a)), whereas g_2=2.00054 for the same sample several days later Figure 1.21(b). This latter value is very close to that reported for E'$_\gamma$ center in common bulk silica materials (g_2=2.00058 [84]).

Another effect of the "aging" is the decrease of the central-line signal intensity, which is reduced by a factor ∼2 for the spectrum a2) as compared with spectrum a1) in Figure 1.21(a). Besides, a gradual modification of the initial line broadening towards that of bulk silica was also induced by annealing treatments. This trend is shown in Figure 1.21(b), where g_2 measured immediately after VUV irradiation (closed symbols) and after subsequent permanence of the samples for days in room ambient (open symbols) is plotted against temperature annealing (T_{an}). All of these findings were attributed to the presence of two distinct systems of E'_γ centers in fumed silica: one localized in the core part of nanoparticles and the other in their surface region. The point defects of the interior of the nanoparticles exhibit a "bulk" like structure, resulting in E'_γ center line shape very similar to the common E'_γ centers of bulk silica (*bulk* E'_γ *centers*). On the other hand, the E'_γ centers localized in the outer region (indicated hereafter as *surface* E'_γ *centers*) are characterized by different properties, attributed to the more structurally distorted (strained) network of this region of the particle as compared with that of core. By this shell-like model of fumed silica particles, Clémer et al. suggested the following scheme: the E'_γ centers are induced in the whole silica nanoparticle by VUV irradiation [81]. The EPR spectrum acquired immediately after irradiation is characterized by the superposition of signals arising from bulk and surface E'_γ centers (Figure 1.21(a1)). However, on increasing the time after irradiation the surface E'_γ centers, being apt to physical and chemical interactions with the environment, are inactivated (passivated) and leaves only the bulk E'_γ centers (Figure 1.21(a2)). The same effect is induced by annealing treatments: for temperatures $T \gtrsim 1150$ °C sintering takes place decreasing the specific surface area and thereby possibly the number of surface E'_γ centers (compare open and closed symbols in Figure 1.21(b)). Besides, by the observation that the E'_γ density induced in fumed silica, immediately after prolonged VUV irradiation for days-week, was about 100 times smaller than the densities typically observed in bulk silica, the authors suggested that the irradiation resistance of the fumed silica network is due to a good SiO_2 stoichiometry or also by oxygen excess. In other words the fumed silica has a very low density of oxygen vacancies, which are commonly considered as E'_γ center precursors [85, 86].

It is important to note that the concentration of E'_γ centers induced in fumed silica is so low to make the signal of strong hyperfine structure undetectable, indeed the intensity of this latter EPR signal is tens of times lower than that of E'_γ center [2, 71, 78, 79]. However, Stesmans et al. by an opportune treatment, consisting of thermal annealing in vacuum of Si/fumed silica/SiO_2 sandwich (indicated by authors as *SiO-vac. anneal.*), observed a drastic increase of E'_γ center density after a VUV irradiation [87, 88]. In particular, as reported in Figure 1.22(a), the density increases on increasing of annealing temperatures (T_{an}) for SiO-vac. anneal. fumed silica samples (solid symbols), whereas it does not appreciably change with T_{an} for standard fumed silica samples (open symbols). The fumed silica typology considered in this

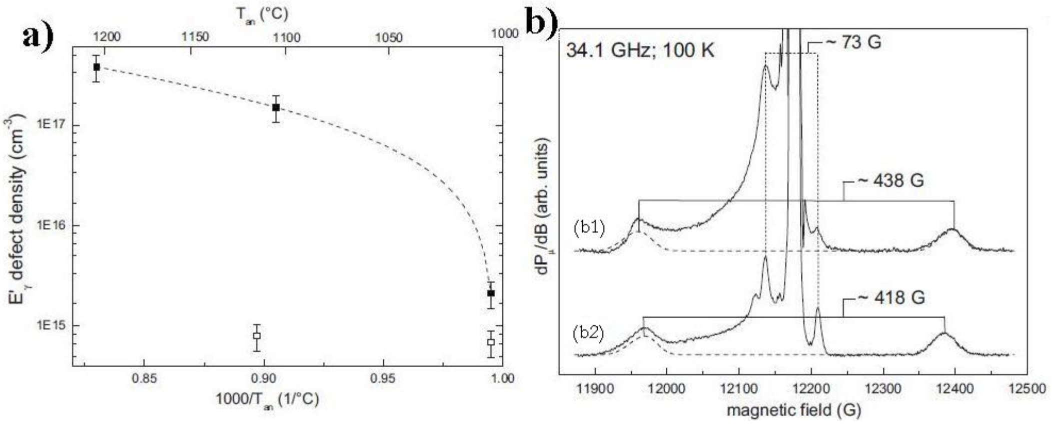

Figure 1.22: a) Defect densities of the E'$_\gamma$ centers in fumed silica subjected to 3 h SiO-vac. anneal. (solid symbols) and 1 h standard vacuum anneal (open symbols) as a function of temperature. All the samples were subjected to 1 h VUV irradiation after the thermal treatments. The measurements were performed immediately after the VUV activation. The dashed curve is a guide for the eye. b) Spectra acquired in SH-EPR mode for: b1) fumed silica subjected to a 1105 °C SiO-vac. anneal. and additional VUV irradiation measured at 100 K, after leaving the samples for substantial time in room ambient; b2) typical spectrum of bulk silica subjected to 100 Mrad by γ-irradiation. The dashed curves represent simulations of the strong hyperfine structure of the E'$_\gamma$ centers. Spectra were aligned at the resonance field of the E'$_\gamma$ central resonance, which is largely out of scale. Figures taken from Clèmer et al. [87].

work was the same used in the previous works (particles with 7 nm diameter). The enhancement of radiation-sensitivity was interpreted in terms of increasing of oxygen vacancies in the fumed silica induced by the Si and SiO_2 slices during the annealing. The analysis of the E'$_\gamma$ line shape for the SiO-vac. anneal. samples suggested that this point defect was mainly induced in the core of the particles, indeed the EPR signal was very similar to that discussed above and reported in Figure 1.21(b). As anticipated, the increase of density of E'$_\gamma$ centers, up to 2×10^{17} cm^{-3} for SiO-vac. anneal. at 1105 °C post VUV irradiated, enabled to detect the strong hyperfine structure, as shown by SH-EPR mode measurements in Figure 1.22(b). In the same figure the typical spectrum of strong hyperfine structure of bulk silica is reported for comparison. It can be clearly seen that the splitting of the strong hyperfine structure of the E'$_\gamma$ center is larger in the fumed silica than for bulk silica. The authors estimated that the splitting is 438 and 418 G for the fumed and bulk silica, respectively. As discussed above, an increase of splitting was observed for bulk silica samples densified under hydrostatic pressure (see Figure 1.20) [77]. From this point of view, the authors suggested that the core network of fumed silica particles is more densified with respect to that of standard bulk silica, corroborating the previous simulative works [39, 40]. On the basis of the data reported in Figure 1.20(b), a quantitative estimation of 5.9 % densification for the particles core was obtained. This high density was attributed to a modification of the n-membered ring distribution in the core network suggesting the presence of more low-membered rings. It is worth noting that these alterations in the core network of particles are too small to induce a detectable change in the E'$_\gamma$ center main EPR line, emphasizing the role of the strong hyperfine structure as a very sensible probe.

Chapter 2

Methodologies

In the present chapter the basic theoretical background useful to understand the experimental investigation we carried out is discussed. In particular the vibrational, photoluminescence and electron paramagnetic resonance spectroscopies are described.

2.1 Vibrational spectroscopy

This Thesis work deals with the investigation of structural modification induced in bulk and nanoparticle silica materials. The study has fruitfully exploited the structural information arising from vibrational spectroscopy, with particular reference to the Raman and IR absorption techniques.

In the IR absorption, light with selected frequencies passes through a sample and the intensity of the signal transmitted in the same direction as the incident one is measured as a function of the frequency. At frequencies corresponding to molecular vibration energies of the sample, some light is absorbed reducing the transmitted intensity. The quantitative relation linking the incident light intensity $I_0(\overline{\nu})$ with the transmitted one $I(\overline{\nu})$ is known as Lambert-Beer's law [89–92]:

$$I(\overline{\nu}) = I_0(\overline{\nu})e^{-\alpha(\omega)d} \tag{2.1}$$

where $\overline{\nu} = 1/\lambda$ is the *wavenumber*, generally expressed in cm^{-1}, d is the path length inside the medium and $\alpha(\omega)$ is the absorption coefficient at frequency $\omega = 2\pi c/\lambda$, c being the light speed and λ the wavelength. The macroscopic parameter $\alpha(\omega)$ is proportional to the number of objects absorbing the light (i.e. intrinsic bridges, point defects embedded in the solid, molecules, etc.) and also to the specific IR transition probability. Since the energies absorbed by the sample correspond to its molecular vibrational frequencies, the typical spectral range of these absorptions is $10^2 \div 10^5$ cm^{-1} (infrared range).

At variance with respect to IR, in Raman spectroscopy we do not observe the transmitted light, but the light scattered from the sample exposed to a monochromatic light source of wavenumber $\overline{\nu}_0$. Due to the isotropic nature of the scattering process, the light diffused by the sample can be measured at any direction with respect to the incident light direction. Typically, a fraction of the order $1/10^3$ of the incident light intensity at the same wavenumber $\overline{\nu}_0$ is scattered in all directions [89–92]. This elastic process, in which the energy of the scattered light is the same of the incident one, is the well known *Rayleigh scattering.* A very small fraction of the order $1/10^6$ of the incident light is not scattered at the same wavenumber $\overline{\nu}_0$ [89–92]. Indeed, this light is characterized by wavenumbers $\overline{\nu}_0 \pm \overline{\nu}_i$ where $\overline{\nu}_i$ corresponds to the molecular vibrational frequencies of the investigated system. This process is called Raman scattering and, as we will discus in detail in Section 2.1.1, it originates from the energy exchanges between the incident photons and phonons of the sample. In particular, the Raman scattered radiation with energy $\text{hc}(\overline{\nu}_0 - \overline{\nu}_i)$ is called *Stokes* radiation and that with energy $\text{hc}(\overline{\nu}_0 + \overline{\nu}_i)$ is called *anti-Stokes* radiation. The Stokes lines are more intense than the anti-stokes lines, whose intensity decreases almost exponentially with the frequency. Typically, energies from near-IR up to visible are considered in the Raman spectroscopy.

It is important to remark that the molecular vibrations involved in the Raman process are not necessarily the same as those excited by the IR absorption process. In this sense it is usually said that Raman and IR absorption techniques are complementary [89–92]. In the following sections, a theoretical approach will be carried out to explain the Raman and IR absorption processes as well as their selection rules. For this reason, it is useful to introduce some quantum mechanics concepts.

The Hamiltonian of a molecule with n electrons (mass m and coordinate r_i) and N nuclei (mass M_α and coordinate R_α) can be written as [91–93]:

$$\hat{H} = T_e + T_N + V_{e-e} + V_{N-N} + V_{e-N} \tag{2.2}$$

where $T_e = -\frac{1}{2m}\sum_{k=1}^{n} \hbar^2 \frac{\partial^2}{\partial r_k^2}$ represents the kinetic energy of the electrons, $T_N = -\sum_{l=1}^{N} \frac{\hbar^2}{2M_l}\frac{\partial^2}{\partial R_{l2}}$ represents the kinetic energy of the nuclei, $V_{e-e} = \frac{1}{2}\sum_{k\neq s} \frac{e^2}{|r_k - r_s|}$ is the potential energy term associated to the electron-electron interaction, $V_{N-N} =$

$\frac{1}{2}\sum_{l\neq t}\frac{e^2 Z_l Z_t}{|R_l-R_t|}$ is the potential energy term associated to the nuclei-nuclei interaction and finally $V_{e-N} = -\sum_{k\neq l}\frac{e^2 Z_l}{|R_l-r_k|}$ is the potential energy term associated to the electrons-nuclei interaction. An exact solution of the corresponding Schrödinger equation $H\psi(r,R) = E\psi(r,R)$, where $\psi(r,R)$ and E are the wave function and the energy eigenvalue, is difficult to be obtained and therefore some approximations are required. Since the ratio between nuclear and electronic masses is very high ($M_\alpha/m \sim 10^3 \div 10^5$), while the forces to which the electrons and nuclei are subjected are of comparable intensity, it is reasonable to assume that the electrons move much faster than the nuclei. It means that motions of electrons and nuclei are approximately independent (Born-Oppenheimer approximation): the electronic cloud reorganizes quickly itself during the slow displacement of the nuclei and from the point of view of nuclei this electronic cloud generates an energy appearing as a global electrostatic potential, which is the mean of T_e, V_{e-e} V_{e-N}. On the basis of this consideration, the state of the system can be described as the tensorial product of an electronic wave function $\phi_i(r,R)$, depending on both nuclear (R) and electronic (r) coordinates, and a nuclear wave function $\chi_{i,j}(R)$, depending only on the nuclear coordinates:

$$\psi_{i,j}(r,R) \sim \phi_i(r,R)\chi_{i,j}(R) \tag{2.3}$$

where i and j are quantum numbers describing the electronic and vibrational state, respectively. Consequently, the Schrödinger equation that describes the wave functions of the system can be separated in two parts [91–94]:

$$[T_e + V_{e-e}(r,R) + V_{e-N}(r,R)]\phi_i(r,R) = \varepsilon_i(R)\phi_i(r,R) \tag{2.4}$$

$$[T_N + V_{N-N}(R) + \varepsilon_i(R)]\chi_{i,j}(R) = E_{i,j}\chi_{i,j}(R) \tag{2.5}$$

where $\varepsilon_i(R)$ and $E_{i,j}$ are the electronic and nuclear energy eigenvalues. Equation 2.4 describes the electrons moving in the field of the fixed nuclei. It is worth noting that the potential energies $V_{e-e}(r,R)$ and $V_{e-N}(r,R)$ change on varying the nuclei position R and then the eigenfunctions $\phi_i(r,R)$ and energy eigenvalues $\varepsilon_i(R)$ of the electrons depend parametrically on R. On the other hand, Equation 2.5 describes the nuclei motion, which depends on the electronic state through the $\varepsilon_i(R)$ term. The total energy of the system ($E_{i,j}^{TOT}$) can then be written as [91–94]:

$$E_{i,j}^{TOT} = \varepsilon_i(R) + E_{i,j} \tag{2.6}$$

In order to solve the electronic and nuclear Schrödinger equations, one must first consider a fixed position of nuclei and find the eigenvalues $\varepsilon_i(R)$ of Equation 2.4; afterwards, it is possible to solve Equation 2.5 with a proper potential energy term $\mathrm{V}_{N-N}(\mathrm{R})$, which depends on the considered system. It is important to note that in this procedure the stability of the system must always be satisfied. Assuming the system in a stable configuration (i.e. in a energy local minimum) and in the case of small nuclear motions (*harmonic approximation*), the nuclear cartesian coordinates R can be expressed in terms of the *normal coordinates* Q[a] and the nuclear eigenfunctions $\chi(R)_{i,j}$ of Equation 2.5 can be written as the product of independent harmonic oscillators, one for each normal coordinate Q_a [91–94]:

$$\chi_{i,j}(Q) = \prod_{a=1}^{P} \chi_{i,j_a}(Q_a) \tag{2.7}$$

where P is the number of the normal coordinates associated with the system. The nuclear energy eigenvalues are therefore [91–94]:

$$E_{i,j} = \sum_{a=1}^{P} \hbar\omega_{i,a}\left(j_a + \frac{1}{2}\right) \tag{2.8}$$

where $\hbar$ is the Planck constant divided by 2π, $\omega_{i,a}$ is the vibrational frequency of the Q_a-th normal mode and the quantum number j_a can have the values 0, 1, 2, 3.... In order to visualize the distribution of the vibrational energies, an analytic form of the electron energy ε_i is required. For this reason, it is useful to consider a single normal vibration mode Q_a associated with a generic electronic state of energy $\varepsilon_i(Q_a)$. Indicating with $Q_a = Q_{a_0}$ the normal vibration coordinate where $\varepsilon_i(Q_a)$ has a minimum and since the nuclear motion is generally confined to a small range of Q_a close to Q_{a_0}, we can expand $\varepsilon_i(Q_a)$ around Q_{a_0} [91–94]:

$$\varepsilon_i(Q_a) = \varepsilon_i(Q_{a_0}) + (Q_a - Q_{a_0})\left(\frac{d\varepsilon_i}{dQ_a}\right)_{Q_a = Q_{a_0}} + \frac{1}{2}(Q_a - Q_{a_0})^2\left(\frac{d^2\varepsilon_i}{dQ_a^2}\right)_{Q_a = Q_{a_0}} + \cdots \tag{2.9}$$

Since $\varepsilon_i(Q_a)$ has a minimum by definition, the second term on the right of Equation 2.9 vanishes. Finally, neglecting terms higher than $(Q_a - Q_{a_0})^2$, we can represent the

---

[a] The normal coordinates refer to the positions of atoms away from their equilibrium positions. Each normal coordinate is assigned to a single *vibration normal mode*: a collective motion of all the atoms in the molecule where each atom moves in phase with each other at a particular frequency [91–94].

electronic energy by the parabolic approximation [91–94]:

$$\varepsilon_i(Q_a) = \varepsilon_i(Q_{a_0}) + \frac{1}{2}K_{i,a}(Q_a - Q_{a_0})^2 + \cdots \tag{2.10}$$

where

$$K_{i,a} = \left(\frac{d^2\varepsilon_i}{dQ_a^2}\right)_{Q_a=Q_{a_0}} = (\hbar\omega_{i,a})^2 \tag{2.11}$$

It is important to remark that when the system occupies the lower vibrational levels, the parabolic approximation is valid. However, for higher energies (higher vibrational levels) this simple approximation is not longer valid and the anharmonic effects should be considered (the terms we have neglected in Equation 2.9). In Figure 2.1, the electronic energy $\varepsilon_i(Q_a)$ obtained from Equation 2.10 is reported as a function of Q_a. The horizontal lines represent the vibrational energies associated to the normal vibration mode with different quantum numbers j_a, as reported in Equation 2.8.

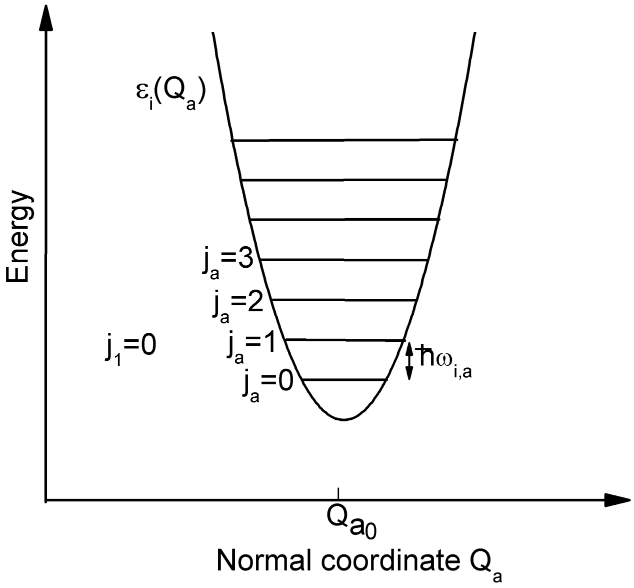

Figure 2.1: The electronic energy as a function of normal coordinate Q_a, obtained in the parabolic approximation. The horizontal lines represent the energy levels attributed to the normal vibration mode with different quantum numbers j_a.

The normal modes of vibration for a nonlinear molecule containing N atoms are 3N-6, whereas for a linear molecule they are 3N-5. Generally, these vibration modes for a molecule can be distinguished in two classes: *stretching mode*, when the length of a chemical bond changes with fixed bond-angles, and *bending mode*, when the bond-angles change with fixed bond-lengths. These two classes can be further subdivided into different types, depending on how the atoms move relative to each other. Stretching vibrational can be symmetric or anti-symmetric, while bending vibrational is generally distinguished in scissoring, rocking, wagging and twisting vibrational.

2.1.1 Raman scattering

As anticipated before, the vibration transitions involved in the Raman spectrum arise from physical process different from those determining the IR absorption. In this section the origin of the Raman scattering process is explained by using a classical approach.

If a molecule is placed in an electric field E, a dipole moment p_{ind} is induced in the molecule because the force ($\mathbf{F} = q\mathbf{E}$, where q is the charge) acting on nuclei and electrons is directed in opposite directions [89–92]. The induced dipole is approximately proportional to the force by the factor α, commonly called *polarizability* [89–92]:

$$p_{ind} = \alpha E \tag{2.12}$$

The polarizability measures the ease with which the electron cloud around a molecule can be distorted. Now we consider an electromagnetic field whose electric field oscillates at the frequency ω_0 as:

$$E = E_0 cos(\omega_0 t) \tag{2.13}$$

where E_0 is the maximum value of the electric field. The induced dipole momentum of a molecule in this oscillating field is:

$$p_{ind} = \alpha E_0 cos(\omega_0 t) \tag{2.14}$$

If the polarizability were a constant value, the induced dipole moment should oscillate at the same frequency ω_0. However, as said in the previous section, the molecules oscillate at the frequencies associated with their normal vibration modes and, in principle, these oscillations could effect the dipole momentum through, for example, the polarizability. For simplicity, we consider the case of a diatomic molecule which is characterized by only the stretching vibration mode. If we indicate with ω_m the frequency of this vibration mode and with Q the normal coordinate, the time dependence of this latter can be expressed as [89–92]:

$$Q = Q_0 cos(\omega_m t + \varphi) \tag{2.15}$$

where Q_0 is the maximum value of vibration amplitude and φ is the phase. The exact law of the polarizability variation induced by the molecular vibration is not known, however for vibrations of small amplitude, α can be approximated through the expansion up to first order in Q around $Q = 0$:

$$\alpha \sim \alpha_0 + \left(\frac{\partial\alpha}{\partial Q}\right)_{Q=0} Q \tag{2.16}$$

where α_0 and $\partial\alpha\ /\partial Q$ are the polarizability and the rate of change of α with respect to the change of Q, both estimated at the equilibrium position $Q = 0$. Finally, by combining Equations 2.14, 2.15 and 2.16 we obtain [89–92]:

$$p_{ind} = \alpha_0 E_0 cos(\omega_0 t) + \left(\frac{\partial\alpha}{\partial Q}\right)_{Q=0} Q_0 E_0 cos(\omega_m t + \varphi) cos(\omega t) = \tag{2.17}$$

$$= \alpha_0 E_0 cos(\omega_0 t) + \frac{Q_0 E_0}{2}\left(\frac{\partial\alpha}{\partial Q}\right)_{Q=0} cos[(\omega_0 - \omega_m)t + \varphi] + \frac{Q_0 E_0}{2}\left(\frac{\partial\alpha}{\partial Q}\right)_{Q=0} cos[(\omega_0 + \omega_m)t + \varphi] \tag{2.18}$$

where we used $cos(a)cos(b) = 1/2[cos(a - b) + cos(a + b)]$. Equation 2.18 shows that the motion of the induced dipole moment has components oscillating at ω_0, $\omega_0 - \omega_m$ and $\omega_0 + \omega_m$. Then, the oscillating electric dipole radiates electromagnetic waves at frequency ω_0 (Rayleigh scattering), $\omega_0 - \omega_m$ (Stokes radiation) and $\omega_0 + \omega_m$ (anti-Stokes radiation). It is worth noting that, in general, the Rayleigh scattering is coherent because it is in phase with the incident electromagnetic field, whereas the Raman scattering is incoherent as the consequence of the φ term, which in an ensemble of molecules depends on the given molecule. It is evident, by looking at Equation 2.18, that the Raman scattering occurs because a molecular vibration can change the polarizability. As a consequence, the selection rule for a Raman-active vibration requires that the polarizability changes during the vibration, that is [89–92]:

$$\left(\frac{\partial\alpha}{\partial Q}\right)_{Q=0} \neq 0 \tag{2.19}$$

The vibrations of a highly polar moiety, such as the O-H bond, are usually weakly Raman-active because an external electric field can not induce a large change in the dipole moment. In the case of linear triatomic molecules, such as CO_2 molecule, characterized by three normal vibration modes (symmetric stretching, asymmetric stretching and bending), only the bending mode is Raman-active whereas the other two are very weakly Raman-active. Through the group theory, it is straightforward to show that if a polyatomic molecule has a center of symmetry, vibrations that are Raman-active will be IR-inactive, and vice versa [91, 92].

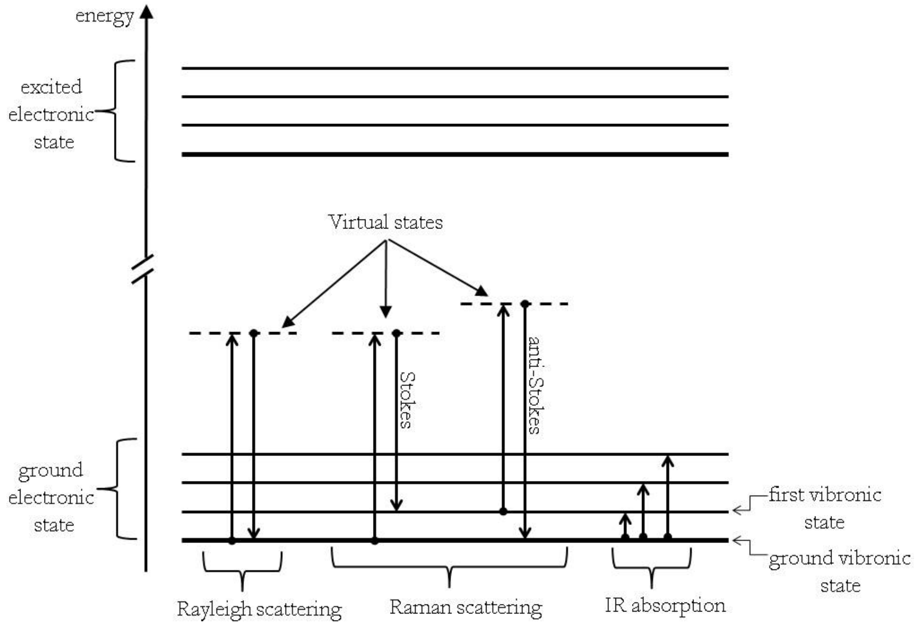

Figure 2.2: Energy levels scheme in which the Rayleigh, Raman and IR transitions are depicted.

The classical model, used to obtain Equation 2.18, correctly predicts the existence of the Raman activity in terms of the Stokes and anti-Stokes lines. However, this model predicts an incorrect intensity ratio between Stokes and anti-Stokes lines, that is:

$$\left(\frac{I_{Stokes}}{I_{anti-Stokes}}\right)_{classic} = \left(\frac{\omega_0 - \omega_m}{\omega_0 + \omega_m}\right)^4 < 1 \tag{2.20}$$

instead, experimentally, the Stokes lines are more intense than the anti-Stokes ones.

The correct intensity ratio is obtained by quantum theory in which the Raman scattering as well as the Rayleigh scattering are treated as a second order process [93, 95].

Considering the discussion reported in the previous section, in the first step, a photon of energy $\hbar\omega_0$ is absorbed, exciting the system from a vibronic state a to a virtual state f; in the second step, the excited molecule emits a photon of energy $\hbar\omega'$ and is de-excited from the virtual state f to a final vibronic state b. If the final state b of the system is the same as the initial state a, the emitted radiation has the same frequency as the incident radiation (Rayleigh scattering); on the contrary, if the final state is different from the initial state, the scattering is inelastic and the Raman scattering occurs. These processes are schematically shown in Figure 2.2, where the Stokes and anti-Stokes radiations are, for example, originated from the processes: (ground vibronic state)⇒(virtual state)⇒(first excited vibronic state) and (first excited vibronic state)⇒(virtual state)⇒(ground vibronic state), respectively. In this scheme, the Stokes lines are more intense than the anti-Stokes lines because generally the ground vibronic state is more populated than states with higher energy, as natural consequence of the Boltzmann distribution.

2.1.2 Infrared absorption

In this section, we will introduce the physical origin of the IR absorption and we will give the selection rules associated to these vibration transitions. Generally, heteronuclear diatomic molecules are characterized by a permanent dipole moment p as a consequence of the fact that one atom will be more electronegative than the other and then it will have a net negative charge. Obviously, this permanent dipole moment oscillates at the same frequency associated to the vibration of the considered molecule. This oscillating permanent dipole moment can interact with an external oscillating electric field and absorbs energy from this if the field also oscillates at the same frequency ω. Therefore, the selection rule for an IR-active vibration requests that the permanent dipole moment changes during the vibration of the normal mode, that is [89–92]:

$$\left(\frac{\partial p}{\partial Q}\right) \neq 0 \tag{2.21}$$

It is worth noting that this condition in a generic polyatomic molecule is strongly related with the considered normal vibration mode. For example, in the triatomic molecule CO_2 (the same case reported above for Raman scattering) the asymmetric stretching and bending vibration modes are IR-actives, whereas the symmetric stretching is IR-inactive. All these considerations give a simplified molecular picture of the IR spectroscopy principle. From a quantum mechanics point of view, the IR absorption originates from the transitions induced by IR electromagnetic field between different vibrational states of the same electronic level [91, 92, 96]. In Figure 2.2, some typical IR transitions from the ground vibronic state are reported. In particular, the transition from the ground state to the first excited vibronic state is called the *fundamental transition*, whereas the transitions from the ground state to the second and third excited vibronic states are the *first* and *second overtone*, respectively. In the harmonic approximation, it is possible to show that the allowed transitions are those with $j_a - j'_a = \pm 1$, where j_a and j'_a are the quantum numbers characterizing the vibrational energy levels involved in the transitions [91, 92, 96]. From this point of view, the fundamental transition is an allowed transition, whereas the first and second overtones are forbidden. However, as discussed in Section 2.1, the harmonic picture is only an approximation. In many cases of interest, a more sophisticated treatment is necessary which shows that overtone transitions occur, but the amplitudes are usually one order of magnitude weaker than that of the fundamental transition. From a quantum mechanics point of view, the probability that the electromagnetic radiation induces an electronic transition from the initial state $\psi_{i,j}(r,Q)$ to the final state $\psi_{f,j'}(r,Q)$ is proportional to the Einstein absorption coefficient $B_{i,f}$ [91, 93]:

$$B_{i,f} = \frac{2\pi}{3\hbar^2 C} |\hat{M}^{i,f}|^2 \tag{2.22}$$

where

$$\hat{M}^{i,f} = \iint dr\, dQ\, \psi^*_{f,j'}(r,Q)\, p\, \psi_{i,j}(r,Q) \tag{2.23}$$

is the electric dipole matrix element and p is the electronic dipole moment of the system.

2.2 Electron paramagnetic resonance spectroscopy

The electron paramagnetic resonance (EPR) spectroscopy can be applied to systems characterized by an electronic magnetic dipole moment $\mu \neq 0$, as for example atoms and molecules with an odd number of electrons or partially filled shell, paramagnetic point defects, transition metal and rare earths ions.

When a generic paramagnetic center is embedded in a solid, its properties strongly depend on the interactions that it establishes with surroundings ions of the solid. In order to consider these contributions, two different methods can be used [97, 98]. The former, called the *crystalline field method*, assumes that the electronic wave function of the paramagnetic center is highly localized on a single ion and that the only effect of the surrounding ions on the paramagnetic center is to produce an electric field (crystal field), which is experienced by the center. The symmetry of this field reflects that of its sources, that is the lattice symmetry. The effect of the crystal field on the paramagnetic center is to separate its energy levels by Stark effect, originating from the interaction of the electric dipole moment $\mathbf{p}$ of the center with the crystalline field $\mathbf{E}$ ($H_{Stark} = -\mathbf{p} \cdot \mathbf{E}$). This approach, which greatly simplifies the interaction of the center with its surrounding, has the limit to be exclusively applied to systems with purely ionic bonds.

The second method is more sophisticated and consists in considering the electronic wave function distributed over a group of atoms forming molecular orbitals of type σ and π [97, 98]. This method has the advantage, as compared with the crystalline field method, to be also applied to systems with covalent bonds. It is important to remark that both these methods lead to a similar result: the appearance of groups of degenerate or almost degenerate energy levels, depending strongly on the symmetry of the surrounding of the center. This result is also confirmed, at least for the ground state of the system, by the *Kramers theorem*, which states that the ground state of a paramagnetic system with an odd number of electrons and in the absence of external magnetic field has at least a double degeneracy [97–99].

As we will discuss in more details in the following sections, in an EPR experiment the degenerate ground state of the investigated paramagnetic system is split by a static magnetic field (Zeeman effect) of about $10^{-2} \div 1$ cm^{-1}: so through an opportune electromagnetic field some transitions are induced between these split states. The aim of the EPR spectroscopy is not to study the complex distribution of the whole energy spectrum of the considered center, but rather to investigate the energy levels involved in the transitions. In order to describe the effects of the static magnetic field on the ground state of the center, a useful formalism is that of the *effective spin Hamiltonian* (or simply *spin Hamiltonian*). This method assumes that the ground state of a paramagnetic center possesses a given value of the spin S, called the effective spin. This value, generally different from the true value of the spin of the ground state, represents a fictitious spin chosen in such a way that $2S+1$ corresponds with the degeneracy of the group of levels considered.

2.2.1 Spin Hamiltonian: Zeeman interaction

In this section, we report the spin Hamiltonian of a solid, containing a given species of paramagnetic center characterized by $S = 1/2$, exposed to a static and uniform magnetic field $\mathbf{H}$. The interaction of the external magnetic field with the magnetic moment associated with the center can be described by the Zeeman operator [97–101]:

$$H_{Zeeman} = -\mu \cdot \mathbf{H} = \mu_B \mathbf{S} \cdot \hat{g} \cdot \mathbf{H} \tag{2.24}$$

where μ is the magnetic moment associated to S, $\mu_B = 9.27408 \cdot 10^{-24}$ J/T is the Bohr magnetic moment and

$$\hat{g} = g_e \mathbf{1}_3 + 2\lambda_{LS}\hat{A} \tag{2.25}$$

g_e=2.0023 being the free electron splitting factor, $\mathbf{1}_3$ the 3×3 unit matrix, λ_{LS} the spin-orbit coupling constant and $\hat{A}$ a tensorial quantity originating from the spin-orbit interaction. In Equation 2.24, the interactions of the paramagnetic center with its environment are taken into account through the spin-orbit coupling ($\lambda_{LS}\hat{A}$). Indeed, if the paramagnetic center were isolated the Zeeman operator should be simply rewritten as $g_e \mu_B \mathbf{S} \cdot \mathbf{H}$.

It is worth noting that the operator of Equation 2.24 is applied to the ground state of the paramagnetic center, assuming that it does not have orbital degeneracy (angular momentum L=0). This latter hypothesis is not highly restrictive because the Jahn-Teller theorem states that a non-linear molecule in a degenerate orbital state is subjected to distortions resulting in the reduction of the symmetry and thus in the removal of the degeneracy [94, 98, 99]. Furthermore, using the crystalline field method, it can be shown that the effect of the electric field on the ground state of the center is to bring to zero the value of the electronic orbital magnetic moment $\mu_L \propto$L (*quenching* of the orbital angular momentum).

The energy levels of the system, obtained from Equation 2.24, are:

$$E_{Zeeman} = g\left(\theta_1, \theta_2, \theta_3\right) \mu_B H m_S \tag{2.26}$$

where $m_S = \pm 1/2$ are the eigenvalues of the component of **S** along the direction of **H** and

$$g\left(\theta_1, \theta_2, \theta_3\right) = \sqrt{g_1^2 cos^2\theta_1 + g_2^2 cos^2\theta_2 + g_3^2 cos^2\theta_3} \tag{2.27}$$

g_i being the principal values of the matrix $\hat{g}$ and θ_i the angles between the direction of the static magnetic field and the principal axes of the $\hat{g}$ tensor. The effect of the Zeeman interaction is to remove the degeneracy of the ground state related to the different possible values of the quantum number m_S.

In the EPR experiments an oscillating magnetic field of amplitude H_1 perpendicular to **H** and with $\mathrm{H}_1 \ll \mathrm{H}$ is used to induce transitions between the two states split by Zeeman interaction. Since the field $\mathbf{H}_1$ oscillates at frequency ω, the transitions can occur when the energy $\hbar\omega$ of the oscillating magnetic field is the same as the energy difference of the two states (*resonance condition*):

$$\hbar\omega = \Delta E_{Zeeman} = g\left(\theta_1, \theta_2, \theta_3\right) \mu_B H \tag{2.28}$$

An EPR spectrum is usually obtained by measuring the energy absorbed by the paramagnetic system as a function of the amplitude of the static magnetic field **H** at fixed frequency of the oscillating magnetic field [97–101].

2.2.2 Spin Hamiltonian: hyperfine interaction

When n atoms with non-zero nuclear spin are located nearby to the paramagnetic center, a new interaction, called *hyperfine interaction*, occurs [94, 97, 99, 101]. The Hamiltonian operator associated with this interaction is:

$$H_{hf} = \sum_{i=1}^{n} \mathbf{S} \cdot \hat{A}_i \cdot \mathbf{I}_i \tag{2.29}$$

where $\mathbf{I}_i$ is the nuclear spin of the i-th atom and $\hat{A}_i = A_i^{iso}\mathbf{1}_3 + \hat{T}_i$ is the hyperfine tensor. The hyperfine interaction is characterized by two different contributions. The first ($A_{iso}\mathbf{1}_3$) is an isotropic term, called *Fermi contact term*, which is of genuine quantum nature and is related to the wave function features of the considered state. The second ($\hat{T}$) is an anisotropic term, called *dipolar term*, originating from the dipole-dipole interaction of the electronic magnetic moment with the nuclear magnetic moment μ_n associated to **I**.

It is important to remark that in general the principal axes of the tensor $\hat{A}$ differ from those of the tensor $\hat{g}$, especially when the interaction is due to a nuclear magnetic moment of an atom different from that on which the electron is localized. This makes the study of the total spin hamiltonian (Zeeman, spin-orbit and hyperfine interactions) hard. However, in many cases of interest, as that considered in this Thesis, the axes of the two tensors can be considered the same. Moreover, since generally the hyperfine terms are smaller than the Zeeman one, first order perturbation theory can be applied. As a consequence, we consider first the Zeeman and spin-orbit terms (see Equation 2.24) and then the hyperfine ones. Indicating with z-axis the direction of the static magnetic field, and in the simple case in which the paramagnetic center with $S = 1/2$ interacts with only one atom with $I = 1/2$, the energy eigenvalues are:

$$E = g\left(\theta_1, \theta_2, \theta_3\right) \mu_B H m_S + A\left(\theta_1, \theta_2, \theta_3\right) m_S m_I \tag{2.30}$$

where $m_I = \pm 1/2$ are the eigenvalues of the component of $\mathbf{I}$ along the z-direction and

$$A(\theta_1, \theta_2, \theta_3) = \frac{1}{g(\theta_1, \theta_2, \theta_3)} \sqrt{g_1^2 A_1^2 cos^2\theta_1 + g_2^2 A_2^2 cos^2\theta_2 + g_3^2 A_3^2 cos^2\theta_3} \tag{2.31}$$

In a similar way to the Zeeman interaction, the effect of the hyperfine interaction is to remove the degeneracy of the states characterized by different values of m_I. Considering that the selection rules for the transition induced by the oscillating magnetic field are $\Delta m_I = 0$ and $\Delta m_S = \pm 1$, in this case the resonance condition is:

$$\hbar\omega = g\left(\theta_1, \theta_2, \theta_3\right) \mu_B H \pm \frac{1}{2} A\left(\theta_1, \theta_2, \theta_3\right) \tag{2.32}$$

The energy levels scheme for a system with $S = I = 1/2$ is shown in Figure 2.3. The transition indicated by the letter “a”, occurring in the presence of only Zeeman interaction, is replaced by the “b” and “c” transitions when the hyperfine interaction is present.

2.2.3 Bloch’s equations

When n paramagnetic centers are embedded in a solid, the mutual interactions that the centers establish each other (spin-spin interactions) and the interactions between them and the lattice (spin-lattice interactions) must be taken into account, in

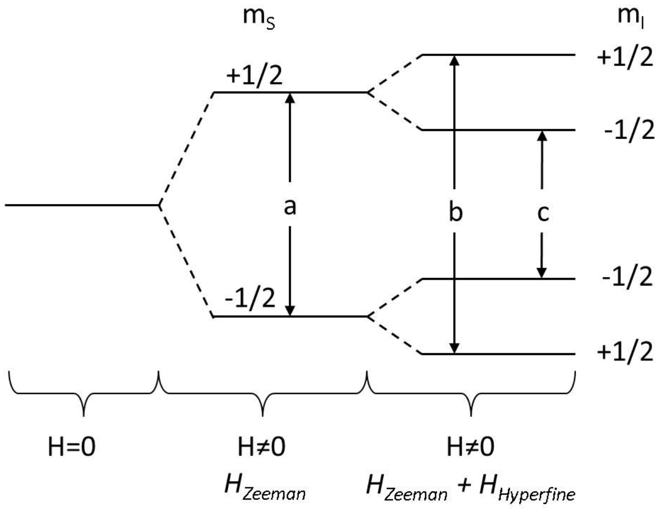

Figure 2.3: Schematic energy levels distribution for a spin system with $S = I = 1/2$ in the case of H=0 and H≠0 (Zeeman and hyperfine interaction). It is important to note that energy level separations are not in scale and the allowed EPR transitions are highlighted by arrows.

addition to the interactions with the external magnetic field above discussed. A phenomenological description of the behaviour of such a system is given by the Bloch's equations [98, 99, 102]. These equations describe the interactions of the macroscopic components of the magnetization $\mathbf{M} = \frac{1}{V}\sum_i^n \mu_i$ of a solid, where V is the system volume, with the static and oscillating magnetic fields. Two phenomenological time constants, T_1 (*longitudinal* relaxation time) and T_2 (*transversal* relaxation time), are introduced in order to take into account the spin-lattice and spin-spin interactions, respectively. The Bloch's equations are:

$$\frac{dM_x(t)}{dt} = \gamma[\mathbf{H}_T \times \mathbf{M}(t)]_x - \frac{M_x(t)}{T_2} \tag{2.33}$$

$$\frac{dM_y(t)}{dt} = \gamma[\mathbf{H}_T \times \mathbf{M}(t)]_y - \frac{M_y(t)}{T_2} \tag{2.34}$$

$$\frac{dM_z(t)}{dt} = \gamma[\mathbf{H}_T \times \mathbf{M}(t)]_z - \frac{M_z(t) - M_0}{T_1} \tag{2.35}$$

where $\gamma = g_e\mu_\beta/\hbar$ is the gyromagnetic ratio ($\gamma = 1.76 \cdot 10^{11} s^{-1} T^{-1}$ for a free electron), $\mathbf{H}_T$ is the total magnetic field (static and oscillating) and M_0 is the modulus of the magnetization of the paramagnetic system obtained in stationary conditions, supposed to be directed along the direction of $\mathbf{H}$ ($\mathbf{H} = (0, 0, H)$) with $H_1 \ll H$. As we will discuss in more details in Section 3.3.2, in order to enhance the sensitivity of the EPR spectrometer, a modulating magnetic field of amplitude H_m and frequency ω_m (much lower than the frequency ω of $\mathbf{H}_1$) is usually superimposed parallel to $\mathbf{H}$. The solution of the Equations 2.33, 2.34 and 2.35 strongly depends on the time dependence of the magnetic fields $\mathbf{H}_1$ and $\mathbf{H}_m$. An analytical solution of this set of equations is difficult to be obtained and as a consequence different specific cases have to be considered. The most important one occurs when:

$$\frac{H_1}{\frac{d(H+H_m)}{dt}} \ll \sqrt{T_1 T_2} \tag{2.36}$$

which is called *slow-passage condition* [103]. Roughly speaking, it means that the rates of time change of $\mathbf{H}$ and $\mathbf{H}_m$ are slow with respect to the main relaxation rates of the paramagnetic centers. In this case an analytic solution of the the Bloch's equations can be easily obtained and the power P absorbed by a number N of paramagnetic centers per unit of volume, averaged on a wave period of $\mathbf{H}_1$ can be derived [98, 99]:

$$P \propto \frac{N H_1^2}{1 + (\gamma H - \omega)^2 T_2^2 + \gamma^2 H_1^2 T_1 T_2} \tag{2.37}$$

As already observed, the resonance condition occurs for $\gamma H = \omega$. When $\gamma^2 H_1^2 T_1 T_2 \ll 1$ (*non saturation condition*), the resonance absorption is proportional to H_1^2 and is characterized by a Lorentzian shape. In this case, the area of the absorption curve is proportional to the concentration N of the centers. At variance, when $\gamma^2 H_1^2 T_1 T_2 \gg 1$ (*saturation condition*), the line shape of the absorbed power deviates from a Lorentzian shape and assumes a constant value independent of H_1^2 at resonance [98, 99]. As we will discus in Section 3.3.2, the above treatment typically applies to the FH-EPR spectra.

When the slow-passage condition (Equation 2.36) is not satisfied and

$$\frac{H_1}{\frac{d(H+H_m)}{dt}} \gg \sqrt{T_1 T_2} \tag{2.38}$$

an analytic solution of the the Bloch's equations is difficult to be obtained, a more empirical experimental approach is used to investigate the resonance phenomenon.

Equation 2.38 is called *rapid-passage condition.* This condition is frequently used in EPR experiments because, upon opportune instrumental setting, it enables to have high sensitivity. Further comments on this more experimental approach will be given in Section 3.3.2. This rapid condition is the physical condition giving origin to SH-EPR spectra.

2.2.4 The EPR line shape of the amorphous materials

In the previous sections, we considered a paramagnetic center embedded in a solid and we showed the close relationship between the direction of the external magnetic field and the axes of symmetry of the center in determining the resonance condition. When the paramagnetic centers are embedded in an amorphous solid as well as in powders of a crystalline material, the lack of spatial periodicity has to be considered. Indeed, for these systems the orientations between the magnetic field and the axes of the center are random. Therefore, for any arbitrary direction of the static magnetic field, a distribution of the resonance fields appears. Moreover, the distributions of the bond-angles and bond-lengths, characterizing amorphous solids, tend further to distribute the parameters characterizing a given center. As a consequence the centers have different principal values of the tensors $\hat{g}$ and $\hat{A}$, resulting in an inhomogeneous broadening of the absorption curves. All of these effects make the investigation of the centers embedded in an amorphous material harder as compared with the investigation of the same centers embedded in a crystalline solid. However, the principal values of $\hat{g}$ and $\hat{A}$ can be experimentally estimated by measuring the field values corresponding to specific features in the EPR spectrum. For example, the principal values of the $\hat{g}$ tensor for a center with orthorhombic symmetry can be experimentally estimated, as discussed in Section 1.3.3, by the field values at which the first maximum (g_1), the zero-crossing point (g_2), and the minimum (g_3) of the EPR spectra in FH-EPR mode occur.

2.3 Photoluminescence spectroscopy

In Section 2.1, we introduced the Lambert-Beer's law (see Equation 2.1) to describe the absorption of the light between vibrational energy levels belonging to the electronic ground state when the investigated material is exposed to IR radiation. The Lambert-Beer's law is also valid when visible or ultraviolet (UV) excitation radiation is used. In these cases, the absorbed light can induce transitions from the ground state of the considered system towards one of its electronic excited states. Generally these transitions are due to the presence in the material of point defects, which introduce electronic energy levels localized between the valence and conduction bands of the considered material. Typically, when the point defects are embedded in an amorphous solid, the absorption bands associated to the transition between the energetic levels of these defects have approximately a gaussian shape. This is originated from the interactions of the point defects with the atomic vibrations and from the inhomogeneities of the local structure inherent to the solid.

After visible or UV absorption, the concomitance of different physical processes occurs in order to carry back the system in the ground state. To illustrate these processes we refer to the Jablonski diagram of Figure 2.4, where a generic energy level scheme, constituted by electronic spin singlet states (the ground state S_0 and the excited state S_1) and by a spin triplet state (T_1), is shown [92]. It is worth noting that by definition S_0 is characterized by two electrons in the same orbital state but with opposite spin orientation, S_1 by two electrons occupying different orbital states with opposite spin orientation and, finally, T_1 by the two electrons occupying different orbital states with the same spin orientation. Each electronic state is accompanied by a series of molecular vibrational states, which are represented as thin lines in Figure 2.4.

As already stated many different processes occur after the electronic excitation. They can be grouped in *non-radiative* and *radiative* processes [92, 104, 105]. The non-radiative processes, characterized by the lake of photons emission, mainly consist in the relaxation from the excited state through vibrational transitions. These processes, typically occuring in a time scale of $10^{-11} \div 10^{-9}$ sec, can take place within the same electronic state or between different states (see Figure 2.4). In this latter case, the conversion from the singlet excited state S_1 to the vibrational excited triplet state T_1 is called *intersystem crossing.* On the contrary, the radiative processes are characterized by the emission of photons and the times of transitions are longer than those of the non-radiative processes. In particular, the so called *fluorescence*, attributed to the spin-allowed transition $S_1 \rightarrow S_0$, has times of the order $10^{-8} \div 10^{-4}$ sec and the *phosphorescence*, attributed to the spin-forbidden transition $T_1 \rightarrow S_0$, in times of the order $10^{-4} \div 10^{2}$ sec [92, 104, 105]. Because of different time involving, the non-radiative processes take place before the radiative ones, as shown in the several paths of the Figure 2.4; typically they bring the nuclear vibrational energy

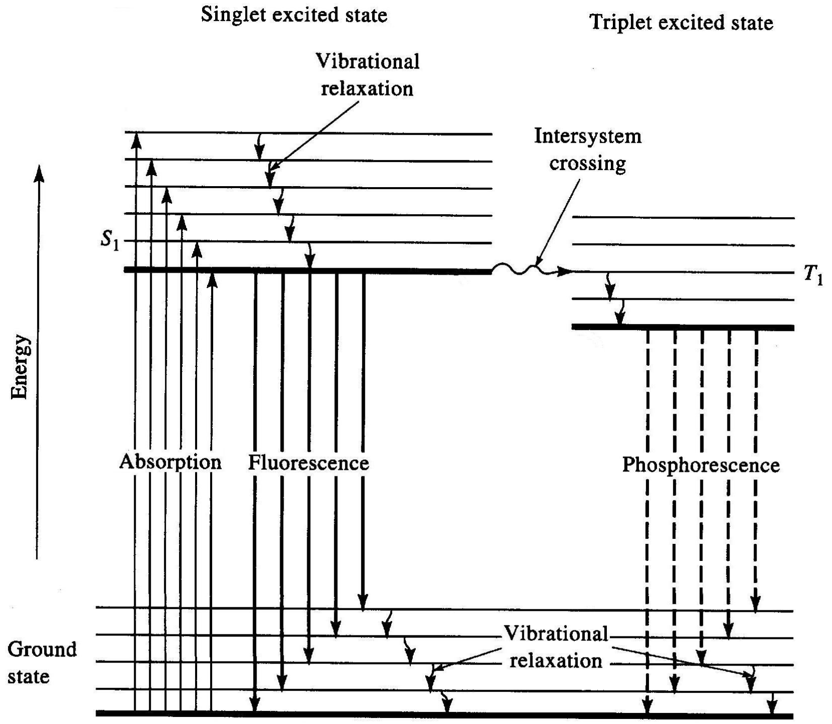

Figure 2.4: Jablonski energy levels diagram illustrating possible electronic processes following absorption of a photon. The non-radiative (intersystem crossing, internal and external conversion) and radiative processes (fluorescence and phosphorescence) are shown.

to its ground level before emission occurs.

From the Lambert-Beer's law reported in Equation 2.1, it can be easily obtained the relation:

$$I^{lum}(E_{exc}, E_{em}) = \Phi I_0(E_{exc}) \left[1 - e^{-\alpha(E_{exc})d}\right] \tag{2.39}$$

where $I^{lum}(E_{exc}, E_{em})$ is the emitted light intensity at energy E_{em}, when the system is exposed to the incident light $I_0(E_{exc})$ at the energy E_{exc}, and Φ is the *quantum yield*. Φ represents the ratio between the number of emitted and absorbed photons [92].

It is important to note that from Equation 2.39 two types of luminescence spectra can be defined: the *emission spectrum* (PL spectrum), in which the intensity is measured as a function of E_{em} for fixed E_{exc}, and the *excitation spectrum* (PLE spectrum), in which the intensity is measured as a function of E_{exc} for fixed E_{em}. In particular, the PLE spectrum represents the excitation efficiency of the luminescence spectrum. Equation 2.39 describes the stationary luminescence of a band when the investigated system is continually exposed to a constant excitation radiation. Time resolved luminescence can be explored using a pulsed excitation laser source, allowing to estimate the decay time τ of the luminescence bands. In the simple case of a two levels system, it can be shown that the time dependence of the luminescence is well described by the expression:

$$I^{lum}(E_{exc}, E_{em}, t) = I^{lum}(E_{exc}, E_{em}, t = 0)e^{-t/\tau}. \tag{2.40}$$

A more complex scenario occurs when inhomogeneities of emitting center environment affect its emission lifetime. In this case a superposition of decay processes with a distribution of τ is present. Experimentally this gives rise to a non single exponential decay. A typical expression describing this effect is the *stretched exponential decay law* [106, 107]:

$$I^{lum}(E_{exc}, E_{em}, t) = I^{lum}(E_{exc}, E_{em}, t = 0)e^{-(t/\tau)^{\gamma}}. \tag{2.41}$$

where $\gamma \leq 1$ is the stretching factor, which indicates the deviation from the single exponential decay. It is important to note that for $t = \tau$ the amplitude is reduced to 1/e of its initial value so that τ still gives an estimation of the process duration.

Chapter 3

Materials, treatments and experimental setups

In the present chapter the materials, the treatments and the instruments used to carry out the experiment investigations are discussed.

3.1 Materials

Two main types of silica materials were considered: fumed and bulk silica. The principal difference between these materials is that the former is constituted by an ensemble of silica particles with dimension falling into the nanometric scale, whereas the latter is constituted by "macroscopic" blocks having minimal dimensions of some hundred of microns.

3.1.1 Bulk silica

Bulk silica materials of different commercial origins and produced with standard industrial manufacturing, which assures a high reproducibility, were used. Commercial bulk silica is usually classified in four different types, distinguishing each other for the production method, silanol groups content, impurity content, etc. [51, 108]:

- **Natural dry (type I)**, produced by melting quartz powders in an inert atmosphere at low pressure using an electric arc. The Si-OH content of these materials is low, usually less than 30 ppm (parts per million by weight)[a]. The

---

[a] 1 ppm$\sim 7.7 \cdot 10^{16}$ Si-OH groups/cm^3 in silica

overall concentration of other extrinsic impurities, the most common being Ge, Al or alkali elements, is usually of the order of 10 ppm.

- **Natural wet (type II)**, produced by melting quartz powders in a H_2/O_2 flame. The Si-OH content is 150÷1000 ppm and concentration of other extrinsic impurities is lower than in the starting material (quartz powders) because some of them are partially dispersed in the flame.
- **Synthetic wet (type III)**, produced by hydrolysis of pure silicon compounds, usually $SiCl_4$, put in gaseous phase in a H_2/O_2 flame. The Si-OH content is higher than 100 ppm and the other impurity contents are negligible as the consequence of the high purity of the starting compounds.
- **Synthetic dry (type IV)**, produced by oxidation of $SiCl_4$ in a water free plasma. The Si-OH content is very low (<1ppm), but a high concentration of residual chlorine (usually higher than 100 ppm) is present.

Another manufacturing procedure to produce bulk silica materials, which does not belong to the above classification, is the so called *Vapor Axial Deposition* (VAD). This consists in the hydrolysis of $SiCl_4$ in a H_2/O_2 flame into the lower end of a rotating silica *boule*. This technique, mainly used to product silica fibers, leads to materials characterized by a very low Si-OH content (<1 ppm).

The full list of the bulk silica materials used in this Thesis, their nicknames, types, producers and OH contents are reported in Table 3.1. In this list, the SDC material does not fully belong to the classification above reported. Indeed, this material is obtained by electric fusion of purified sand; however, for its high content of silanol groups, we have classified this material as a type II-like. All samples have typical size $5 \times 5 \times 1$ mm^3 and were obtained cutting slabs of size $50 \times 5 \times 1$ mm^3. Only the Suprasil F300 samples have cylindric shape of diameter 6.5 mm and thickness 2 mm and were obtained cutting a cylinder of length $\sim$ 10 cm. The widest surfaces of all bulk silica samples here considered were optically polished.

3.1.2 Fumed silica

Fumed silica as well as other fumed oxides (Al_2O_3, TiO_2, etc.) are industrially produced in flame reactors. In the particular case of fumed silica, this is synthesized by a continuous flame hydrolysis technique, involving the conversion of silicon tetrachloride ($SiCl_4$) in the gas phase using an O_2/H_2 flame. $SiCl_4$ reacts spontaneously

Table 3.1: Bulk silica samples used in the experiments presented in this Thesis.

Bulk silica material (nickname)	Type	Producer	[OH] ppm (cm^{-3})
Infrasil 301 (I301)	I (natural dry)	Heraeus	7 ($5.4 \cdot 10^{17}$)
Puropsil A (QPA)	I (natural dry)	Quartz & Silice	15 ($1.2 \cdot 10^{18}$)
Silica EQ906 (Q906)	I (natural dry)	Quartz & Silice	20 ($1.5 \cdot 10^{18}$)
Silica EQ912 (Q912)	I (natural dry)	Quartz & Silice	20 ($1.5 \cdot 10^{18}$)
Herasil 1 (H1)	II (natural wet)	Heraeus	156 ($1.2 \cdot 10^{19}$)
Herasil 3 (H3)	II (natural wet)	Heraeus	156 ($1.2 \cdot 10^{19}$)
Homosil (HM)	II (natural wet)	Heraeus	156 ($1.2 \cdot 10^{19}$)
Silica/1060 (SDC)	II-like (synthetic wet)	Cerac	150 ($1.2 \cdot 10^{19}$)
Suprasil 1 (S1)	III (synthetic wet)	Heraeus	1000 ($7.7 \cdot 10^{19}$)
Suprasil 311 (S311)	III (synthetic wet)	Heraeus	195 ($1.5 \cdot 10^{19}$)
Corning 7940 (CNG5F)	III (synthetic wet)	Corning	900 ($6.9 \cdot 10^{19}$)
Suprasil 300 (S300)	IV (synthetic dry)	Heraeus	< 1 ($7.7 \cdot 10^{16}$)
Suprasil F300 (F300)	IV (synthetic dry)	Heraeus	5 ($3.8 \cdot 10^{17}$)
ED-C (EDC)	VAD	Tosoh Quartz	< 1 ($7.7 \cdot 10^{16}$)

with water, formed by flame itself, to yield silica and hydrochloric acid [109, 110]:

$$2H_2 + O_2 \longrightarrow 2H_2O \qquad 2H_2O + SiCl_4 \longrightarrow SiO_2 + 4HCl \tag{3.1}$$

Subsequently, a cooling line is used to release the heat produced by the reaction in flame and the HCl is separated from fumed silica (*deacidification*). A simplified scheme of these production phases is given in Figure 3.1 [109, 110].

This process generates almost spherical silica particles, known as *primary particles*, with diameter from few to tens nanometers, which tend to sinter together in aggregates of size 100÷500 nm. These aggregates adhere to each other to form agglomerates in a three dimensional chain-like structure of size from 10 to 200 μm [109–111]. By varying the reaction conditions (the concentration of the coreactants, flame temperature, etc.), the primary particles size, their specific surface area and some surface chemical properties can be modified, so to originate the different types of available fumed silica materials [109, 110]. The full list of the fumed silica materials used in this Thesis, their nicknames, their specific surface (measured by the

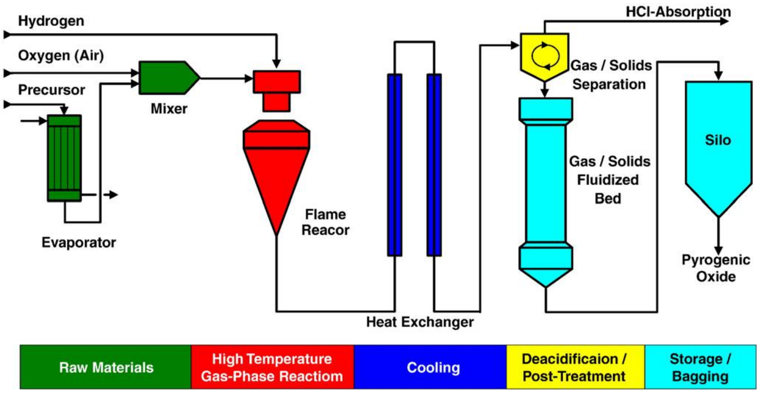

Figure 3.1: Simplified scheme of fumed silica production method [109, 110].

Table 3.2: Fumed silica materials used in the experiments presented in this Thesis.

Fumed silica type (nikname)	Specific surface (m^2/g)	Average primary particle diameter (nm)
Aerosil® 380 ($AE380$)	380±30	7
Aerosil® 300 ($AE300$)	300±30	7
Aerosil® 200 ($AE200$)	200±25	12
Aerosil® 150 ($AE150$)	150±15	14
Aerosil® 90 ($AE90$)	90±15	20
Aerosil® OX 50 ($AE50$)	50±15	40

physical absorption of N_2 (BET method)) and average primary particles diameter (estimated by the transmission electron microscopy (TEM) measurements) are reported in Table 3.2 [109, 110]. As a consequence of the nanometric primary particles sizes, fumed silica is characterized by a very high specific surface up to hundreds m^2/g (see Table 3.2) [109, 110]. This latter property is the main characteristic that distinguishes the different fumed silica types, which are declared 99.8 % by weight pure[b] and are produced in powder form consisting of about 98 % by volume of air with approximately 20 g/l densities.

The TEM images acquired for AE50 and AE380 are reported in Figure 3.2 [109, 110]. As evident the primary particles, characterized by an almost spherical shape,

---

[b] the most common impurities being Al_2O_3, Fe_2O_3, TiO_2 and HCl elements

form a loose network. By comparing these two images, it is possible to note that the tendency to form aggregates/agglomerates is more pronounced for smaller particles [109, 110, 112].

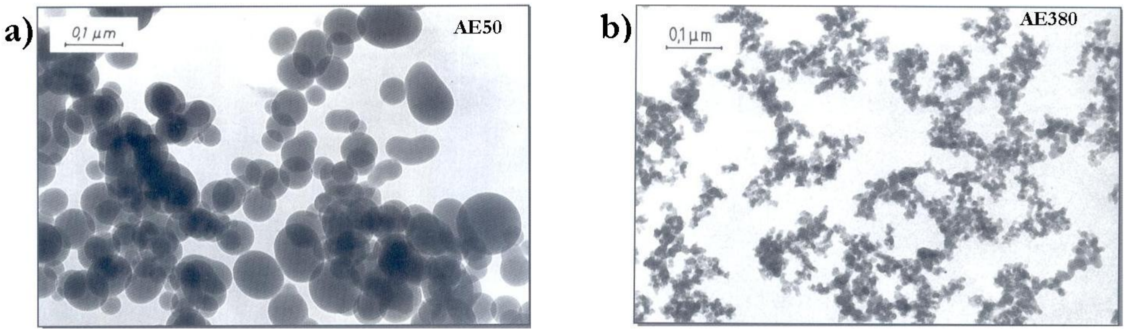

Figure 3.2: TEM images acquired for (a) AE50 and (b) AE380 powders. The different sizes of the primary particles and their different tendency to form aggregates/agglomerates are well evident.

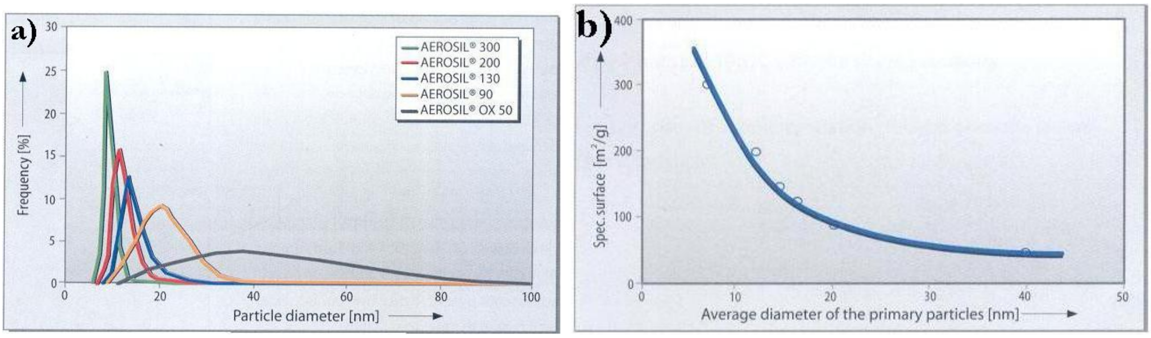

Figure 3.3: (a) Primary particle diameter distribution of some types of fumed silica materials. AE380 material is not shown because it has almost identical distribution curve of AE300 one. (b) The specific surface estimated by BET method as a function of the particle mean diameter estimated by TEM techniques for all of fumed silica types considered here apart from the AE380. The line indicates the 1/D trend.

The particle size distribution obtained by TEM measurements for each fumed silica type is shown in Figure 3.3(a). The distributions are characterized by a larger width on increasing the primary particle mean diameter. This is a typical property originating from the production method of nanoparticles [109, 110]. It is important noting that since the primary particles are almost spheroidal, a simple geometrical

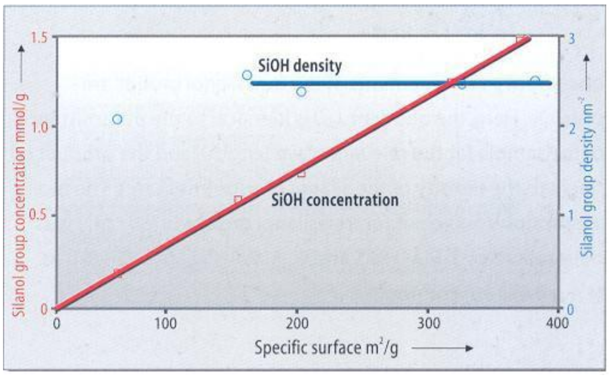

Figure 3.4: The concentration (left scale) and the density (right scale) of the surface silanol groups as a function of the specific surface area [109, 110]. Red and blue curves are guides for eye.

rule which links the specific surface area (S) to the particle mean diameter (D) exists: $D = \frac{6.0\times10^3}{S\rho}$, where D and S are expressed in nm and m^2/g, respectively, and ρ is the density in g/cm^3 units [113]. The density of primary particles is comparable in all fumed silica types (~2.2 g/cm^3), so that D and S are inversely related each other. This correlation is shown in Figure 3.3(b), where specific surface area (estimated by BET method) is reported as a function of the particle mean diameter (estimated by TEM techniques) for various fumed silica types. It is worth noting that the AE380 type is not reported in this figure because the above relation is not valid for this sample; indeed, it is characterized by the same particle mean diameter (D=7 nm) as the AE300 sample but it has a wider specific surface (see Table 3.2). This effect is attributed by the producers to the fact that the particles of the AE380 show a certain surface roughness, which increases their specific surface area as compared with that of the AE300 [109, 110].

The absolute concentration and the density per nm^2 of the surface silanol groups declared by the producer [109, 110], for each fumed silica type, are reported in Figure 3.4 as a function of specific surface area. A surface silanol group density of about 2.5 SiOH/nm^2 is attributed to all of the fumed silica types, independently of the specific surface area, apart from AE50 material. Indeed, this latter shows a density of about 2.2 SiOH/nm^2, which was ascribed to the higher flame temperature used during the production process, as compared with that of the other fumed silica types. As expected, the absolute concentration of the surface silanol groups linearly increases on increasing the specific surface area. All of the fumed silica types here considered have strong affinity for water and tend readily to absorb it from the room humidity. Water molecules tend to be fixed on the particle surfaces by hydrogen bonds with surface silanol groups. For this reason fumed silica is commonly indicated as a hydrophilic material.

Fumed silica sample preparations

The fumed silica samples, as said above, are produced in powder form. In order to obtain more easily-handleable samples and to substantially increase the amount of material (necessary for our experimental investigation), the as-received fumed silica powders were compacted in the form of self-supporting powder tablets by an uniaxial hydrostatic press working at ∼0.3 GPa[c]. These tablets of cylindric shape, with diameter and thickness about 4 cm and 1.8 mm, respectively, were successively cut in rectangular samples with typical size $5 \times 5 \times 1.8$ mm^3. The "apparent" density of samples (estimated roughly by mass to volume ratio, where the volume was measured by a vernier caliper) falls into the range 0.7÷1.0 g/cm^3 for all of the fumed silica types investigated. The snapshots of some of these samples (AE380, AE150 and AE50) are reported in Figure 3.5. It is important to note that the samples are characterized by a different transparency to the naked eye: the AE380 and AE150 samples appear semi-transparent whereas the AE50 one is white.

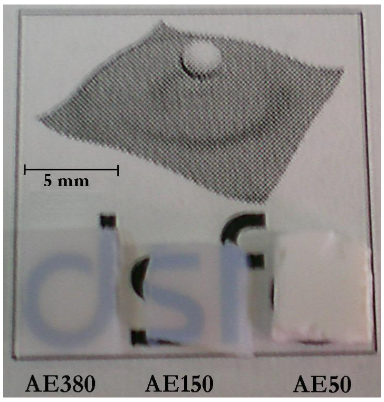

Figure 3.5: Photograph of typical AE380, AE150 and AE50 fumed silica samples after the compaction of powder by the uniaxial press. The visible transparency strongly depends on the fumed silica type.

---

[c] This procedure, as discussed in Chapter 5, does not modify the properties of the as-received system investigated.

3.2 Irradiations and thermal treatments

In this section, the ionizing radiations used to generate the point defects and the thermal treatments employed to modify the structural properties of the network and the point defect features are described. To induce point defects in bulk and fumed silica samples, different doses of irradiation with γ and β rays were used in this Thesis:

- bulk silica
  - γ-ray irradiations were carried out at room temperature by ^{60}Co source with dose rate of 1÷4 kGy/h and photon mean energy of ∼1.25 MeV (irradiation doses in the range 0.1÷100 kGy). *Nuclear Engineering Department of the University of Palermo, Italy.*
  - β-ray irradiations were carried out at room temperature by a pulsed RF S-band Linac with a dose rate of 120 Gy/s and electron mean energy of ∼3 MeV (irradiation dose at 90 kGy). *ENEA C.R., Frascati, Italy.*
- fumed silica
  - β-ray irradiations were carried out at room temperature by a linear accelerator with a dose rate of 120 Gy/s and electron mean energy of ∼6 MeV (irradiation dose at 400 kGy). *National Institute for Laser, Plasma and Radiation Physics, Magurele, Romania.*

Thermal treatments were performed in air in an electric furnace in the range 100÷1000 °C and for different time durations (from few minutes up to hundreds hours). The furnace temperature was controlled by a digital feedback circuit and was stabilized within ±3 °C. Both *isothermal treatments*, a sequence of thermal treatments at fixed temperature and of progressively increasing duration, and *isochronal treatments*, a sequence of thermal treatments at fixed duration and of progressively increasing temperature, were considered. In each thermal treatment, the sample was rapidly put in the furnace that was preliminarily heated at the given temperature. A temperature variation of the furnace from 5 °C to 20 °C (rapidly compensated within few minutes) was observed as the consequence of the insertion of the sample into the furnace. In particular, a variation of ∼5 °C was observed for low temperature (T<400-500 °C), whereas variations greater than ∼10 °C were detected for higher temperature. After each thermal treatment, the sample was rapidly removed from the hot furnace and was thermalized at room temperature.

3.3 Experimental setups

In this section a detailed description of the instruments used to investigate bulk and fumed silica materials is reported.

3.3.1 Raman measurements

Two different Raman spectrometers, equipped with near-IR and visible laser sources, were used. In general, the Raman signal intensity is related to the excitation wavelength by the relation: $\frac{1}{\lambda^4}$. From this point of view, in order to improve the signal to noise ratio, it should be better to use a spectrometer characterized by lower excitation wavelength. However, there are some typologies of materials for which a larger wavelength is preferred. This is the case of fumed silica, in which when a Raman spectrum with excitation wavelength in the visible range is acquired, a strong background signal is observed. This signal is not related to the vibration properties of the investigated system but it arises from a photoluminescence effect induced by visible excitation laser. This effect superimposes to the normal Raman scattering, making the analysis of the spectra very hard. As suggested by Uchino et al. [13, 44], this problem is overcome employing a near-IR laser source, which eliminates the effect of the background. For this reason, we employed a Raman spectrometer equipped with near-IR source to investigate the fumed silica materials. On the other hand, since these effects were not observed in the bulk silica materials, a Raman spectrometer employing a visible laser source was used for these latter materials.

Raman spectrometer with near-IR laser source

A Bruker RAMII Fourier Transform Raman spectrometer was used to acquire Raman spectra at room temperature with near-IR excitation. This instrument is equipped with a Nd:YAG laser source at 1064 nm(∼1.16 eV) working at the max power of 500 mW. A simplified scheme of this spectrometer is shown in Figure 3.6. The laser beam is focused on the sample, whose position is optimized to maximize the scattered light. Only the z-direction is motorized with 50 μm steps and maximum excursion of 1 cm. The scattered light from the sample is collected by a lens in back scattering geometry (the direction of laser beam and that of scattered light is the same) and is directed to a filter to cut the dominant Rayleigh elastic scattering at the same wavelength of the laser source. The filtered light reaches an interferometer, whose operating principle is shown in the same Figure 3.6: the light is separated in two beams by the beam splitter, one goes along the *path a* (green line) and the other goes along the *path b* (red line). These two beams are reflected by a fixed and a moving mirror, respectively, and then they superimpose at the beamsplitter on their way back from the mirrors and finally are directed to the detector (an InGaAs diode with an integrated preamplifier working at room temperature).

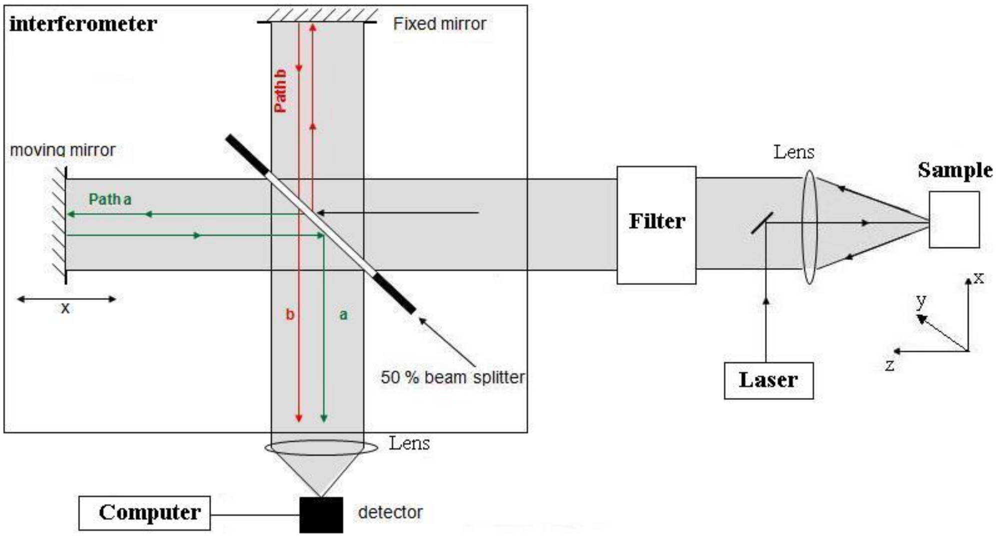

Figure 3.6: Schematic representation of Fourier transform Raman spectrometer.

The optical path length difference of the two beams depends on the position of the moving mirror, which moves back and forth in a continuous way: if its distance from the beam splitter is the same of that of the fixed mirror, the two beams have the same optical path and the signals are in phase, otherwise the two beams are out of phase. The detector measures the signal intensity $I(x)$ (usually called interferogram), due to the superposition of the two beams, at fixed wavelength as a function of the position x of the moving mirror that is as a function of the optical path difference:

$$I(x) = \int_0^\infty \frac{1}{2}\overline{I}\left(\overline{\nu}\right)\left[1 + cos(2\pi\overline{\nu}x)\right] d\overline{\nu} \tag{3.2}$$

where $\overline{I}\left(\overline{\nu}\right)$ is the incident spectral density on the interferometer at wavenumber $\overline{\nu} = 1/\lambda$. By making the Fourier transform of the Equation 3.2 and after few algebraical steps, the spectral density can be obtained:

$$\overline{I}\left(\overline{\nu}\right) = 2\int_{-\infty}^{+\infty}\left[2I(x) - I(0)\right]e^{-2i\pi\overline{\nu}x}dx \tag{3.3}$$

where $I(0)$ is the intensity measured at x=0 (when the signals are in phase).

The position x of the moving mirror is detected by a laser pointing system with high precision and the Fourier transform is performed by the instrument acquisition software. In order to focus on the Raman scattering without the Rayleigh contribution at the same frequency of the laser source, the Raman spectra are commonly reported showing the spectral density as a function of frequency shift with respect to the laser frequency. In particular, Raman instruments typically report the quantity $I\left(\overline{\nu}_L - \overline{\nu}\right)$, where $\overline{\nu}_L$ is the wavenumber of the laser source (in our case $\overline{\nu}_L = \frac{1}{1064nm} = 9398cm^{-1}$).

To prevent the effects of water vapour and CO_2 of air, which cause undesired absorption peaks typically in the middle-infrared spectral region, during measurements the chamber where the detector is allocated is purged with a continuous nitrogen flow (flux ~6 l/min). The Raman spectra reported in the following chapters were acquired at the maximum power of 500 mW and with a spectral resolution of 5 cm^{-1}. The working range is 70÷3500 cm^{-1} and the accuracy is 0.1 cm^{-1}. In order to improve the signal to noise ratio, many spectra were acquired and averaged. Each averaged spectrum took typically from few up to 20 h for sample.

Raman spectrometer with visible laser source

A Bruker SENTERRA dispersive micro Raman spectrometer was used to acquire Raman spectra at room temperature with visible excitation. A diode laser source at 532 nm (2.33 eV), working up to the max power of 20 mW, is installed in the instrument. This Raman spectrometer is equipped with an Olympus BX51 optical microscope and utilizes a hybrid aperture containing an array of pinholes and slits to set the *confocal* or *no-confocal* measurements, respectively. The confocal design provides high quality Raman spectra with the highest lateral and depth resolution at the diffraction limit. The principle of confocal optical microscopy is shown in Figure 3.7(a). In the case of a conventional optical microscope (left picture), the radiation is focused with the microscope objective to the desired region of a sample. The light scattered from two different depths of the sample are indicated as z_1 (red) and z_2 (blue). If both points are within the focused volume as defined by the objective field depth and system optics, the resulting spectrum will be an average of the spectra from the points z_1 and z_2. In the confocal mode (right picture), an aperture is placed in a remote image plane to reduce the sampling depth of field. In this simple example, the aperture blocks the Raman light scattered from z_2, thus resulting in a spectrum exclusively from z_1. Only the in-focus and on-axis Raman light rays are recorded by the spectrograph system, because the confocal aperture blocks the out-of-focus and off-axis light rays. The result is that the confocal optics and microscope restrict the sampling depth to a region that is smaller than that obtained using conventional optics. The confocal mode allows to carry out a depth profile of a sample acquiring successively spectra at the same position (in the xy plane) but in different sample layers (z height).

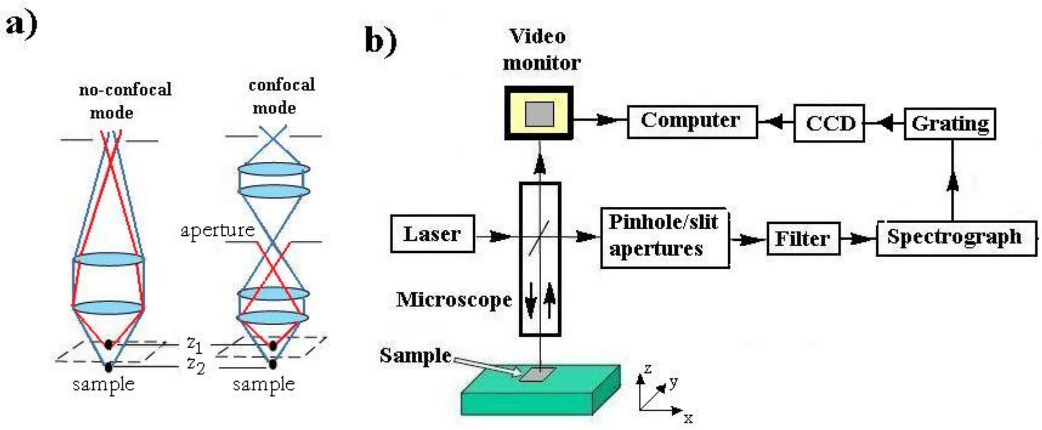

Figure 3.7: a) The principle of no-confocal (left) and confocal optical microscopy (right). b) the schematic representation of the micro Raman spectrometer.

A simplified scheme of the spectrometer used in this Thesis is reported in Figure 3.7(b). The laser beam is focused on the sample, whose position can be manually-controlled in x- and y-direction rotating the corresponding knobs with 100 μm steps in order to bring the sample area of interest in the light path, while the movement in the z-direction (height) is adjusted by turning the course/fine focus adjustment knobs with 0.1 μm steps to bring the sample in focus. A standard trinocular viewer allows to see sample on the computer monitor or through the binocular. The scattered light from the sample, in back scattering geometry, goes through the microscope objective, which focuses the light on the pinhole (confocal mode) or on the slit aperture (no-confocal mode). The light is directed to a filter to cut the dominant Rayleigh elastic scattering at the same wavelength of the laser source. The remaining light arrives to a grating that separates the Raman scattered light into individual wavelengths. The spatially dispersed radiation is directed to the charge coupled device (CCD), which is thermoelectrically cooled at T=-50 °C in order to enhance the sensibility.

The microscope is equipped with two objectives 20x and 50x. Different available apertures can be selected: pinhole apertures of 25 and 50 μm for confocal mode and slit apertures of 25×1000 μm and 50×1000 μm for no-confocal mode. The resolution depends on the grating chosen: 3÷5 cm^{-1} (high resolution) and 9÷15 cm^{-1} (low resolution). In this latter case, only one spectral range from 40 to 4000 cm^{-1}, covering the complete spectral range of the spectrometer, can be selected. In the case of high resolution three spectral ranges can be selected, which combined all together cover almost the entire spectral range up to 4000 cm^{-1}. In all the Raman spectra here reported the range 53÷1557 cm^{-1} was considered.

The parameters used in this Thesis to acquire the Raman spectra of bulk silica materials are: 20x objective, 50×1000 μm slit aperture, 3÷5 cm^{-1} resolution, 53÷1557 cm^{-1} range and 20 mW power. The integration time of CCD were conveniently chosen.

3.3.2 EPR measurements

In a typical EPR experiment, the investigated sample is subjected to two orthogonal external magnetic fields indicated hereafter as $\mathbf{H}$ and $\mathbf{H}_1$ [97–101]. The first is a static magnetic field, which splits the ground state energetic levels by Zeeman interaction: H_{zeeman}=$\mu_B\mathbf{H}\cdot\hat{g}\cdot\mathbf{S}$, where μ_B is the magnetic moment, $\hat{g}$ is electronic splitting factor and $\mathbf{S}$ is the effective spin. The second is a magnetic field oscillating at frequency ω, normal to $\mathbf{H}$ and with amplitude much smaller than the static magnetic field, which induces transitions between pairs of states split by the Zeeman interaction [97–101]. The transitions occur when the resonance condition is verified (see Section 2.2):

$$\hbar\omega = g \cdot \mu_B \cdot H \tag{3.4}$$

that is the energy of the photons associated to $\mathbf{H}_1$ is equal to the energy difference between the split levels. Since it is difficult to change and control with accuracy the frequency ω of the oscillating magnetic field, an EPR spectrum is usually acquired by measuring the microwave power absorbed by the sample as a function of the static magnetic field amplitude H, while the amplitude and frequency of the magnetic field $\mathbf{H}_1$ are fixed [97–101].

In our experimental investigation, a Bruker EMX-micro spectrometer working at ∼9.8 GHz (X band) was used. The block scheme of this spectrometer is shown in Figure 3.8, where it is possible to recognize the elements constituting the four main instrumental blocks: resonant cavity, magnetic generator, microwave bridge and acquisition system.

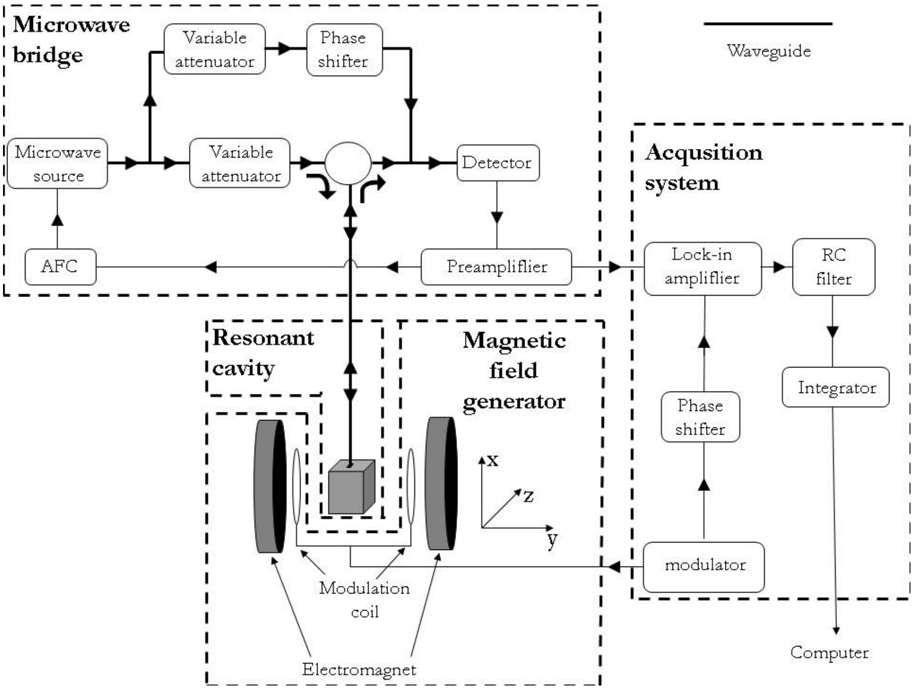

Figure 3.8: Schematic representation of the EPR spectrometer.

The resonance cavity is a metallic box with high conductivity internal walls. The cavity internal dimensions are comparable to the microwave wavelength. The sample to be investigated is located at the center of the cavity, resonating in the TE_{102} at about 9.8 GHz, where the microwave magnetic field is maximum and the microwave electric field is minimum.

In the microwave bridge, the oscillating magnetic field $\mathbf{H}_1$, or more simply microwave radiation, is generated by a Gunn diode working at the frequency of ∼9.8 GHz. During the measurement, this frequency is controlled and modified by the Automatic Frequency Control (AFC) in order to be locked to the frequency of the resonance cavity, filled by the sample under study. The power transmitted to the cavity through a waveguide can be attenuated with respect to the maximum power generated by the microwave source (200 mW) by the variable attenuator. The power incident on the cavity is then measured in decibel units of attenuation using the formula:

$$\text{Att(dB)} = -10 \cdot \log_{10} \frac{\text{power transmitted to the cavity}}{200mW} \tag{3.5}$$

In addition to the microwave radiation, the resonant cavity is exposed to the magnetic field **H**, generated by the electromagnet and varied during the measurement around the resonance value. A modulating magnetic field $\mathbf{H}_m$ is superimposed parallel to **H** through a couple of coils. This field oscillates at the frequency ω_m=2π100 kHz. The superposition of this modulation field to **H** is not necessary to obtain the resonance condition, rather it is used to enhance the sensitivity of the EPR spectrometer, through the lock-in detection system. Indeed, the radiation reflected from the cavity (radiation not absorbed by the sample), being amplitude modulated at the frequency ω_m, is converted by the detector (a Schottky diode) in a periodic current signal. Once this signal has reached the lock-in amplifier, the component related to the sample absorption is easily isolated from other spurious signals. For quantitative measurements as well as for optimal sensitivity, the incident microwave power on the detector should be higher than ∼1 mW. In order to fulfill this condition, some extra microwave power taken from the source and passing through the reference arm can be directed to the detector. To further enhance the signal-to-noise ratio, a RC circuit filter is traversed by the signal to cut off the noise components with frequencies higher than $\frac{1}{\tau_{cost}}$, where $\tau_{cost} = RC$ is the response time of the RC circuit. Finally, the signal reaches an integrator, which converts the current signal in a digital EPR signal.

Due to the use of modulated magnetic field and RC circuit filter, some conditions have to be satisfied in order to avoid EPR signal distortions [99, 100]:

$$H_m \leq 0.4\Delta H_{pp}, \tag{3.6}$$

$$\tau_{cost} \leq 0.1\frac{\Delta H_{pp}}{\Delta H_{sweep}}T_{sweep} \tag{3.7}$$

and

$$\tau_{cost} \leq 0.1\frac{H_m}{\Delta H_{sweep}}T_{sweep} \tag{3.8}$$

where ΔH_{pp}, ΔH_{sweep} and T_{sweep} are the peak-to-peak field distance, the interval of magnetic field scanned and the scan time, respectively.

As a consequence of the use of modulated magnetic field, generally the EPR spectra reproduce a curve proportional to the first derivative of the absorption lineshape when the non saturation and slow-passage conditions are satisfied (see Section 2.2.3). This type of acquisition, called hereafter *first-harmonic unsaturated mode* (FH-EPR) reveals the component of the signal reflected from the resonant cavity, oscillating at the same frequency and in phase with the modulating magnetic field [103, 114].

A more sensitive type of acquisition, called *second-harmonic saturated mode* (SH-EPR), can be achieved when the signal is saturated and the rapid-passage conditions is satisfied. This type of acquisition reveals the part of the signal oscillating at double the frequency ω_m and $\pi/2$-out-of-phase with respect to the modulation magnetic field [103, 114]. In this case the EPR spectrum reproduces a signal resembling the absorption curve[d]. It is import to remark that the features the FH-EPR signal can be easily derived from the analytic solution of the phenomenological Bloch equations reported in Section 2.2.3. This is not the case for SH-EPR signal, where a general analytical treatment is lacking and a more empirical experimental approach is used to correctly detect the SH-EPR signal and to maximize its intensity. In the present Thesis, in agreement with several previous works [77, 78, 115], the FH-EPR was used to detect the main resonance line of the E'$_\gamma$ center, whereas the SH-EPR was applied to reveal the strong hyperfine structure, whose intensity is very low. Furthermore, in the samples characterized by a FH-EPR signal intensity of the main resonance line of the E'$_\gamma$ center with very poor signal-to-noise ratio, the SH-EPR was used. This is the case of fumed silica which, as discussed in Section 1.3.3, is irradiation-resistant.

Usually, the concentration of the E'$_\gamma$ centers is estimated by the comparison of the double integral of the main resonance line acquired in FH-EPR with that of a reference sample with known E'$_\gamma$ center concentration. In the present Thesis, a γ rays irradiated bulk silica sample was used as reference and the concentration of the E'$_\gamma$ centers was determined by the spin echo technique [116]. However, when the concentration of E'$_\gamma$ centers was too low to be detectable by FH-EPR measurements, we estimated it by SH-EPR signal. These estimations were obtained by multiplying the integral of the SH-EPR spectrum by an empirical factor deduced by the ratio between the concentration of E'$_\gamma$ centers, estimated from FH-EPR measurements,

---

[d] provided that the paramagnetic centers are characterized by an inhomogenously broadened EPR line.

Table 3.3: The instrument parameters of the EPR spectrometer used in this Thesis.

	E'$_\gamma$ center main resonance line (FH-mode/SH-mode)	Strong hyperfine structure of the E'$_\gamma$ center (FH-mode/SH-mode)
ΔH_{sweep} (mT)	0.8/0.8	80/80
H_m (mT)	0.01/0.01	0.8/0.8
Power (mW)	$8 \times 10^{-4}/5$	$5 \times 10^{-2}/50$
Harmonic	I/II	I/II
phase	0/270	0/270

and the integral of the SH-EPR spectrum, determined in a sample where both the FH- and SH-EPR signals were detectable.

The instrument parameters that we used to acquire the EPR spectra must satisfy the conditions reported in the Equations 3.6, 3.7 and 3.8, besides they depend on the investigated signal (E'$_\gamma$ center main resonance line and its strong hyperfine structure) and type of acquisition (FH- and SH-EPR mode). In particular the instrument parameters used in this Thesis are reported in Table 3.3.

3.3.3 Infrared absorption measurements

The infrared absorption spectra reported in this Thesis were acquired by a Bruker Vertex 70 Fourier transform IR single-beam absorption spectrometer. A simplified scheme of this system is shown in Figure 3.9. The source is a globar (i.e. an U-shaped piece of silicon carbide) emitting a broad band in the middle-infrared range. The light emitted from the source is collimated and directed to the interferometer. This latter works exactly as the interferometer of the Raman spectrometer with near-IR laser source already described. The signal generated by the interferometer is focused into the sample chamber and then reaches the infrared DLaTGS detector, operating at room temperature and covering a spectral range from 400 to 6500 cm^{-1}. The detector measures the interferogram I(x), then by Fourier transform, performed by the instrument acquisition software, the interferogram is converted in the spectral density $\overline{I}\left(\overline{\nu}\right)$ (see Section 3.3.1). When the sample is located in the sample chamber the detector measures the interferogram of the signal transmitted from the sample

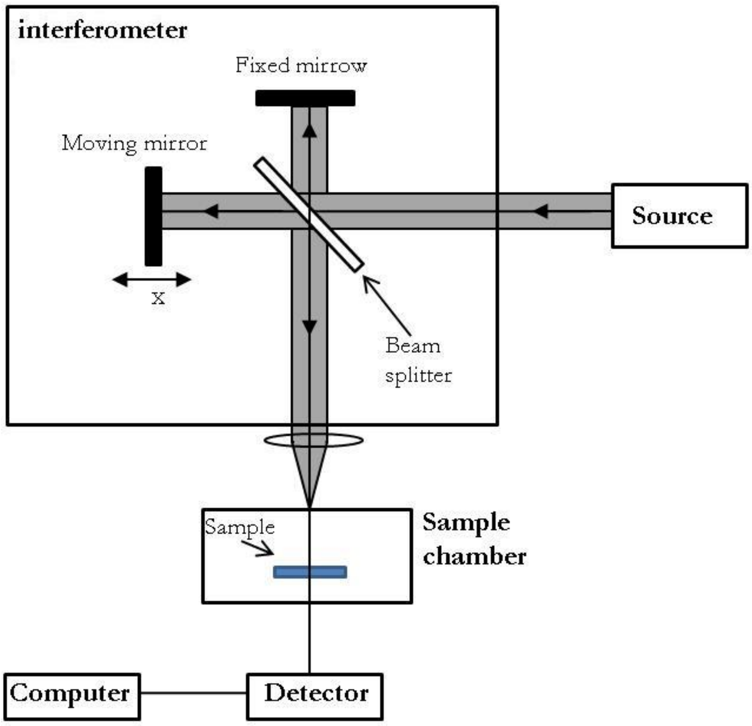

Figure 3.9: Schematic representation of the Fourier transform IR spectrometer.

$(\overline{I}_t(\overline{\nu}))$. Since the spectrometer considered in this Thesis is a single-beam, the spectral density of the sample chamber with no sample $(\overline{I}_0(\overline{\nu}))$ was acquired in order to obtain the absorption spectrum by the usual relation:

$$Abs(\overline{\nu}) = log_{10}\left(\frac{\overline{I}_0(\overline{\nu})}{\overline{I}_t(\overline{\nu})}\right) \tag{3.9}$$

To remove the undesired absorption peaks due to the water vapour and CO_2 of air, during measurements the whole spectrometer is purged with a continuous nitrogen flow of about 10 liters/min. Besides, after the sample was inserted or removed from the sample chamber, 20 min were waited before starting a measurement in order to reach the condition of nitrogen saturation of the sample chamber. All of the spectra reported here were acquired with a spectral resolution of 1 cm^{-1} and were averaged over 200 scans. The errors associated with the determination of the position and the amplitude of the IR bands of our interest are ± 0.05 cm^{-1} and less than 1%, respectively.

3.3.4 Other experimental setups

In addition to Raman, EPR and infrared absorption measurements two other experimental investigations were carried out to deepen the knowledge uncommon properties of fumed silica. These techniques are briefly described below.

Time resolved photoluminescence measurements

Time resolved photoluminescence spectroscopy consists in the acquisition of luminescence emission spectra at different delay times (T_D) from the excitation pulse integrated in different time windows (ΔT). Because measurements do not occur until a certain time has elapsed from the excitation pulse, this technique allows to estimate the decay time of a luminescence band and to distinguish between luminescence components characterized by different decay kinetics.

Time resolved PL spectra were performed at room temperature in a standard front-scattering geometry. Pulsed excitation light (pulse width ∼5 ns, repetition rate 10 Hz) was provided by a VIBRANT OPOTEK optical parametric oscillator laser system, pumped by the third harmonic (3.50 eV) of a Nd:YAG laser. Laser photon energy was varied from 2.25 to 5.90 eV; the beam intensity was monitored by a pyroelectric detector and was kept at ∼0.2 mJ/pulse. The luminescence emitted from the sample was dispersed by a spectrograph (SpectraPro 2300i, PI/Acton, 300 mm focal length) equipped with a grating with 150 grooves/mm, the spectral slit resolution was set to 20 nm. The detector uses an intensified CCD camera driven by a delay generator (PIMAX Princeton instruments) in order to synchronize the detector with the pulsed source.

Atomic force microscopy measurements

The atomic force microscopy (AFM) was used to qualitatively investigate the topography of fumed silica samples and its modification induced by thermal treatments. The AFM uses a microfabricated cantilever with a sharp tip that interacts with the surface of interest in order to investigate its topography. The cantilever raster-scans the sample while its deflection or oscillation amplitude is measured. These measurements are performed by an optical tracking system that uses a photodetector to track the reflection of a laser on the back of the cantilever. Detected changes in cantilever deflection or oscillation amplitude are recorded and correlated to a voltage-distance calibration factor in order to determine the height z at a given xy coordinate.

In this Thesis tapping mode amplitude modulation AFM measurements [117–119] were performed by a *Multimode V* (Veeco Metrology) scanning probe microscope. It is equipped with a conventional piezo-scanner (maximum xy range $\sim$ 14 μm, maximum z range $\sim$ 3.6 μm) and a four-segment photodetector for cantilever deflection monitoring. Point Probe® Plus Silicon-SPM-probes were used with Al backside reflex coating, resonance frequency ~300 kHz and tip apical diameter ~10 nm. All the scans were performed at room temperature and in nitrogen atmosphere. The inert gas ambient, obtained by continuous purging the sample chamber with nitrogen (flux~2 l/min), was necessary to reduce the probability of adhesion of the nanoparticles to the tip, by efficiently reducing the capillary forces acting between them. Prior to AFM measurements, all of the samples in powder tablet form were subjected to a meticulous cleaning procedure, which consists in a sequence of three ultrasonic treatments in ethanol, acetone and distilled water. Each single treatment had a duration of about 20 min. After cleaning, the samples were dried by placing them directly into the AFM sample chamber and by purging with nitrogen (flux~5 l/min) for about 10 h before measurements. All the acquired images had a resolution of 512 x 512 pixels and were obtained with a tip velocity on the surface of $\sim$ 2 μm/s.

Chapter 4

Results: investigation of the structural properties and their modifications in bulk silica

In the present chapter the investigation by Raman and EPR spectroscopy on a wide variety of bulk silica materials of commercial origin differing, in production methods and impurities content (see the Table 3.1), is reported. We devoted the attention on the as-grown structural properties of the different materials (Section 4.1) [120] as well as on their modifications induced by isothermal treatments (Section 4.2) [121]. In particular, we investigated the features of the D_1 and D_2 Raman lines, probing the mean features of the network (range-III order), and of the strong hyperfine structure of the E'$_\gamma$ center, probing the local arrangement of the network (range-II order). All of the considered materials were opportunely γ- or β-ray irradiated at the maximum dose of 10^2 kGy in order to induce a detectable concentration of the E'$_\gamma$ centers.

4.1 Structural properties of different bulk silica materials

In a first set of experimental, to investigate the as-grown general properties of silica structure, we acquired Raman spectra for all the materials reported in Table 3.1 both before and after γ-ray irradiations in the dose range $0.1 \div 10^2$ kGy. In Figure 4.1

we report the Raman spectra, normalized to the signal amplitude of the main broad line peaked at ∼440 cm^{-1}, acquired for F300, Q906 and S1 not irradiated materials.

As shown in Figure 4.1 the Raman lines peaked at about 800, 1065 and 1200 cm^{-1} (assigned to $Si-\widehat{O}-Si$ bond-stretching vibrations [15, 23]) are well superposed in the different materials, whereas the D_1 and D_2 lines possess different amplitudes and a small variability can be observed in the shoulder of the main line peaked at ∼440 cm^{-1} too. In order to quantitatively estimate these difference we determined the amplitude of the D_1 and D_2 lines for each material. To this aim, in agreement with the method of analysis used in a previous experimental investigation [122], we subtracted to each normalized spectrum an opportune baseline, as indicated by the dashed lines in the insets of Figure 4.1 insets for S1 material. In Table 4.1 we report the obtained values for the relative amplitude of the D_2 line. The choice to consider the amplitude of the D_2 line, and not that of the D_1 one, followed the ascertainment that the former is significantly less affected by the details of the baseline used to estimate its amplitude from the Raman spectrum. We observed that there is no explicit correlation of the D_2 line amplitude with the material type and a variability larger than the experimental errors occurs. After irradiation, no detectable modifications on the intrinsic Raman lines were evidenced in the range of investigated doses[a].

In all of the considered materials, no EPR signals were detected before irradiation. At variance, in the irradiated materials the characteristic main FH-EPR line due to the E'$_\gamma$ center was revealed. In Figure 4.2 the FH-EPR spectra acquired for the materials F300, Q906 and S1, irradiated at $\sim 10^2$ kGy, are shown. The spectra, normalized to the peak-to-peak signal amplitude, evidence that the main resonance line of the E'$_\gamma$ center has a L2 line shape, as discussed in Section 1.3.3, in all of the three materials. Indeed, we estimated that $\Delta g_{1,2}$ ∼0.0017. Similar findings were found in all the other irradiated materials (not reported here).

As discussed in Section 1.3.3, it was reported that the strong hyperfine structure of the E'$_\gamma$ center is particularly sensitive to the defect environment. In order to study this hyperfine structure, we performed EPR measurements over an extended range of magnetic field (∼80 mT). Since this structure is characterized by a very low intensity, in order to obtain EPR spectra with a suitable signal-to-noise ratio we took advantage of the high sensitivity of the SH-EPR acquisition method. In addition, in the samples in which the intensity of the strong hyperfine structure was high enough,

---

[a] It is worth noting that in few samples after irradiation at high doses ($\sim 10^2$ kGy), a wide bands due to defect-related spurious photoluminescence appears.

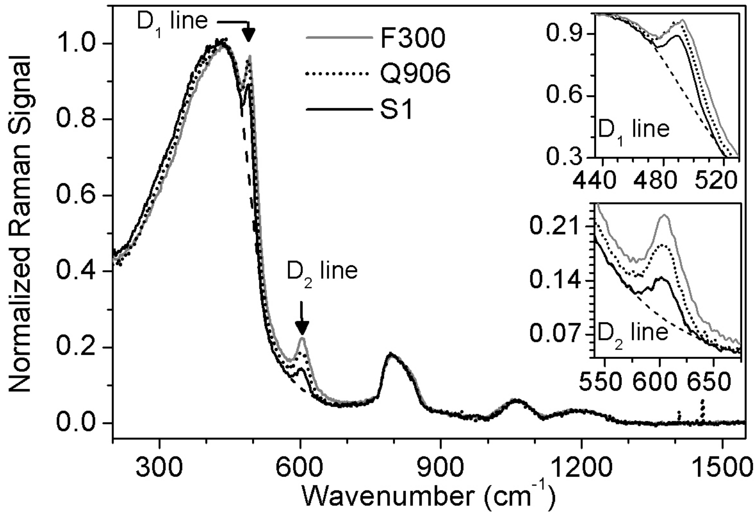

Figure 4.1: Raman spectra detected for F300, Q906 and S1 materials, normalized to the amplitude of the main line peaked at about 440 cm^{-1}. Dashed lines below the D_1 and D_2 lines are the baselines used to estimate the amplitude of these lines for the S1 spectrum. Insets: zooms of the D_1 and D_2 lines.

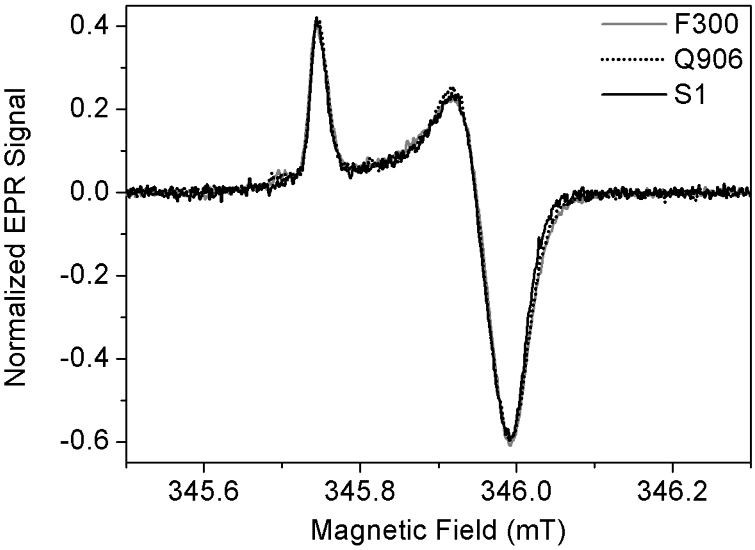

Figure 4.2: FH-EPR spectra of the E'$_\gamma$ center main resonance line acquired for F300, Q906 and S1 materials, irradiated at $\sim 10^2$ kGy, normalized to the peak-to-peak signal amplitude.

Table 4.1: Relative amplitude of the D_2 line, estimated from the Raman spectra normalized to the R-line, and splitting of the E'_γ center strong hyperfine structure in each bulk silica material considered.

Bulk silica materials (type)	D_2 line amplitude	Splitting of the E'_γ center hyperfine structure (mT)
I301 (I)	0.081±0.004	41.80±0.08
QPA (I)	0.082±0.004	41.80±0.08
Q906 (I)	0.086±0.004	42.04±0.08
Q912 (I)	0.08±0.004	41.80±0.08
H1 (II)	0.067±0.004	41.88±0.08
H3 (II)	0.082±0.004	41.88±0.08
HM (II)	0.067±0.004	41.80±0.08
SDC (II-like)	0.1059±0.004	42.52±0.08
S1 (III)	0.051±0.004	41.80±0.08
S311 (III)	0.055±0.004	41.88±0.08
CNG5F (III)	0.060±0.004	41.80±0.08
S300 (IV)	0.061±0.004	41.80±0.08
F300 (IV)	0.106±0.004	42.44±0.08
EDC (VAD)	0.081±0.004	42.04±0.08

the results obtained by SH-EPR measurements were corroborated by the FH-EPR ones. In agreement with previous experimental investigations [123], we found that no change of the strong hyperfine splitting occurs in each material as a function of the irradiation dose, in the range considered. For this reason, in the following no reference will be made to the dose at which the various materials were irradiated.

In Figure 4.3 we report a comparison of the SH-EPR spectra obtained for the strong hyperfine structure of the E'_γ center in the same materials of Figures 4.2 and 4.1. The spectra show the saturated EPR central line of the E'_γ center (out of scale in the figure), a pair of lines split by about 42 mT, which represents the hyperfine structure of the E'_γ center, and other signals due to hydrogen related point defects distinguishable from that of the E'_γ center [124]. These spectra evidence that the splitting of strong hyperfine structure depends on the material. In order to make the changes in the peak-to-peak separation of the strong hyperfine doublets more

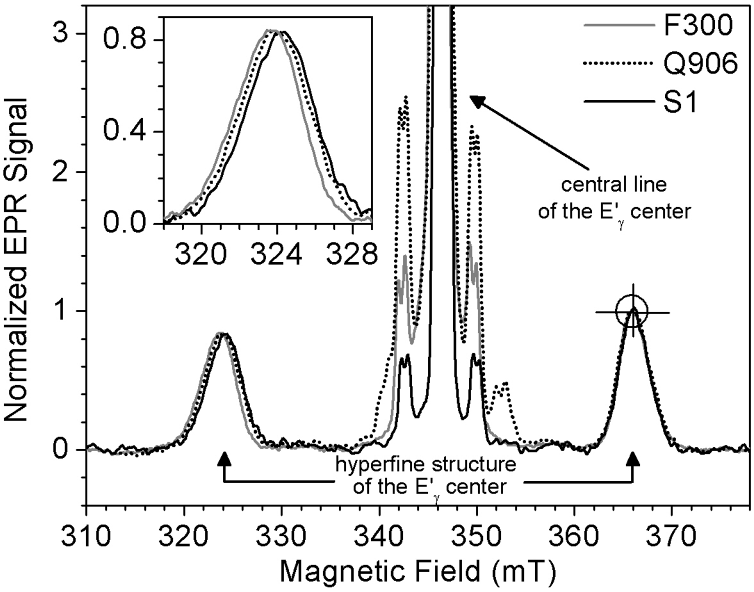

Figure 4.3: SH-EPR spectra acquired for F300, Q906 and S1 materials irradiated at ~10^2 kGy. Inset: zoom of the low field component of the strong hyperfine doublets.

evident, each spectrum in Figure 4.3 was normalized and horizontally shifted in order to superimpose the high-field components, centered at about 366 mT. In Table 4.1, the splitting of the strong hyperfine structure of the E'$_\gamma$ center, estimated for all the set of considered materials, is reported.

4.1.1 Discussion

Our experimental data allowed us to point out that both the strong hyperfine structure of the E'$_\gamma$ center and the Raman spectra of the investigated materials show a material-to-material measurable variability. Furthermore, we observed that these two properties are not affected by the irradiation up to the maximum dose we considered (~10^2 kGy). Since it is known that Raman and EPR features are affected by the structure of the matrix, we guessed a possible relation between them.

In order to make a quantitative comparison between the features of the E'$_\gamma$ center strong hyperfine structure and those of the Raman spectra, in Figure 4.4 we report the strong hyperfine splitting of the E'$_\gamma$ center as a function of the D_2 line relative amplitude for all the materials considered (see Table 4.1). The data reported in Figure 4.4 evidence that the strong hyperfine splitting of the E'$_\gamma$ center and the D_2

Raman line amplitude are correlated, as qualitatively indicated by the dashed line.

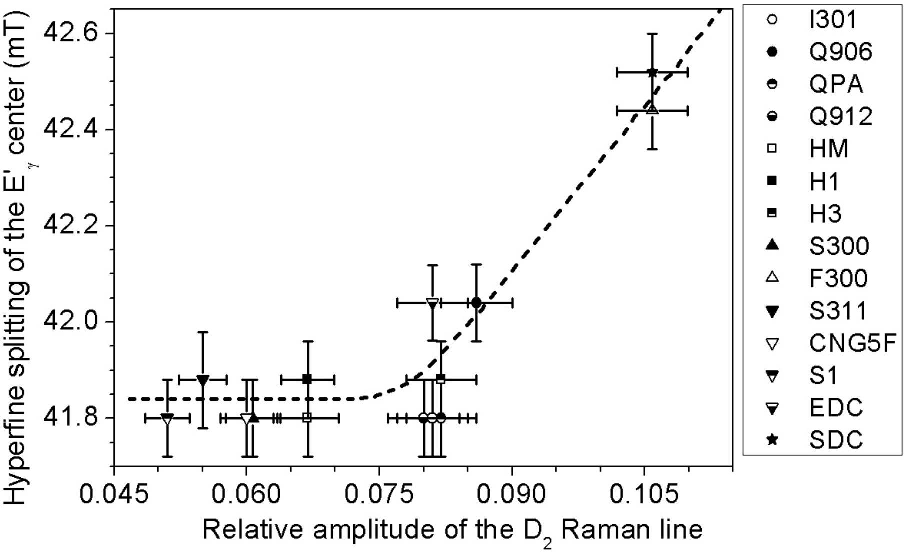

Figure 4.4: Peak-to-peak separation of the E'$_\gamma$ center strong hyperfine doublet as a function of the D_2 line amplitude estimated from the normalized Raman spectra. Dashed line is drawn as guide for the eye.

As discussed in Section 1.1, the D_2 line amplitude is directly related to the population of the 3-membered rings [15, 18, 20], probing of the range-III order properties of silica network, whereas the strong hyperfine splitting of the E'$_\gamma$ center depends strongly on the $Si - \widehat{O} - Si$ and $O - \widehat{Si} - O$ bond-angles and Si-O bond-lengths [77, 80], due to the range-II order properties (see Section 1.3.3). Consequently, our findings suggest that the range-II and -III order are intimately related each together. More precisely, our data indicate that when the amplitude of the D_2 Raman line is less than ∼8% with respect to the amplitude of the main line, peaked at ∼440 cm^{-1}, the strong hyperfine splitting is almost insensitive to D_2 line amplitude changes and is 41.8 mT. At variance, for relative amplitudes of the D_2 Raman line larger than ∼8% the strong hyperfine splitting increases monotonically on increasing the D_2 line amplitude. Finally, the comparison of the data of Figure 4.4 with the values of the OH groups content estimated for the various materials (see Table 3.1) put forward that no evident correlation exists between the strong hyperfine splitting of the E'$_\gamma$ center, or the amplitude of the D_2 Raman line, and the OH groups content of the materials. A relevant aspect in the context is the supposed ability of OH groups in affecting the relaxation properties of the silica network [125, 126].

4.2 Modifications induced by thermal treatment in the structural properties of a bulk silica material

Driven by the results reported in the previous section and in order to deepen the relation between the properties of the range-II and -III order of the silica network, we gradually modified the structural properties of a given material by isothermal treatments and probed the D_1 and D_2 Raman lines and the strong hyperfine structure of the E'_γ center. In particular, we chose to consider the material SDC among all of the materials considered above, because it is characterized by a wide strong hyperfine splitting of the E'_γ center and by intense amplitudes of the D_1 and D_2 Raman lines (see Figure 4.4). Basing on literature data [108], this commercial material should have an annealing temperature in the range 1080÷1200 °C; so by thermal treatments at 1000 °C, T_f should be gradually changed affecting the structural properties of the matrix [22].

In more details, we considered ten SDC samples: one of these was preserved by any thermal treatment, whereas nine samples were isothermally treated at 1000 °C for 5, 15, 30, 50, 80, 110, 180, 240 and 480 minutes, respectively. They will be indicated henceforth as *SDC/k*, where *k* indicates the treatment time duration in minutes. All these samples were β-ray irradiated at the dose of 90 kGy as discussed in Section 3.2.

We acquired Raman spectra for all the SDC/k samples before and after β-ray irradiation. Following Section 4.1, we verified that the irradiation does not modify the intrinsic Raman lines in the range of the investigated energies. In order to show the effect of the isothermal treatments, in Figure 4.5 the Raman spectra acquired for the samples SDC/0, SDC/80 and SDC/480, normalized to the amplitude of the main line (peaked at about 440 cm^{-1}), are reported. As pointed out in the insets of this figure, the thermal treatment gradually reduces the amplitude of D_1 and D_2 lines, while no detectable changes are evidenced in the other Raman lines, peaked at 880, 1065 and 1200 cm^{-1}. The Raman spectra (not reported here) acquired for the other samples thermally treated for different duration times confirm the trend observed in SDC samples. In order to quantitatively estimate the amplitude of the D_1 and D_2 lines for each material, in agreement with the method of analysis above used, we subtracted to the normalized spectrum an opportune baseline (see the grey dotted lines in the insets of Figure 4.5).

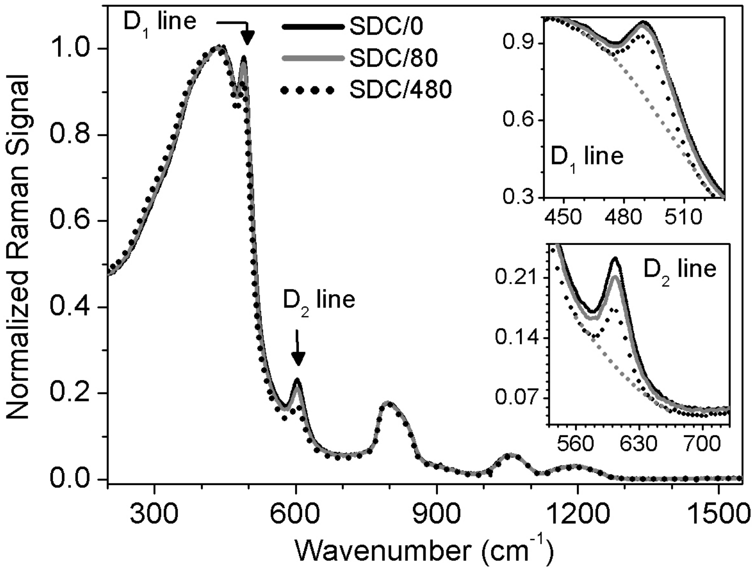

Figure 4.5: Raman spectra acquired for the samples SDC/0, SDC/80 and SDC/480, normalized to the amplitude of the main line peaked at ~440 cm^{-1}. Insets: zooms of the D$_1$ and D$_2$ lines. The grey dotted lines below the D$_1$ and D$_2$ lines are examples of typical baselines used to estimate the amplitude of these Raman lines.

No EPR signals were detected before irradiation in all of the samples considered. At variance, in the irradiated samples the characteristic EPR signal due to the central line of the E'$_\gamma$ center was detected. In Figure 4.6 the FH-EPR spectra acquired for the samples SDC/0, SDC/80 and SDC/480 (the same samples of Figure 4.5) and normalized to the peak-to-peak signal amplitude are shown. The line shape of the E'$_\gamma$ center is not exactly the same for all the samples; indeed just a small change of the line shape from L2 towards a more orthorhombic line shape is induced by the thermal treatment (compare the SDC/0 and SDC/480 spectra of Figure 4.6).

In Figure 4.7, the SH-EPR spectra of the strong hyperfine structure of the E'$_\gamma$ center, acquired for the same samples SDC/0, SDC/80 and SDC/480, are compared. In order to make the differences in the strong hyperfine splitting more evident, the same procedure of normalization and shift before described for Figure 4.3 was used. As shown in the inset of Figure 4.7, the thermal treatment affects the strong hyperfine splitting of the E'$_\gamma$ center, which is gradually reduced on increasing the time duration of the treatment. In Figure 4.8, the strong hyperfine splitting of the E'$_\gamma$ center (left scale) and the relative amplitude of the D$_2$ Raman line (right scale) as a function of the time duration of the thermal treatment for all SDC samples are reported. In

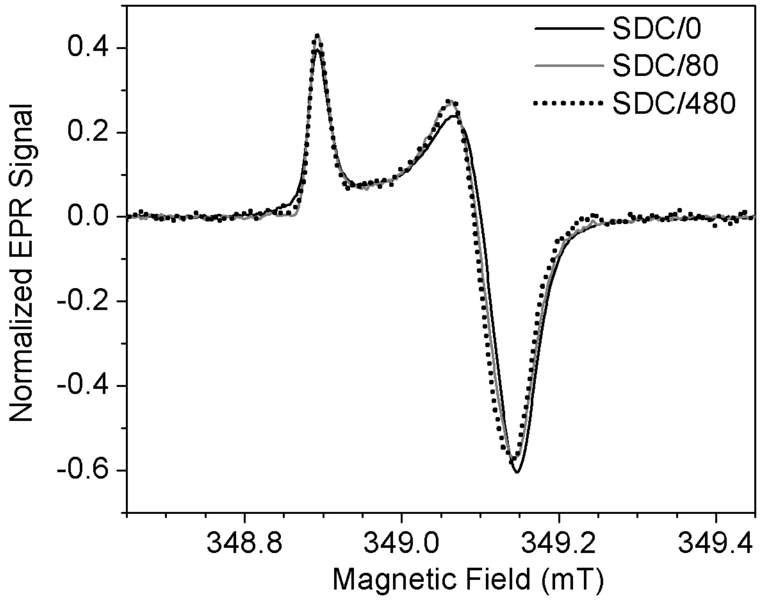

Figure 4.6: FH-EPR spectra of the E'$_\gamma$ center main resonance line acquired for SDC/0, SDC/80 and SDC/480 and normalized to the peak-to-peak signal amplitude.

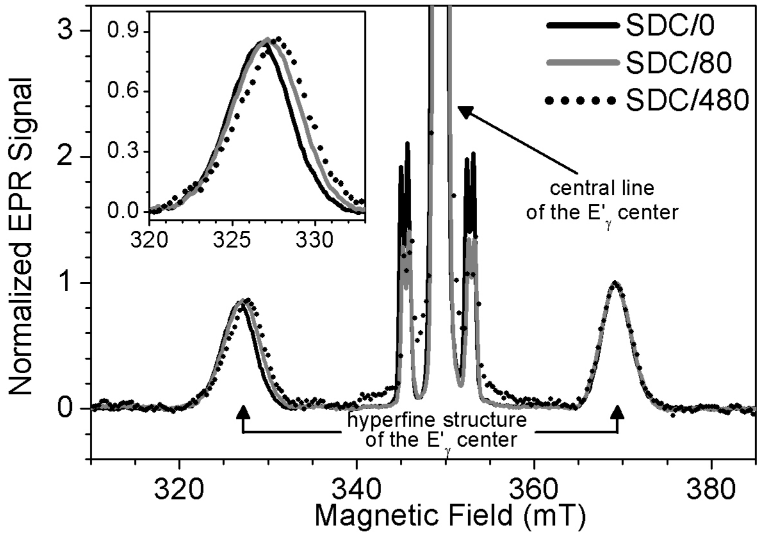

Figure 4.7: SH-EPR spectra acquired for the samples SDC/0, SDC/80 and SDC/480. Inset: zoom of the low field component of the strong hyperfine doublet.

this figure it is clear that the effect of the thermal treatment is to induce a gradual reduction of the D_2 line amplitude and of the strong hyperfine splitting on increasing

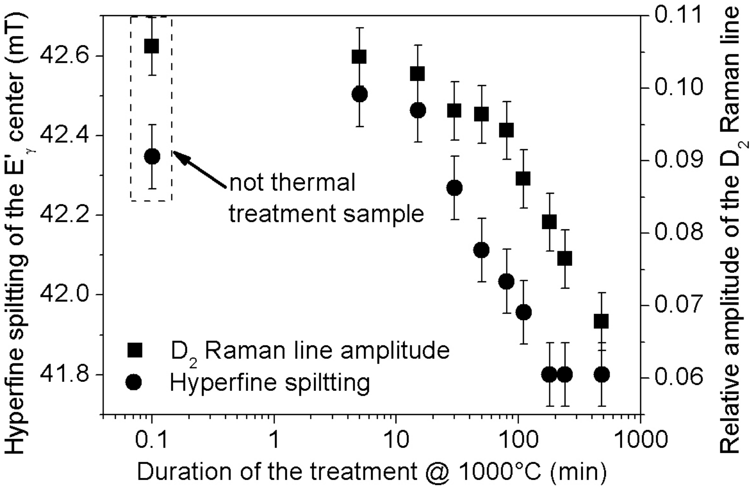

Figure 4.8: Splitting of the E'$_\gamma$ center strong hyperfine structure (left scale) and the relative amplitude of the D$_2$ Raman line (right scale) as a function of the time duration of the isothermal treatment at T=1000 °C. The untreated sample SDC/0 is indicated by the arrow.

the treatment time duration.

4.2.1 Discussion

Our experimental results show that the range-II and range-III order properties can both be modified by an opportune thermal treatment. Indeed, as shown in Figure 4.8, the amplitude of the D$_2$ Raman line and the splitting of the strong hyperfine structure of the E'$_\gamma$ center, probing the properties of the range-III and range-II order respectively, can be gradually modified by isothermal treatments at 1000 °C.

In order to investigate in a quantitative way the modifications on the range-II and range-III order properties and their relation, in Figure 4.9 we report the strong hyperfine splitting of the E'$_\gamma$ center as a function of the D$_2$ line amplitude, for the various SDC samples thermally treated for different duration times (black symbols). From Figure 4.9, it is visible that changes in the D$_2$ line amplitude up to 8 % occur without changes of the strong hyperfine splitting, whereas for larger changes in the D$_2$ line a concurrent change of the strong hyperfine splitting occurs.

The data reported in Figure 4.9 highlight a strong correlation between the strong hyperfine splitting and the amplitude of the D$_2$ line, further supporting the conclusion that the range-II and range-III order properties are intimately related to each other.

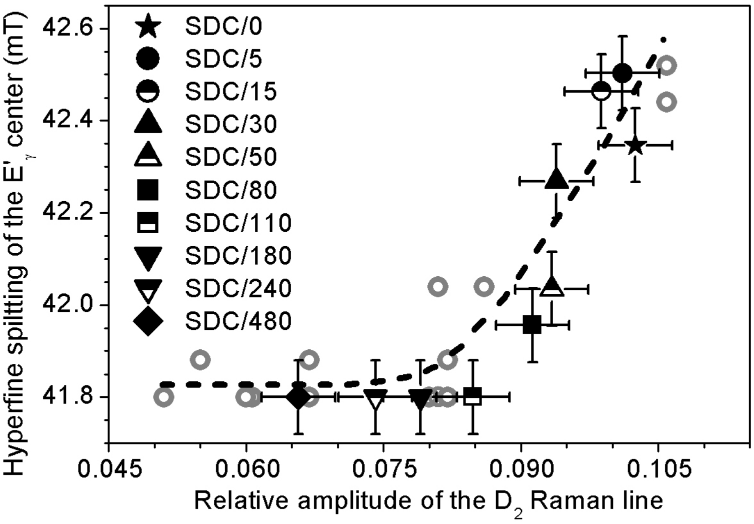

Figure 4.9: Peak to peak separation of the E'$_\gamma$ center strong hyperfine doublet as a function of the D_2 amplitude, estimated from the normalized Raman spectra, in the not thermally treated SDC sample ($\star$) and in 9 SDC samples thermally treated at 1000 °C for different time durations. Treatment time duration, expressed in minutes, is indicated as part of the nickname for each sample in the legend. Grey open circles are the experimental data above reported in Figure 4.4 [120], in which a set of materials of different commercial origin was considered. The dashed line is drawn as guide for the eye.

Besides, this correlation is in good agreement with the experimental data already reported in Section 4.1 [120], in which a similar trend was found for a set of not thermally treated materials of different commercial origin (see the grey open circles reported in Figure 4.9, corresponding to the data of the Figure 4.4).

Our findings point out that the different structural features in the range-II and range-III order, characterizing silica materials of different commercial origin (see the grey symbols), are essentially related to the different thermal history of the materials. In fact, all the possible values of the E'$_\gamma$ strong hyperfine splitting and those of the D_2 line amplitude can be obtained with a single material (SDC) by thermal treatment (see the overlap of the black and grey symbols in Figure 4.9). In other words, our results suggest that the variety of the configurations of the $Si-\widehat{O}-Si$ and $O-\widehat{Si}-O$ bond-angles and Si-O bond-lengths and of the ring size distribution are not due to the material type (natural or synthetic) nor to the impurity content of each material, but rather these structural features are mainly related to the thermodynamic properties of the system.

From this point of view, it is worth noting that the modifications of the thermodynamic properties affect the range-II and range-III order features in different ways. Indeed, as shown in Figure 4.9, the thermal treatments up to 110 minutes gradually reduce the strong hyperfine splitting of the SDC material, from 42.4 to 41.8 mT; whereas for longer treatment time the strong hyperfine splitting is not modified and it remains fixed at 41.8 mT. On the other hand, the D_2 line amplitude is gradually reduced on increasing the time duration for all the thermal treatments here considered. This suggests that initially the system modifies the whole structure by changing both the range-II and range-III order properties, but for subsequent modifications the system can change only the features of the range-III order.

Chapter 5

Results: investigation of the structural properties of fumed silica and their modifications by thermal treatments

In this Chapter we present the results on the investigation on six different types of fumed silica (see the Table 3.2) by Raman, EPR, IR absorption, luminescence spectroscopies and AFM. In particular, we devoted the attention on the spectroscopic features of the fumed silica that allow to obtain structural information and help to shed light on the origin of the uncommon properties of these materials as compared to bulk silica. In particular, in Section 5.1, the changes induced by isochronal thermal treatments on structural properties are investigated by the Raman and IR spectroscopies [127]. The enhancement of a blue luminescence band by thermal treatments is studied and related with the structural properties of the fumed silica particles in Section 5.2 [128, 129]. Finally, the generation of the E'_γ center by β-ray irradiation is considered in Section 5.3.

Before to report and discuss the results we obtained, it is useful to show the preliminary investigation that we carried out on the fumed silica materials. As discussed in Section 3.1.2, as-received fumed silica is in powder form, consisting of about 98 % by volume of air. As a consequence of the low apparent density of the samples (approximately 2×10^{-2} g/cm^3), their signal amplitude in the Raman as well as that in the EPR and luminescence spectra is very low. In order to increase the density of the samples and therefore their signals, as-received powders were compacted in tablets of density ~0.7÷1 g/cm^3 by an uniaxial hydrostatic press working at ~0.3 GPa. This pressure value was opportunely chosen considering that, from one hand, it is high enough to ensure a substantial increase of the density (about 50 times) and from other hand, it is small enough to not induce permanent structural modifications. Indeed, the anelastic regime occurs in the pressure range from 4 to 8 GPa (see the last part of Section 1.2) [47]. However, to show that our procedure does not alter the structural properties of the fumed silica samples, the comparison of the Raman spectra acquired for the AE380 as-received powders and for the same powders compacted in tablets has been done; the results are shown in Figure 5.1.

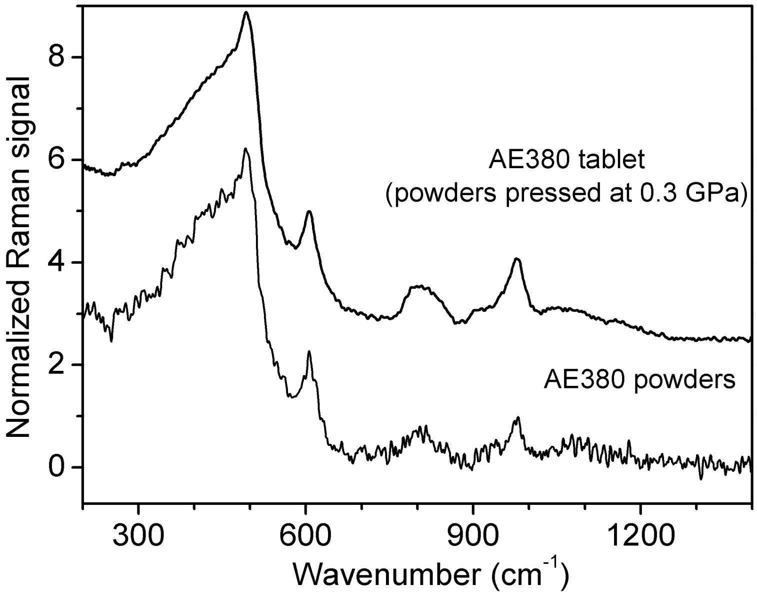

Figure 5.1: Raman spectra acquired for the AE380 as-received powders and for the same powders compacted in tablets by an uniaxial hydrostatic press working at ~0.3 GPa. The spectra are arbitrarily vertically shifted after the normalization described in the text.

The spectra of Figure 5.1 were normalized to the amplitude of the line peaked at ~800 cm^{-1}. We chose to normalize to this line all of the Raman spectra of the fumed silica, rather than to normalize to the R-line as we did for bulk silica materials in the previous Chapter[a], because the line peaked at ~800 cm^{-1} is much more stable

---

[a] It is important to note that in the case of the bulk silica materials previously considered, to normalize to the line peaked at ~800 cm^{-1} or to the R-line gives indistinguishable results, as evident from Figures 4.1 and 4.5

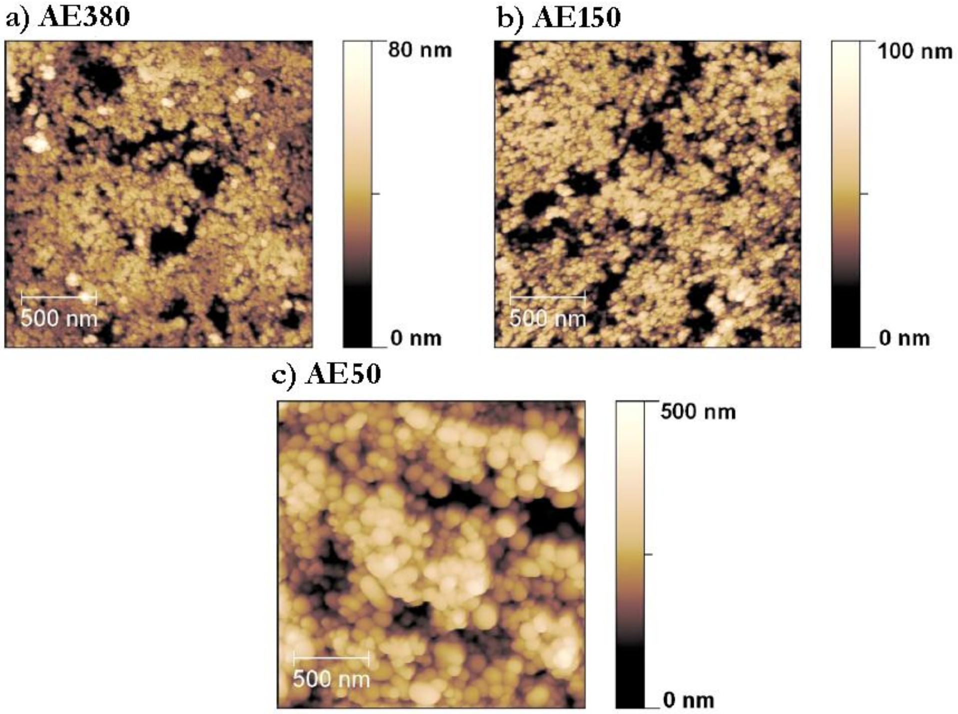

Figure 5.2: AFM images of the powder tablets of the AE380, AE150 and AE50 fumed silica samples.

[45]. Indeed, as discussed in Section 1.1, structural modifications of the silica network can influence the position, shape and amplitude of the R-line, whereas no significant changes were reported for the line peaked at ~800 cm^{-1} [45]. In the case of fumed silica, as we will describe in details in Section 5.1, the R-line is very different in the various fumed silica types, consequently in order to perform a quantitative investigation of the Raman features it is convenient to normalize the spectra to the line peaked at ~800 cm^{-1}.

The spectra of the AE380 sample in form of powders and tablet, shown in Figure 5.1, are enough comparable each other apart form the different signal-to-noise ratio. Moreover, these two spectra are in agreement with the Raman spectrum of the same fumed silica type (AE380) previously reported by Yamada et al. [42]. This finding corroborates the absent of modifications induced by the compacting procedure. It is worth noting that in Figure 5.1 the Raman spectrum of the as-received powder was acquired for about 30 hours, whereas that of the tablet was acquired for about 15 hours. Nevertheless, this latter spectrum is characterized by signal-to-noise ratio about 4 times higher than that of the spectrum of the not compacted powder. Similar considerations apply to all the other fumed silica types, emphasizing the “advantage” in compacting the powders of fumed silica in form of tablet.

As shown in Figure 5.2, where the AFM images of the surfaces of the tablets of the AE380, AE150 and AE50 samples are reported, the tablets consist in an ensemble of particles very close each others characterized by large voids, conferring to the overall sample a certain degree of porosity [130]. As expected, each fumed silica type shows a different mean size of particles. These images further confirm that the compaction procedure induces only a reduction of spaces between the particles. Hereafter, all of the Raman, EPR and luminescence spectra of fumed silica samples will refer to tablets obtained from the powders compacted by the press.

5.1 Structural properties of fumed silica and their modifications induced by thermal treatments

In Figure 5.3 the Raman spectra acquired for all the six fumed silica types are reported. In the same figure a typical spectrum of a bulk silica sample (S300) is shown for comparison. All fumed silica samples exhibit a very different Raman spectrum as compared with that of bulk silica: the R-line is more intense and shifted toward higher frequency, the D_1 and D_2 lines as well as the line peaked to $\sim$980 cm^{-1} are more intense. It is worth noting that these properties are much more pronounced on increasing of specific surface or, in other words, on decreasing the primary particles size. As discussed in Section 1.1, to our knowledge the experimental investigations performed by Raman spectroscopy until now were focussed mainly on the AE380 sample and a direct comparison among the different fumed silica types was lacking. The increase of the amplitude of the line peaked to $\sim$980 cm^{-1}, attributed to the OH vibration mode, with the specific surface was expected as a consequence of the different “ability” of fumed silica types to absorb water on the particle surface (see Figure 3.4) [109, 110]. At variance, the gradual differences found in terms of the R-line and D_1 and D_2 lines, which become more evident on increasing the specific surface, is a more striking feature. Indeed these findings suggest the the different types of fumed silica are characterized by different structural properties, directly related to the nanometric nature of the particles.

To deepen this question and in order to study the changes induced in the structural properties of these samples, three fumed silica types (AE380, AE150 and AE50)

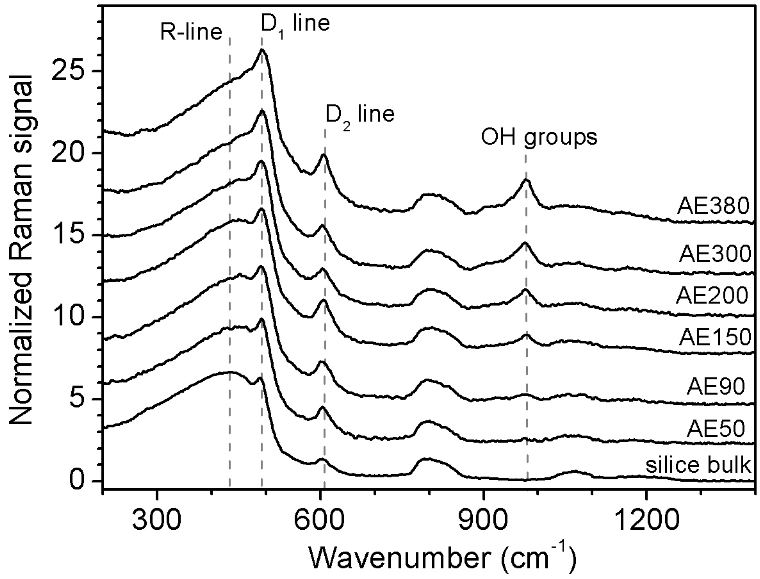

Figure 5.3: Raman spectra acquired for all six of the fumed silica types. A bulk silica Raman spectrum (S300 sample) is reported as reference. Each spectrum is normalized to the amplitude of the line peaked at ~800 cm^{-1}. The spectral features evidenced by the vertical dashed-line are discussed in the text. Spectra are arbitrarily vertically shifted.

were thermally treated for two hours in the range 100÷1000 °C, with steps of 100 °C. We considered distinct samples for each fumed silica type. One sample for each material was treated at only one temperature falling in the range above indicated. In the following, the untreated samples will be referred to as *nickname/0*, whereas the thermally treated ones as *nickname/T*, where *T* indicates the temperature of the treatment in °C units.

Figure 5.4 reports the Raman spectra acquired for (a) AE380, (b) AE150 and (c) AE50 samples before and after thermal treatments at 300, 800 and 1000 °C. In the same figure, a typical Raman spectrum of bulk silica is reported for comparison. To carry out a quantitative analysis, as above discussed, the spectra were normalized to the amplitude of the line peaked at ~800 cm^{-1}. As shown in Figure 5.4, the thermal treatments gradually modify both the R-line and the D_1 and D_2 line features but in different ways. In fact, after the treatment at 1000 °C the R-line of the three fumed silica types is very similar to that of bulk silica, whereas the amplitude of the D_2 line is still significantly different.

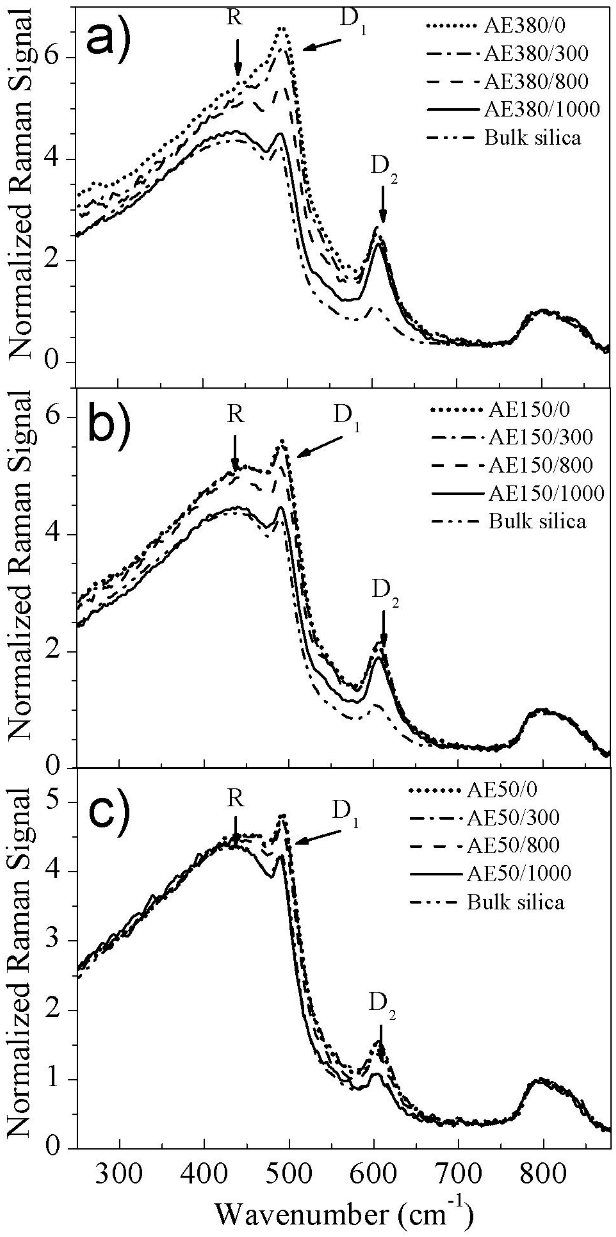

Figure 5.4: Raman spectra acquired for the materials (a) AE380, (b) AE150 and (c) AE50 before and after thermal treatments at 300, 800 and 1000 °C. A bulk silica Raman spectrum is reported as reference. Each spectrum is normalized to the amplitude of the line peaked at ∼800 cm^{-1}. The spectral features evidenced by arrows are discussed in the text.

To investigate in a more quantitative way these changes, we estimated the position of the maximum of the R-line (ω_R) as a function of the thermal treatment temperature. In particular, the R-line position was determined by inspection of the graphs searching the wavenumber corresponding to the maximum of the line. The results are reported in Figure 5.5. In the same figure, the peak position variability determined in the wide variety of bulk silica materials investigated in Chapter 4 is also indicated as a grey stripe. As shown in Figure 5.5, AE150 and AE50 materials exhibit the same trend: the ω_R values do not change up to ~700 °C, whereas they gradually decrease falling into the grey stripe for T>800 °C. At variance, the R-line position in AE380 material is constant up to ~300 °C and thereafter it progressively decreases superimposing for T≥600 °C to the trend observed for AE150 and AE50 materials.

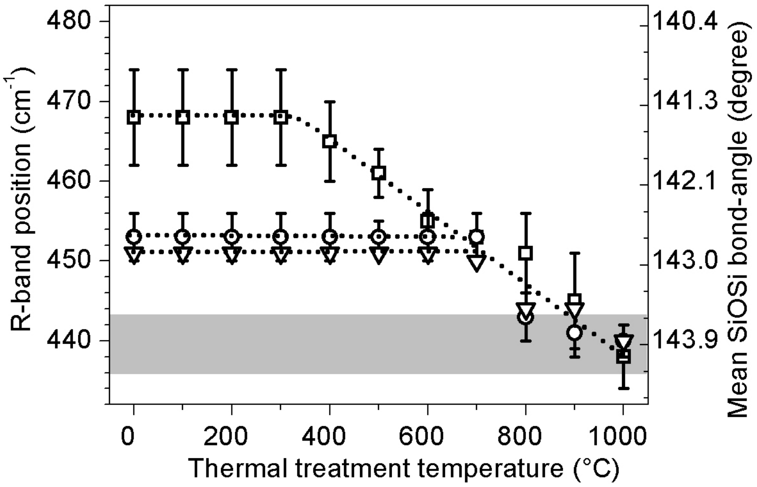

Figure 5.5: Main Raman line position (ω_R) and the $Si - \widehat{O} - Si$ mean bond-angle (θ) of the materials (□) AE380, (○) AE150 and (▽) AE50 as a function of the thermal treatment temperature. The grey stripe represents ω_R variability observed in a lot of bulk silica materials of different commercial origin. Dotted lines are guides for the eye.

In Section 1.1 we reported the relation (Equation 1.1) linking the position of the R-line and the $Si - \widehat{O} - Si$ mean bond-angle (θ) [15]. Through this equation and from the R-line positions, θ values were estimated and reported on the right vertical axis of Figure 5.5. The obtained data suggest that this angle is smaller in fumed silica as compared to bulk one and that it gradually increases by thermal treatments.

To further compare our Raman spectra, we estimated the amplitude of the D_2

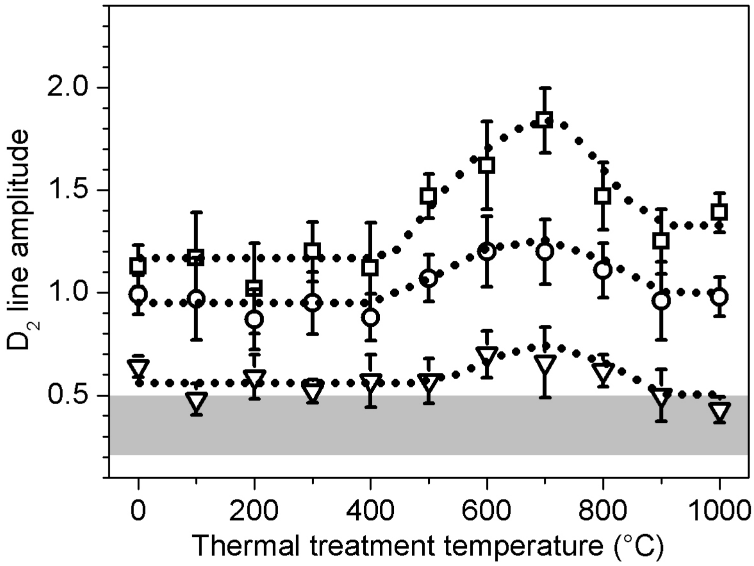

Figure 5.6: D_2 line amplitude in the materials (□) AE380, (○) AE150 and (▽) AE50, estimated from the normalized Raman spectra, as a function of the thermal treatment temperature. The grey stripe represents the D_2 line amplitude variability observed in a lot of bulk silica materials of different commercial origin. Dotted lines are guides for the eye.

line. A similar study for the D_1 line is more difficult because its spectroscopic features are affected by the superposition with the R-line. In details, to evaluate the D_2 line amplitude in our samples, we subtracted an opportune baseline to the normalized Raman spectra, in agreement with the method of analysis previously used (see Chapter 4). In Figure 5.6, we report the D_2 line amplitude as a function of the thermal treatment temperature. In the same figure we indicate with the grey stripe the amplitude variability of the D_2 line estimated in the wide variety of bulk silica materials investigated in the Chapter 4 (See Table 4.1)[b]. As shown in Figure 5.6, fumed silica materials display a very similar trend among them, that is, the D_2 line amplitude does not appreciably change in each material for all thermal treatment temperatures except for the temperatures in the range 500÷900 °C. In this range the D_2 line amplitude first increases then reaches a maximum at T$\sim$ 700 °C and finally it decreases and levels above T= 900 °C.

---

[b] The D_2 line amplitudes reported in Table 4.1 were estimated from the bulk silica spectra normalized to the R-line. The grey stripe in Figure 5.6 refers to the data of that table opportunely rescaled by the amplitude of the line peaked at ~800 cm^{-1} in order to take in to account that the fumed and bulk silica spectra were normalized in different ways.

In addition to the Raman investigation, the effects of thermal treatments were also explored by IR measurements. The IR spectra of AE380, AE150 and AE50 fumed silica materials acquired before and after thermal treatments at 300, 500, 800 and 1000 °C are shown in Figure 5.7. All the IR spectra of untreated samples show the typical broad line in the range 2500÷4000 cm^{-1}, whose main contribution arises from the vibrational modes of physisorbed water on the primary particle surface as discussed in Section 1.3.1 [55, 57, 109, 110]. In agreement with the previous works, we also found that the intensity of this line increases on decreasing the primary particles diameter, or, equivalently, on increasing the specific surface [57, 109, 110]. On the shoulder of this broad line, the narrow line peaked at ~3740 cm^{-1}, assigned to isolated surface silanol groups, can be detected [55, 57–59].

As shown in Figure 5.7, the thermal treatments induce a gradual decrease of the broad band in the range 2500÷4000 cm^{-1} in all of the fumed silica types, and reveal the presence of other specific spectral features in the spectra. In details, two bands at about 3520 cm^{-1} and 3680 cm^{-1} are found, suggesting the presence of SiOH groups engaged in H-bonding with each other [131]. These bands are also affected by the treatments and decrease on increasing the temperature. Since many IR spectra are saturated in the region 2500÷4000 cm^{-1}, we estimated the water content from absorption bands in the range 5000÷5400 cm^{-1} (see insets a1, b1 and c1 of Figure 5.7), ascribed to nearly degenerate combination modes of bending, symmetrical stretching and antisymmetrical stretching modes of water (see Section 1.3.1) [55, 57–59]. From the insets of Figure 5.7, it is possible to note that the shapes of these bands depend on the fumed silica type. In particular, the band profile is more structured on decreasing the particle diameters, suggesting a different contribution of the various vibrational modes. Notwithstanding, we observe that a gradual reduction of the overall band area occurs in all the materials. In Figure 5.8, we report the area of this band, normalized to that of untreated samples, as a function of the thermal treatment temperature. The data suggest that the dehydroxylation process is effective in the same temperature range for AE380, AE150 and AE50 materials. It is worth noting that the IR spectra were taken, at worst, within 8 days from the thermal treatment. Since the samples were kept at ambient condition during this time, re-hydration effects could affect our measurements. However, we can state that the thermal treatments are able to remove water starting from 100 °C since a decrease of the water associated bands is anyway found.

IR spectra were also used to investigate the position of the IR line around

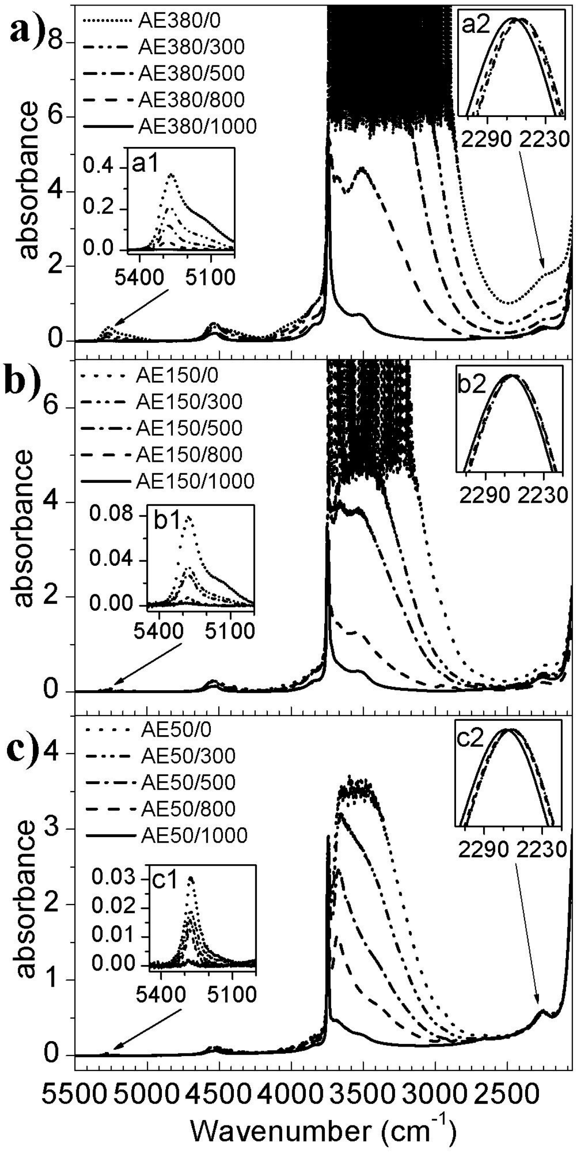

Figure 5.7: IR spectra acquired for the materials (a) AE380, (b) AE150 and (c) AE50 before and after thermal treatments at 300, 500, 800 and 1000 °C. Insets a1, b1 and c1 are zooms of the line around 5200 cm^{-1}, assigned to the combination modes of water molecules ($\nu_1 + \nu_2$ and $\nu_2 + \nu_3$) see text. Insets a2, b2 and c2 are zooms of the line around 2260 cm^{-1}, subtracted by an opportune baseline and normalized to the maximum, assigned to the overtone of the $Si - \widehat{O} - Si$ stretching vibration at 1100 cm^{-1}.

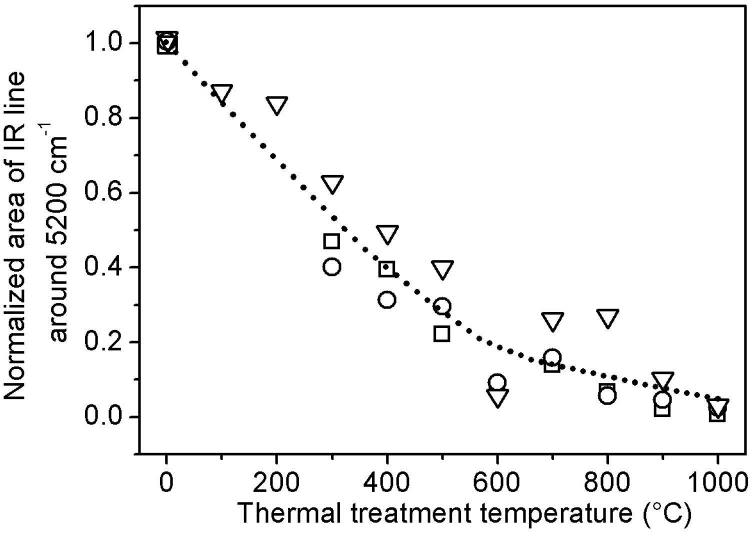

Figure 5.8: Area of IR line around 5200 cm^{-1}, normalized to that of untreated samples, for materials (□) AE380, (◯) AE150 and (▽) AE50 as a function of thermal treatment temperatures. The error bar is comparable to the size of the symbols. Dotted line is a guide for the eye.

2260 cm^{-1}, assigned to the first overtone of the $Si-\widehat{O}-Si$ stretching vibration mode [22] and related to the fictive temperature T$_f$ through Equation 1.2. As discussed before, T$_f$ is relevant because it is related to the average value of the $Si-\widehat{O}-Si$ bond-angle (see Section 1.1) [23–25]. As shown in Figure 5.7, in many spectra of our samples, one can not identify a maximum of the line around 2260 cm^{-1} because it is dramatically overlapped to the tail around ~2100 cm^{-1} (see for example AE380/0, AE380/300 and AE150/0 samples). In addition, for those samples in which the maximum can be recognized, it typically falls below 2255 cm^{-1}. These findings prevent to directly estimate the fictive temperature and $Si-\widehat{O}-Si$ mean bond-angle from our IR spectra. In fact, as discussed before, the relation linking the peak position and T$_f$ (Equation 1.2) is only valid in a small frequency range from ~2255 to ~2263 cm^{-1} and when the peak is estimated without any baseline subtraction [23–25]. Accounting for the above mentioned limitations, we limited ourself to obtain only merely qualitative information on $Si-\widehat{O}-Si$ mean bond-angle from IR spectra, which can serve to support results obtained from Raman measurements. To this aim, we analyzed the region around 2260 cm^{-1} by subtracting a linear baseline from the IR spectra. The spectra obtained with this method are reported, normalized to the maximum, in the insets a2, b2 and c2 of Figure 5.7 and show a line peaked at about 2260 cm^{-1} in all of the samples. This line has similar shape independently on the temperature, but the peak position shifts towards higher frequency on increasing the temperature.

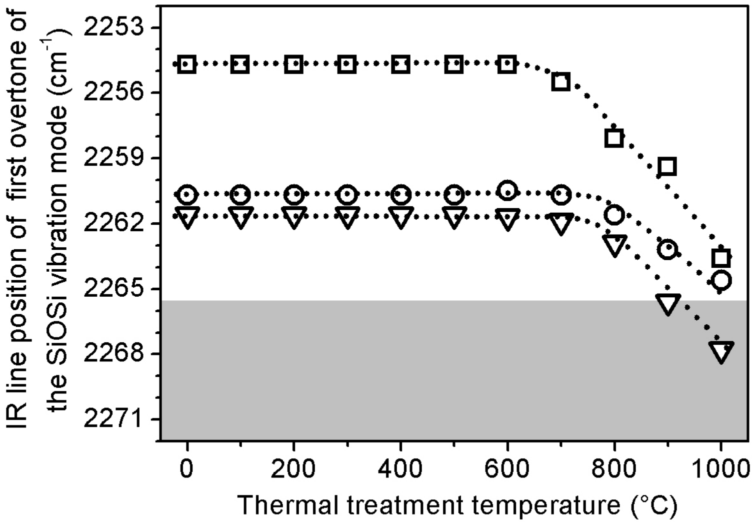

Figure 5.9: Peak position of the 2260 cm^{-1} band, estimated by a baseline subtraction, in the materials (□) AE380, (◯) AE150 and (▽) AE50 as a function of the thermal treatment temperature. The grey stripe represents the peak position variability observed in a lot of bulk silica materials of different commercial origin. The error bar is comparable to the size of the symbols. Dotted lines are guides for the eye.

The peak positions obtained from this analysis method for AE380, AE150 and AE50 materials are reported in Figure 5.9. In the same figure, we indicate with the grey stripe the variability obtained for this line in a wide variety of bulk silica materials of different commercial origin, estimated applying the same analysis method used for the fumed silica samples. So, even if the line position is shifted and it can not be related to T_f, the comparison between fumed and bulk samples is still a valid procedure and it can give information on the different structural properties of the materials. The data reported in Figure 5.9 show a trend in qualitative agreement with that of the R-line position reported in Figure 5.5. In particular, all the fumed silica untreated materials have an IR line peak position different from that of the bulk silica. Furthermore, AE150 and AE50 have similar peak positions, which are not modified up to ∼700 °C. For higher temperatures these values monotonically decrease towards the bulk silica values. On the other hand, the AE380 material shows a line peaked at much lower frequency position, which remains essentially stable up to ∼600 °C. On further increasing the thermal treatment temperature, also for this material the line position shifts towards the bulk silica values. These thermally induced changes resemble those observed for the R-line position, even if for the AE380 material this latter line starts to change at lower temperature. This discrepancy could be attributed to the difficulty of the analysis of IR spectra.

5.1.1 Discussion

Our experimental data clearly show that the fumed silica Raman spectral features, such as the R-line, the D_1 and D_2 lines, are very different from those of ordinary bulk silica on decreasing the primary particles size (on increasing the specific surface area). These findings naturally suggest that these differences, which can be attributed to changes in structural properties of the primary particles, arise from their nanometric size. By thermally treating fumed silica, we found that these differences are removed for the R-line, whereas the D_2 line maintains a different amplitude with respect to bulk samples. To investigate in details the uncommon structural properties of fumed silica, we extracted some quantitative information from Raman and IR spectra as a function of the thermal treatment temperature. In particular, we focused on the modification of the $Si-\widehat{O}-Si$ mean bond-angle, on the concentration of 3-membered rings and on the water content.

The results on the R-line of Raman spectra can be interpreted by a modification of θ by using Equation 1.1. The data reported in Figure 5.5 show that the θ values in the untreated fumed silica materials are θ=141.4±0.5 °, 142.6±0.2 ° and 142.8±0.1 ° for AE380/0, AE150/0 and AE50/0, respectively, and they gradually decrease by thermal treatments. At temperature of 1000 °C, these values fall within the variability of $Si - \widehat{O} - Si$ mean bond-angle (143.6 ° $\leq \theta_{bulk} \leq$ 144.2 °) estimated in bulk silica materials of different commercial origin. Besides, by the comparison of the Raman spectra of the untreated fumed silica samples with those of bulk silica materials mechanically densified (see Figure 1.5 in Section 1.1), we estimated that AE380 is $10 \div 20$ % densified with respect bulk silica materials.

Further support to the change in θ induced by thermal treatments is found by the modification of the IR line position around 2260 cm^{-1} reported in Figure 5.9. In fact, the observed increase of the peak position in wavenumbers indicates a increase of θ [23, 24]. For the reasons discussed in the previous section, it is not possible to extract quantitative values of this angle to be compared with those obtained by the R-line position. Nevertheless, the data trend reported in Figures 5.5 and 5.9 for Raman and IR spectra, respectively, suggest a similar tendency of the $Si-\widehat{O}-Si$ mean bond-angle to increase by thermal treatment.

Our untreated samples are characterized by smaller bond-angle than bulk silica, as shown in Figure 5.5. In Section 1.1, we reported that a decrease of the $Si-\widehat{O}-Si$ bond-angle can be induced in bulk silica materials by permanent densification. From this point of view, it is worth noting the Raman spectra of untreated fumed silica samples are similar to the spectra of bulk silica materials mechanically densified (for example compare the AE380/0 spectra reported in Figure 5.4 with the spectra of Figure 1.5(b)). Furthermore, the D_1 and D_2 Raman lines, assigned to 4- and 3-membered rings, respectively, are more intense in fumed silica materials than in bulk ones (see Figure 5.4). Basing on the above discussion reported in Section 1.1, our findings suggest that the ring distribution in fumed silica materials should be slightly shifted towards smaller-membered rings respect to bulk silica. The angle θ changes induced on fumed silica materials by thermal treatments can be interpreted in terms of modification of ring distribution. In other words, it could be expected that when changes are induced on θ (R-line modification), these variations should be reflected on the population of 4- and 3-membered rings too. However, our results are not in agreement with this scheme. In fact, as shown in Figure 5.5, the monotonic increase of θ for T>500 °C suggests that the ring distribution in all three fumed silica types should be gradually shifted towards larger-membered rings. In contrast, as shown in Figure 5.6, the 3-membered ring content increases in the range of temperature 500÷800 °C.

The above discussed findings show that the population of 3-membered rings and of rings with n> 4 (contributing to the R-line) have different evolution by thermal treatments. In order to interpret these features, it can be supposed that the rings are differently spatially distributed inside the primary particles. In particular, in agreement with the analysis of simulative [39, 40] and experimental works [81] reported in Section 1.2, a shell-like structural model of the primary particles of fumed silica can be suggested as schematically shown in Figure 5.10(c). In this scheme, a surface-shell exists for each particle, characterized by strong structural constraints with a network consisting mainly of small n-membered rings (n=3 and/or 4). In addition, a core-shell is present showing a network similar to that of the bulk one but with a ring distribution slightly shifted towards small membered rings. One can imagine that these different atomic structures of the primary particle are consequences of the strains imposed by the nanometric size of the system. In fact, the surface and near surface are those regions of the particle more affected by the strains resulting from the high radius of curvature.

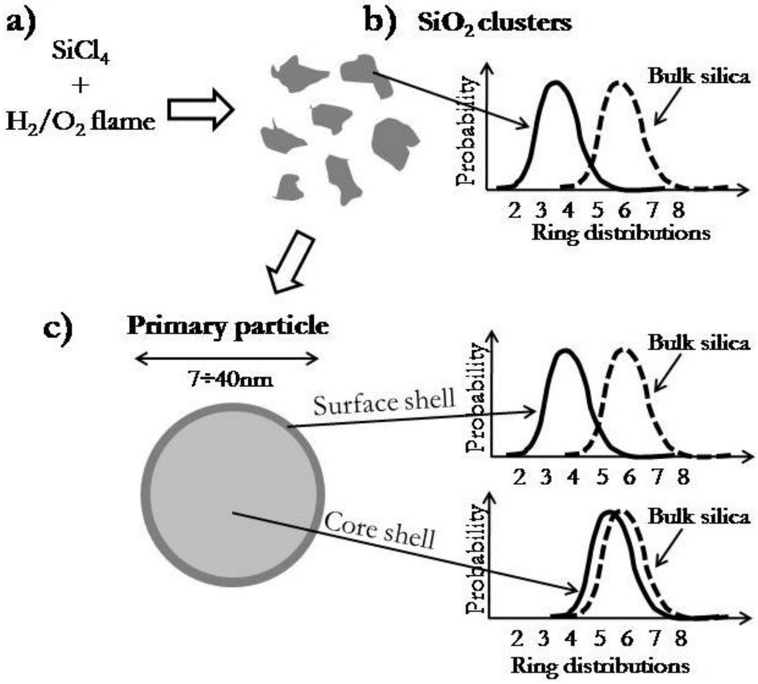

Figure 5.10: Schematic representation of the formation of fumed silica primary particles: (a) $SiCl_4$ hydrolysis in H_2/O_2 flame, (b) formation of small SiO_2 clusters and, finally, (c) the primary particle. The shell-like model of this latter with a core and surface region is shown. The ring distribution of small clusters, bulk silica, core- and surface-shells of primary particle, are qualitatively reported.

It can be suggested a simple explanation of the reason for which the network of a primary particle organizes itself in a shell-like structure. The theoretical calculations reported in Section 1.2 demonstrated that the network of small free isolated $\{SiO_2\}_n$ clusters ($5 \leq n \leq 20$) are constituted mainly by small-membered rings [132–134]. This finding was ascribed to the fact that the small-membered rings, as compared to bigger ones, are geometrically and energetically favored in forming a stable network of few SiO_4 elements. As shown in the scheme of Figure 5.10, one can imagine that, in the starting stages of the fumed silica synthesis process ($SiCl_4$+H_2/O_2 flame), these small clusters represent the early blocks leading to the formation of the primary particles. In this scheme, when these clusters are connected together to build up the primary particle (constituted by many hundreds of these clusters), the original structural strains pertaining to each cluster, forming the core region of the primary particle, are partially released thanks to the increase the degrees of freedom. In other words, the fusion of the primary clusters into larger ones allows the reorganization of the network, so that the ring distribution shifts towards larger-membered rings (compare Figure 5.10(b) and 5.10(c)). In this respect, it is expected that the structure of the core region becomes similar but not necessarily identical to that of bulk silica. At variance, the clusters, connected in proximity of the surface or near surface layer of the particle, remains more strained. In agreement with this model, simulative works on SiO_2 nano-particles showed that the outer layer presents a different atomic network as compared to the inner part [39, 40]. It was also found that the thickness of the outer layer is about two reticular steps ($\sim 2 \div 3$ $\mathring{A}$) and independent of particles sizes (see Section 1.2). In our experimental system, a thickness $\sim 2 \div 3$ $\mathring{A}$ for the exterior layer gives a (surface-shell volume)/(particle volume) ratio of about 20, 10 and 4 % for particles with 7, 14 and 40 nm diameter, respectively, showing that depending on the particle size, the surface layer could give a relevant contribution to the overall particle properties.

Our experimental results can easily be interpreted by the shell-like model above presented. In fact, the high intensity of the D_1 and D_2 Raman lines, characterizing all 3 types of untreated fumed silica (see the dotted line in Figure 5.4), is mainly due to the high content of 4- and 3-membered rings, respectively, in the surface-shell of the primary particles. In particular, as shown in Figure 5.6, the D_2 line amplitude of the untreated samples monotonically decreases with increasing the particles diameter. This result is in agreement with the shell-like model, in which the (surface-shell volume)/(particle volume) ratio decreases on increasing the particles size, if the outer layer is of almost constant thickness. On the other hand, the evident shift of the Raman R-line position, characterizing all 3 types of untreated fumed silica, is mainly attributable to the residual strains of the core-shell network of the particles. As reported in Figure 5.5, this line is much more shifted towards high frequency on decreasing the particles size as a consequence of the fact that the smaller the primary particle is small, the more strained the network of the core-shell.

The application of thermal treatments is able to change the overall structural properties of the fumed silica samples: the water content, R-line and D_1 and D_2 lines are modified. Basing on the above illustrated shell-like model for the nano-particles, we can explain these results. First of all, we notice that as reported in Figure 5.8, the water content monotonically decreases starting from the first treatment temperature of 100 °C independently of the material. At variance, the R-line position starts to change above 400 °C at a value of the temperature which depends on the material (see Figure 5.5). These findings suggest that the network modifications of the core-shell are independent of the drying process. This can also be supported considering the fact that water is adsorbed on the particles surface and, therefore, the core-shell and the water layer are spatially separated by the surface-shell. For this reason, it is not surprising that the shift of the R-line towards lower frequency is not related to the water release; it occurs for $T \geq 400$ °C because of the thermal relaxation of residual strains in the core-shell network. It is important noting that the modification of the R-line starts above 400 °C for the AE380 material and above 800 °C for AE150 and AE50. This can be attributed to different activation energies for stress removal in the various materials. In details, AE150 and AE50 untreated materials have similar initial strained network of the core-shell with comparable values of θ and their modifications are triggered at the same temperature. At variance, AE380 untreated material is characterized by a stronger initial strain (see the lower θ values in Figure 5.5), which is released starting at lower temperature.

On the other hand, as shown in Figure 5.6, the D_2 line increases above 400 °C, reaches a maximum at ~700 °C and successively decreases for higher temperature with a dependence which looks similar in all fumed silica types. The increase of this Raman line can be related to the dehydroxylation process. Indeed, as previously suggested (see Section 1.3.1)[42, 58, 135, 136], around T~700 °C the silanol groups on the particles surface, no longer hydrogen-bonded to water molecules, can interact with each other forming $Si-\widehat{O}-Si$ bridging bonds ($\equiv$Si-OH HO-Si$\equiv$ $\rightarrow$ $\equiv$SiOSi$\equiv$ + H_2O). This hypothesis is somehow corroborated by the decrease of amplitude of the IR bands, related to SiOH groups engaged in H-bonding with each other, observed in Figure 5.7. It is worth noting that the re-hydration does not affect this conclusion since hardly reversible dehydration can be observed above 400 °C [136]. The $Si-\widehat{O}-Si$ bridging bond generation, localized on the particle surfaces, promotes the formation of 3-membered rings and therefore the D_2 line increases [42, 135]. It is important noting that the increase of the D_2 line amplitude around T=700 °C is more evident on decreasing the particle diameters (see Figure 5.6). This finding further corroborates the precursor role of the surface silanol groups in the formation of 3-membered rings by thermal treatments. Indeed, the concentration of surface silanol groups (OH/cm^3) is larger on decreasing the particle size [109, 137]. For temperatures above 700 °C, the decrease of the D_2 line amplitude can be interpreted by the occurrence of a different physical process. In this latter case, the particle surface, mainly constituted by 3-membered rings, is involved in the particle-to-particle bonding originating the formation of more complex structures and of larger membered rings, with the ensuing decrease of D_2 line amplitude. In this respect, it is guessed that the structural modifications involve the single particle below 700 °C, whereas at higher temperature structural changes are due to build up of particle-to-particle linking (sintering effects).

5.2 Emission properties of fumed silica: the blue band

Fumed silica, as discussed in Section 1.3.2, is characterized by the blue luminescence band excited in a wide range extending over visible and UV energies [62–64, 67, 68]. This emission activity has never been found in bulk silica and consequently it is assumed to be typical of silica nanoparticles. Notwithstanding the studies carried out, the properties of this photoluminescence band have not been fully clarified. In particular, the connection with the nanometric nature of fumed silica and the exact physical origin of this emission are lacking. In this section we report a detailed investigation on the luminescence properties of the blue band and through the structural information obtained by Raman spectroscopy, we will try to clarify the influence of the size and matrix structure on the blue band emission properties.

In Figure 5.11 the photoluminescence spectra, acquired for the AE300 sample under excitation at 3.65 eV before and after a thermal treatment of 2 h at 300 °C, are reported. As shown in the figure, the untreated sample is characterized by a broad asymmetric photoluminescence band peaked at about 3 eV (dashed line). This band, observed also in other untreated fumed silica types (not reported here), is attributed to hydrocarbon groups physisorbed on the primary particle surfaces [62–64]. As evidenced in Figure 5.11 and in agreement with previous works [62–64], the effect of the considered thermal treatment is to induce a blue band, peaked at about $2.7\div2.8$ eV and with FWHM$\sim$0.8 eV, that overwhelms the contribution of hydrocarbons emission. A band with analogous spectral properties (position and FWHM) was observed in all the other fumed silica types (not shown here). On the other hand, as discussed in details successively, an evident dependence on the fumed silica type of the blue band amplitude was observed.

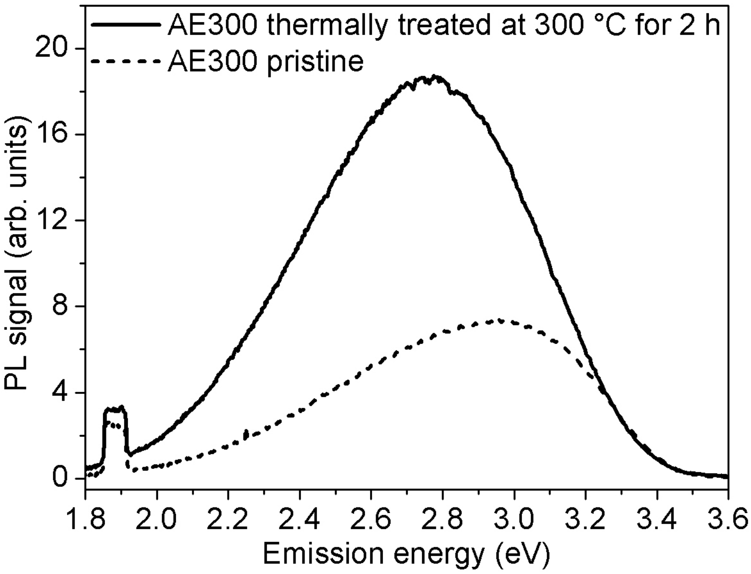

Figure 5.11: PL spectra acquired for the AE300 sample before (dashed line) and after the thermal treatment of two hours at T=300 °C (solid line), excited at 3.65 eV

Since it was reported that the induction of the blue band in a AE380 sample strongly depends on the thermal treatment, we carried out two experimental investigations in order to deepen this dependence. In the first experimental, isochronal treatments of 2 h from 100 °C up to 700 °C with 100 °C steps on one AE300 sample were considered. After each treatment, the amplitude of the blue band excited at 3.65 eV was estimated and is reported in Figure 5.12 as a function of the thermal treatment temperature. The emission of this band increases up to a temperature of about 300÷400 °C and then decreases rapidly for higher temperatures, as qualitatively indicated by the dashed line. We carried out the same experiment for one AE90 sample, obtaining a compatible data trend (not shown here). These findings, in agrement with previous works in which the same thermal treatments were performed on the AE380 material [62–64], suggest that the maximum increase of the blue band is at about 300÷400 °C for thermal treatments of 2 h in all of the fumed silica types.

The second experiment that we considered concerns isothermal treatments at T=300 °C for different time intervals on the AE300 sample. The amplitude of the blue band excited at 3.65 eV was estimated after each treatment and is reported in Figure 5.13 as a function of the thermal treatment time duration. As evidenced, the amplitude of the band increases up to 2 h and then reaches a constant value

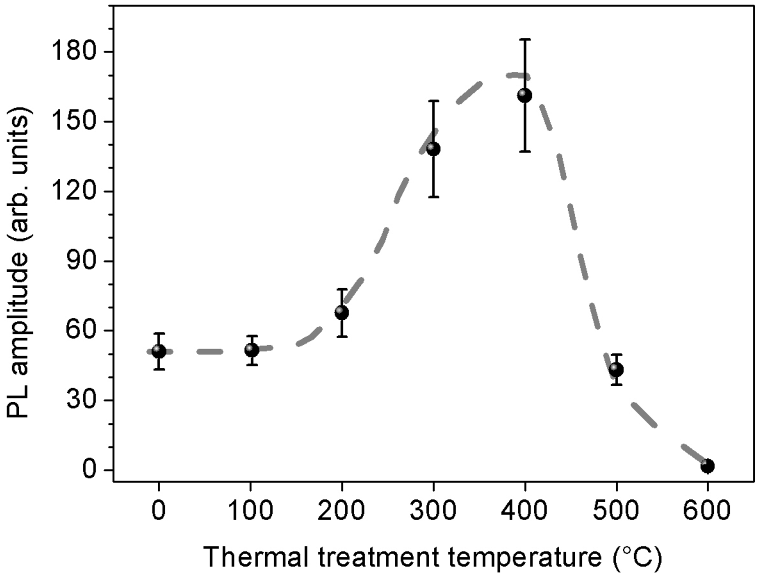

Figure 5.12: Blue band amplitude of the AE300 sample, estimated from the spectra excited at 3.65 eV, as a function the isochronal (2 h) thermal treatment temperature. The dashed line is a guide for the eye.

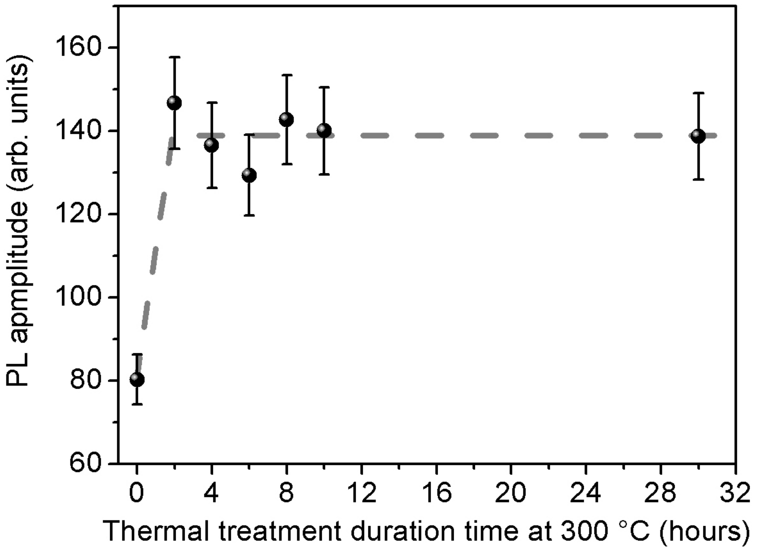

Figure 5.13: Blue band amplitude of the AE300 sample, estimated from the spectra excited at 3.65 eV, as a function the thermal treatment time duration at the temperature of 300 °C. The dashed line is a guide for the eye.

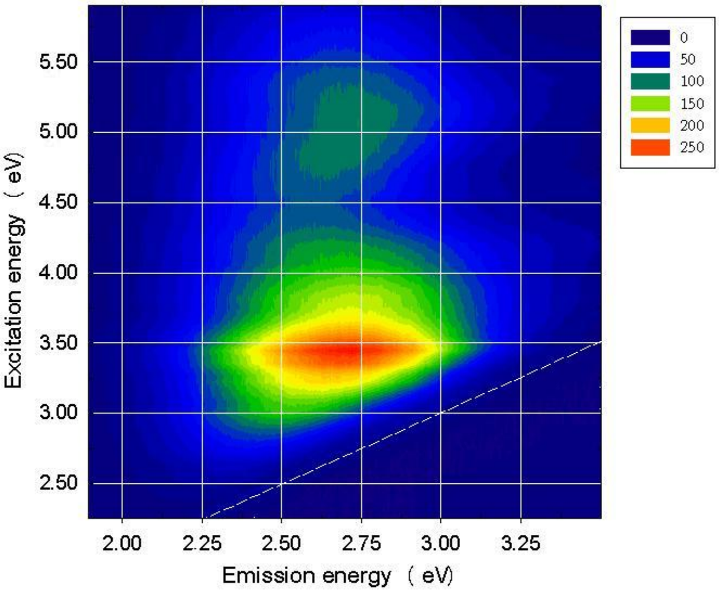

Figure 5.14: Contour plot of the blue band amplitude of the AE300 sample, thermally treated at 300 °C for 2 h, collected at various excitation and emission energies. The intensity is indicated by the color scale.

qualitatively indicated by the dashed line. Since we observed a similar data trend for the AE90 sample (not shown here) even if with a different final PL amplitude, it is reasonable to assume that similar dependence on the thermal treatment time and temperature applies to the other fumed silica types.

On the basis of the findings reported in Figures 5.12 and 5.13, we chose to thermally treat all of the fumed silica samples reported hereafter for 2 h at 300 °C in order to investigate the properties of the blue band. In particular we studied the spectral features as a function of the excitation energy and the time dependence of this band. Since no evident differences were observed in terms of the position, FWHM and life time of blue band in various fumed silica types, we report the results obtained only for the AE300 type.

The contour plot of the blue band amplitude as a function of the excitation and emission energy is shown in Figure 5.14, where the amplitude is indicated by the color scale. The sample is characterized by a wide emission range with a intensity peak around at 2.7÷2.8 eV and by a wide excitation energy range from the visible up to UV, with the maximum excitation at ∼3.5 eV. Moreover, the contour plot

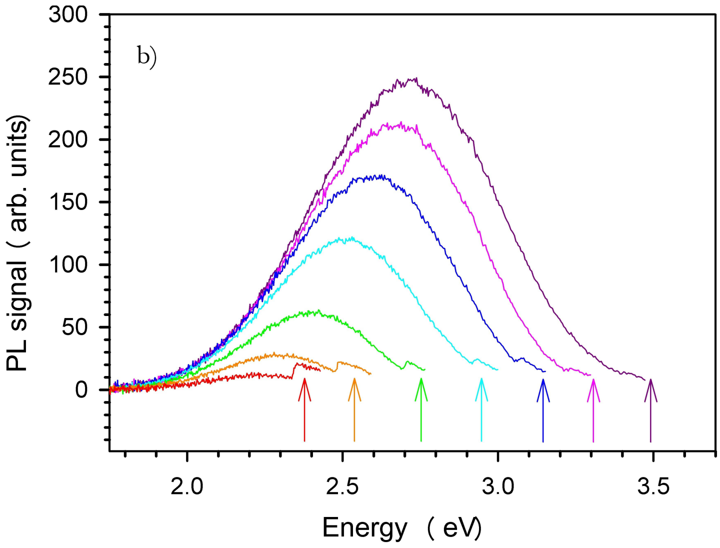

Figure 5.15: Blue band emission spectra of the AE300 sample, thermally treated at 300 °C for 2 h, detected under different E_{exc} as indicated by the arrows.

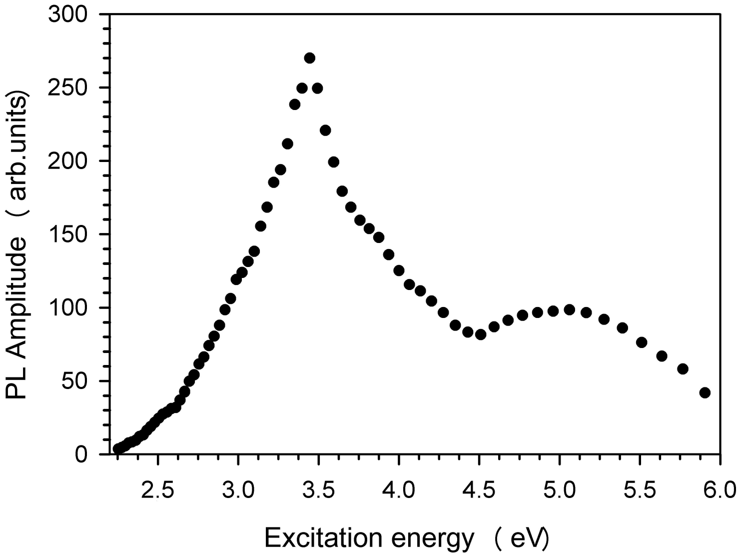

Figure 5.16: Blue band amplitude of the AE300 sample, thermally treated at 300 °C for 2 h, as a function of the excitation energy.

evidences that a modification of the emission line shape for excitations lower than ~3.5 eV occurs. This effect is better shown in Figure 5.15, where the blue band spectra acquired at different excitation energies (indicated by the arrows for each spectrum) are reported. In particular, for excitation energies between ~6 and ~ 3.5 eV (not shown in Figure 5.15), the blue band line shape is almost the same: the position and FWHM are 2.7÷2.8 eV and 0.7÷0.8 eV, respectively. On the other hand, for excitation energies lower than ~3.5 eV the blue band line shape is dramatically modified. Indeed, even if it remains a quite bell-shaped curve, the peak position shifts towards lower energies and the width decreases on decreasing the excitation energy (see Figure 5.15). For example, we estimated that for the 2.38 eV excitation the peak position and FWHM are 2.25±0.02 eV and 0.32±0.04 eV, respectively. In other words, one can say that the blue band is emptied of the components at higher energies for excitation energies lower than ~3.5 eV. This finding strongly suggests that this band is characterized by a broad inhomogeneous distribution of the emitting centers.

In Figure 5.16, the PL amplitude measured at the peak of each emission spectrum as a function of the excitation energy is shown. In agreement with the contour plot of Figure 5.14, the presence of two excitation peaks around 5.0 and 3.5 eV is clearly evident. In this context, it is important to note that a similar excitation spectrum was found by Uchino et al. through conventional PLE spectra, monitoring the intensity of the blue band with emission energy fixed at 2.82 eV for the AE380 sample [62]. Obviously this latter method does not reproduce the exact excitation pathway because, as shown in Figure 5.15, it is affected by the emptiness of the blue band components for excitation energies lower than ~3.5 eV. In any case, the overall excitation spectrum that we obtained and that reported by Uchino et al. are qualitatively in agreement.

In order to deepen the investigation of the inhomogeneous properties of the blue band, we acquired the decay profile excited at 3.65 eV and monitored at different emission energies. In particular, the decay curves for the emission at 2.38, 2.81 and 3.13 eV are shown in Figure 5.17. Each curve, characterized by a timescale of ns order, has a decay profile that deviates from a single exponential law (stretched decay profiles) and is faster on increasing the emission energy. In order to make more evident this latter effect, we estimated for the different emission energies the lifetime τ, measured as the time necessary to reduce the PL intensity to 1/e. The data obtained from this analysis, reported in the inset of Figure 5.17, show that τ

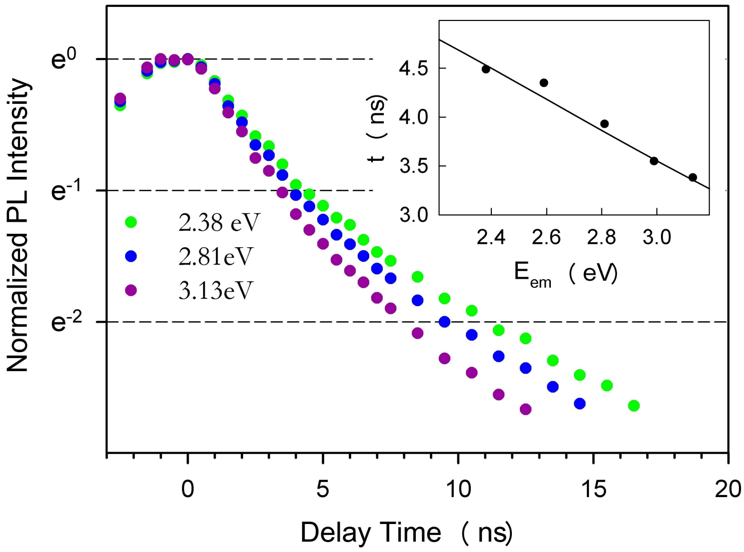

Figure 5.17: Semilog plot of the PL decay monitored at different emission energies under excitation at 3.65 eV. The inset shows the lifetime, estimated as the time necessary to reduce the PL intensity to 1/e, as a function of emission energy.

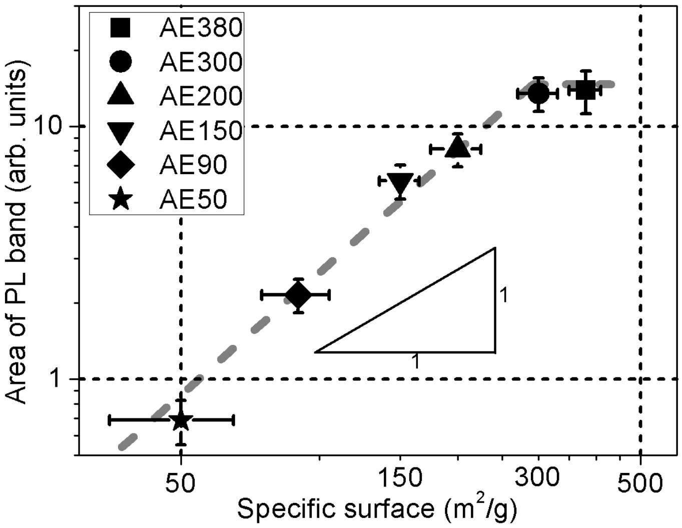

Figure 5.18: Blue band area, estimated in the fumed silica PL spectra excited at 3.65 eV, as a function of the specific surface. All of the samples were thermally treated at 300 °C for 2 h. The dashed-line passing through the data points indicates a growth proportional to (specific surface)$^{1.7}$ up to 300 m^2/g and a constant value for higher specific surface.

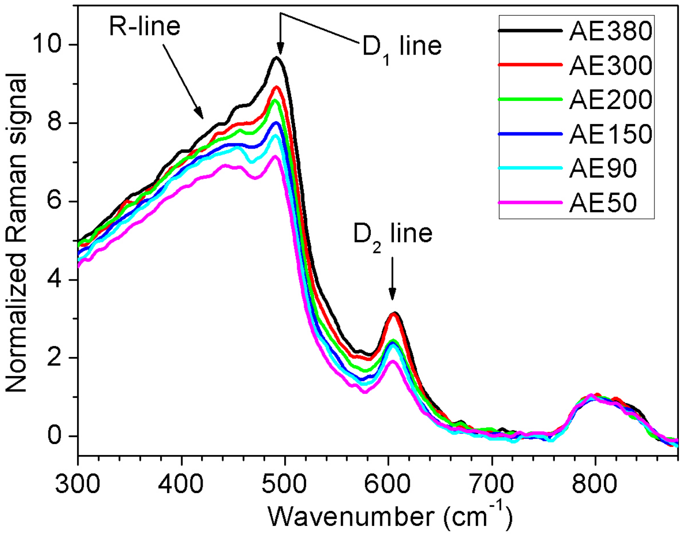

Figure 5.19: Raman spectra of all of the six fumed silica types thermally treated at 300 °C for 2 h. Each spectrum is normalized to the amplitude of the line peaked at ~800 cm^{-1}.

decreases on increasing the emission energy. This finding corroborates the idea that the blue band has a broad inhomogeneous distribution, in which each homogeneous component is characterized by a different life time.

Apart from the amplitude of the blue band, all of the other observed properties (peak position, FWHM and lifetime) are comparable in all the fumed silica types, suggesting that these properties are not directly related with the nanometric size of the fumed silica particles. In order to clarify the reason for which the blue band is absent in the bulk materials, we estimated the area of the blue band in all of the six fumed silica types excited at 3.65 eV. The data obtained are reported in Figure 5.18 as a function of the specific surface. In this figure, as shown by the dashed line, the blue band area increases on increasing the specific surface (S), with the exception of the AE380 sample that shows the same value of the AE300 sample. In particular we estimate that the PL amplitude is proportional to $\mathrm{S}^{1.7\pm0.1}$ in the range $50 \leq S \leq 300$. It is worth remembering that, as discussed before, all of the considered fumed silica samples were thermally treated at 300 °C for 2 h.

The Raman spectra, acquired for the same samples of Figure 5.18, are reported in Figure 5.19. In agreement with Raman spectra reported before, each spectrum is normalized to the amplitude of the line peaked at ~800 cm^{-1}. As discussed in Section

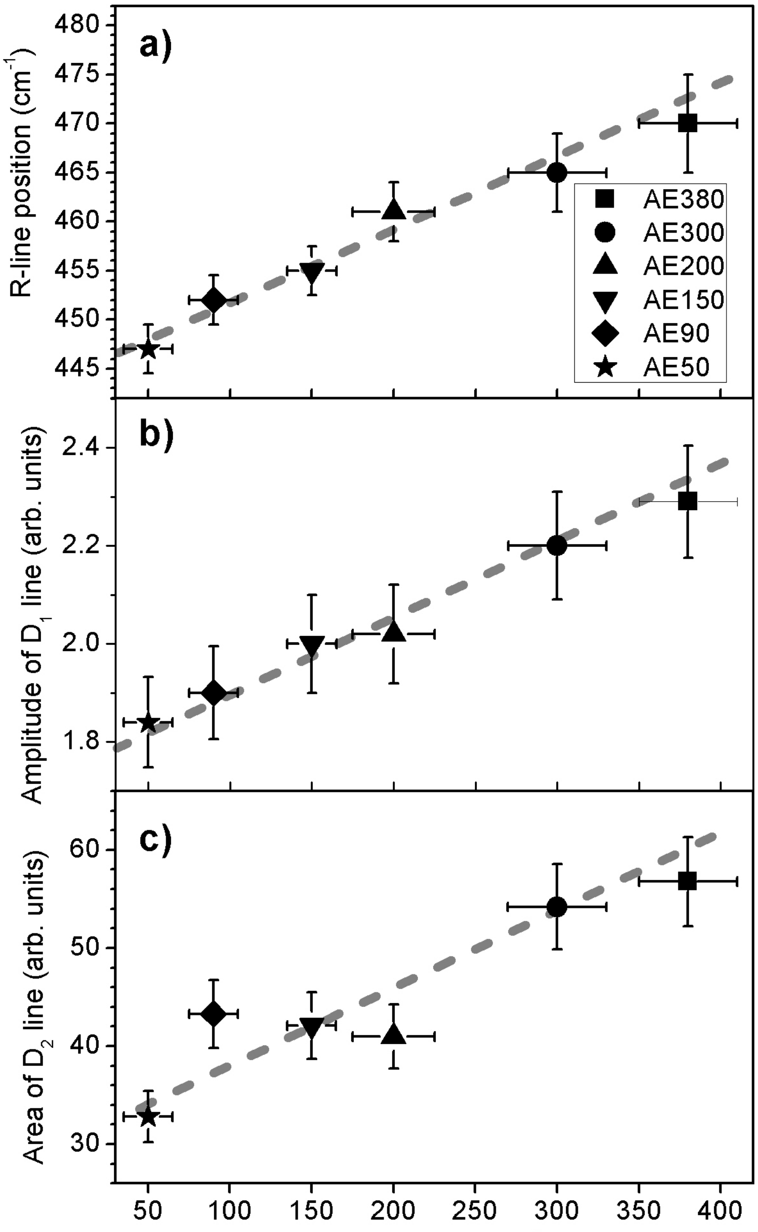

Figure 5.20: a) R-line position, b) amplitude of the D_1 line and c) area of the D_2 line estimated from the fumed silica Raman spectra reported in Figure 5.19, as a function of the specific surface. The dashed lines passing through the data points in each panel indicate a linear growth as a function of the specific surface.

5.1, no evident differences of the intrinsic Raman spectral features between the untreated fumed silica samples of Figure 5.3 and those of Figure 5.19 (thermally treated at 300 °C for 2 h) appear. Indeed, on the basis of the investigation carried out by the isochronal thermal treatments (see Figures 5.5 and 5.6), structural modifications can be induced only for thermal treatments of 2 h at $T \geq 400$ °C. This finding suggests that the blue band is not originated from the structural modifications induced by the thermal treatments.

To investigate the Raman features in a more quantitative way the R-line position, the amplitude of the D_1 and the area of the D_2 lines were determined and are reported in Figure 5.20. To estimate the D_1 line amplitude and D_2 line area, we subtracted opportune baselines to the normalized Raman spectra. In more details, as discussed before, the D_1 line amplitude is hard to estimate because it is partially overlapped to the R-line. However, a qualitative information on the different D_1 line amplitudes in all of the six fumed silica types can be obtained by subtracting a line that is tangent to the spectra on the high wavenumber side around 540 cm^{-1} and that passes at about 480 cm^{-1} on the high wavenumber side of the R-line maximum. The D_2 line area was determined subtracting a straight line tangent to the D_2 line tails as discussed previously. The data reported in Figure 5.20 show a gradual and common trend of the Raman features investigated: the R-line position linearly shifts towards higher energies and the Raman signal of D_1 and D_2 lines linearly increase on increasing the specific surface (see the dashed lines drawn as guides for the eye).

5.2.1 Discussion

The above reported data evidence that a blue emission is induced by thermal treatments at 300 °C in all the investigated fumed silica types. This band is characterized by a peak position and width independent of the particles size. These findings confirm the observation reported in literature for fumed silica sample with 380 m^2/g specific surface [62, 63]. On the other hand, our data enable an extended comparison because we considered particles with different size. Consequently, it is possible to investigate the origin of the emission in connection to the nanometric nature of fumed silica. In fact, as reported in Figure 5.18, we found that the PL signal monotonically increases with the specific surface. This result can justify the absence of this emission in bulk silica and suggests that this band is strongly related to the nanometric nature of the material. In more details we have found that the emission amplitude is proportional to $S^{1.7\pm0.1}$ up to the $S\sim300$ m^2/g sample and then it is almost constant for S≥300 m^2/g.

In order to determine the origin of emitting defects we consider that they should not be simply surface defects. In fact, if the defects were located on the surface of the particles their population should be proportional to the specific surface. At variance we found a non linear dependence on S and in addition the emission amplitude reaches an almost constant value for S≥300 m^2/g. To interpret the trend reported in Figure 5.18, we considered the shell-like model discussed in the previous sections. According to this model it can be supposed that the defects are localized inside the surface-shell with constant concentration. As a consequence, the total number of emitting defects in a given sample is proportional to the overall surface-shell volume. This volume, by simple geometrical considerations, is proportional to S×δ, because δ is small with respect to the diameter of the particle. The above estimation of the surface-shell volume proportional to S is valid for all the fumed silica types apart from the AE380. In fact, this latter type is considered an exception since, as discussed in Section 3.1.1, its larger S is due to a certain surface roughness with respect to the particles of the other fumed silica types [109, 110]. As a consequence, the surface-shell volume of the AE380 is not simply related to S. By considering the data reported in Figure 5.18, the similar emission of the AE300 and AE380 is then interpreted on the basis of the fact that they have the same mean diameter of particles and so almost the same surface-shell volume. Consequently, the shell-like model enables to justify the same emission amplitude of the AE300 and AE380 samples, which is not explained assuming the emission origin by surface defects. Nevertheless, this model predicts again a linear dependence of the blue emission on S. By contrast, the data show a dependence as $S^{1.7}$. This difference suggests that the emission should be affected also by other properties. In this respect, we considered the Raman spectra in order to have insight on the structural properties of the fumed silica samples. As reported in Figure 5.20, the R-line position, and the D_1 and D_2 lines signals are similarly influenced by changes of S. In particular, the shift of the R-line towards higher energies and the increase of the D_1 and D_2 lines signals are linear with S. These spectral features, as discussed in details in Section 5.1, are interpreted in terms of smaller $Si - \widehat{O} - Si$ mean bond-angle (smaller density) of the network of each particle on increasing S. Because it was shown on bulk silica materials that the creation efficiency of point defects is higher in densified samples [76, 138], we can assume that a similar effect is also valid for the silica nano-particles. On the basis of these considerations, we suggest that the defects responsible for the blue emission are induced in the surface-shell more efficiently in those samples having a more densified structure. We can consequently write a qualitative relation for the emission amplitude:

$$I_{\mathrm{PL}} \propto (\text{Surface-shell volume}) \times f(\text{structure}) \tag{5.1}$$

where I_{PL} is the area of the blue band, and f(structure) is a function that takes into account the effects of the differences in the SiO_2 matrix of each particle.

Considering that the surface-shell volume term is linearly dependent on S up to S=300 m^2/g and then it is constant, it is deduced that f(structure) should be proportional to $S^{0.7}$, to justify the observed $S^{1.7}$ dependence of I_{PL}. The determined monotonic dependence of the structural function on S is in agreement with the results of the Raman measurements, which show that the density of the nanoparticles linearly increases with S and, as a consequence, a monotonic increase of the creation efficiency of the defects could be expected.

5.3 Investigation by EPR spectroscopy of the structural properties of fumed silica

In this section, we report investigation by EPR spectroscopy on fumed silica whose results corroborate the shell-like model suggested in the previous sections. In particular, we studied the creation efficiency of the E'$_\gamma$ centers in the different fumed silica types, β-ray irradiated at a dose of 400 kGy.

In all of the fumed silica types, no EPR signals were detected before irradiation. At variance, in the irradiated materials a weak signal ascribed to the main resonance line of the E'$_\gamma$ center was detected. In Figure 5.21, the FH-EPR spectrum acquired for the AE90 fumed silica type is shown. The spectrum acquired for the SDC/0 sample β-ray irradiated at 90 kGy (the same spectrum of Figure 4.6) is displayed for comparison. The fumed silica sample spectrum is characterized by a very low signal-to-noise ratio as compared with that of bulk sample and shows a line shape similar enough to the common L2 line of bulk materials. These findings are qualitatively in agreement with the previous works, in which the VUV irradiation on the AE380 fumed silica type was able to induce only a very low concentration of E'$_\gamma$ centers (see Section 1.3) [37, 81].

In order to enhance the signal-to-noise ratio in the fumed silica samples, we acquired the main resonance line of the E'$_\gamma$ center by SH-EPR method. The normalized spectra for different fumed silica types and SDC/0 sample are reported in Figure 5.22.

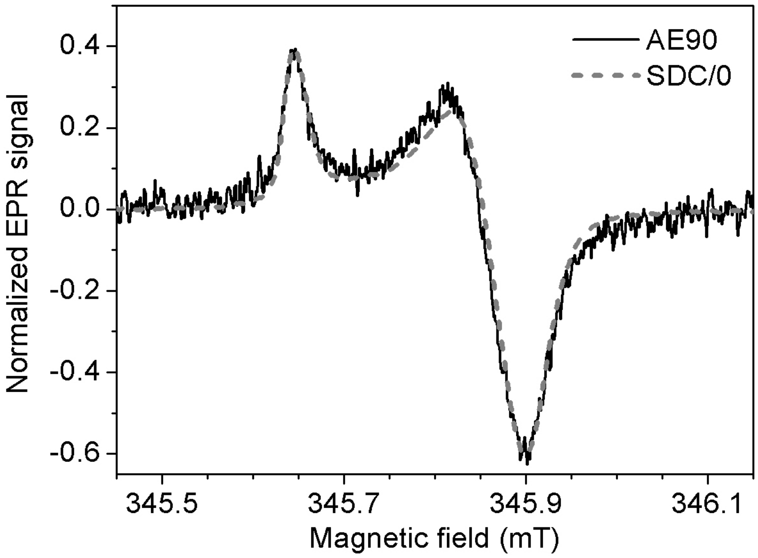

Figure 5.21: FH-EPR spectra of the E'$_\gamma$ center main resonance line acquired for AE90, β-rays irradiated at 400 kGy, and SDC/0 sample, β-rays irradiated at 90 kGy. The spectra are normalized to the peak-to-peak signal amplitude.

No evident changes are observed in the line shape among the fumed silica types considered, whereas just a little difference at about 346.1 mT can be recognized between the fumed silica types and the SDC/0 spectra.

Since the concentration of the E'$_\gamma$ centers was too low in some fumed silica types for the signal being detectable by FH-EPR measurements, we used SH-EPR signals reported in Figure 5.22 to estimate concentration as discussed in Section 3.3.2. The concentration of the E'$_\gamma$ centers as a function of the specific surface for each fumed silica type is shown in Figure 5.23. The data show that the E'$_\gamma$ centers concentration decreases on increasing the specific surface. It is important to note that the low concentration of this point defect in fumed silica does not allow to detect the strong hyperfine structure of the E'$_\gamma$ center. Indeed as discussed before the intensity of this latter signal is much lower than that of the main resonance line of the E'$_\gamma$ center.

5.3.1 Discussion

The spectra reported in Figures 5.21 and 5.22 show that the main resonance line of the E'$_\gamma$ center is independent of the different nanometric nature of each fumed

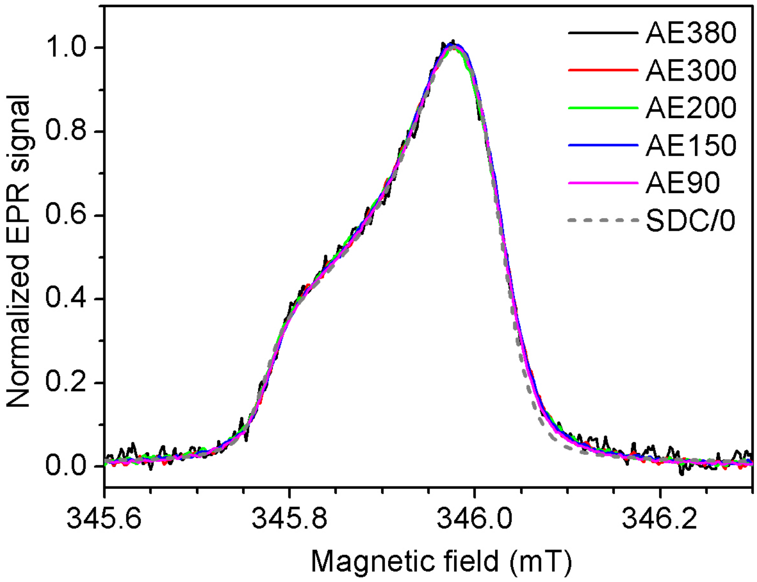

Figure 5.22: Normalized SH-EPR spectra of the E'$_\gamma$ center main resonance line acquired for different fumed silica types, β-rays irradiated at 400 kGy, and SDC/0 sample, β-rays irradiated at 90 kGy.

silica type. Indeed the line shape is the same for all the fumed silica types and it is characterized by an orthorhombic line typically observed in the bulk silica materials irradiated at high doses (L2 line shape). On the other hand, the data shown in Figure 5.23 suggest that the creation efficiency of the E'$_\gamma$ centers strongly depends on the considered fumed silica type and that a direct correlation between the E'$_\gamma$ center concentration and the specific surface exists. In this context, if one supposes that the E'$_\gamma$ centers were induced by irradiation in the whole volume of each fumed silica particle, obviously the concentration of the E'$_\gamma$ centers should be independent of the particle size and then it should be the same in all the fumed silica types. However, the data reported in Figure 5.23 clearly disagree with this supposition. In order to interpret our findings, we assume that the E'$_\gamma$ centers can be induced only in a portion of the particle volume. In particular, considering the shell-like model above discussed (see Sections 5.1.1 and 5.2.1) and in agreement with the previous investigations by EPR technique on AE380 fumed silica [37, 81], we suggest that the E'$_\gamma$ centers are induced mainly in the core-shell. On the basis of this condition the

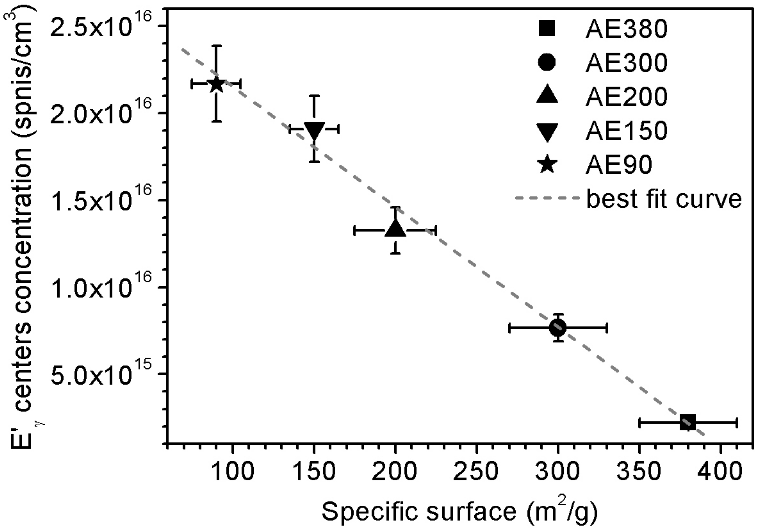

Figure 5.23: The concentration of the E'$_\gamma$ centers, estimated in each fumed silica type β-rays irradiated at 400 kGy, as a function of the specific surface. The dashed line is the best fit curve discussed in the text.

expected concentration in each fumed silica type can be written as:

$$C_{E'_\gamma} = k\frac{V_{CS}}{m_p} \tag{5.2}$$

where k is a constant, V_{CS} is the volume of the core-shell and m_p is the particle's mass. Substituting $V_{CS} = V_{particle} - V_{SS}$, being $V_{particle}$ and V_{SS} the volume of the whole particle and the surface-shell volume, respectively, and considering that $\frac{V_{SS}}{m_p} \sim \delta \times S$ with S the specific surface and δ the thickness of the surface-shell, Equation 5.2 can be rewritten as follows:

$$C_{E'_\gamma}(S) \sim k\left(\frac{1}{\rho} - \delta \times S\right) \tag{5.3}$$

where ρ is the mean density of the particle.

ρ can be considered constant as compared with the variation of $C_{E'_\gamma}$ and S. Indeed, these latter change of about one order of magnitude (see Figure 5.23), whereas ρ, as discussed in Section 5.1, changes only up to 10 ÷ 20 % in all the fumed silica types. We fitted the experimental data reported in Figure 5.23 with Equation 5.3, where k/ρ and $k \times \delta$ were considered fit parameters. The good agreement between the best fit curve (the grey dashed line) and the experimental data confirms the initial supposition: the fumed silica particles can be described in terms of the shell-like model, where the E'$_\gamma$ centers are induced mainly in the core-shell.

From the intercept value $C_{E'_\gamma}(0) = k/\rho = (2.8 \pm 0.6) \times 10^{16}$ spins/cm^3, important information can be obtained. Indeed, considering that this value is comparable with the typical concentration of the E'$_\gamma$ centers induced in bulk silica materials and that the intercept represents the concentration induced only in the core-shell, our data suggest that the radiation sensitivity of the network of the core-shell and bulk silica materials are similar. In this context, it is important to note that previous works on the AE380 attributed the radiation resistance of fumed silica to the oxygen excess in the particles [37, 81–83] (see Section 1.3.3). However, in disagreement with these latter works, our findings strongly suggest that the radiation resistance of fumed silica is only due to the fact that stable E'$_\gamma$ centers can not be induced into the surface-shell of each particle. Besides, in order to confute the role of the oxygen in this mechanism, we verified that the O_2 content in fumed silica types increases on decreasing the specific surface[c]. In other words, the O_2 content is higher in the fumed silica types characterized by higher concentration of E'$_\gamma$ centers.

Another information that we extracted from the fit is the thickness of the surface-shell: $\delta \sim 1$ nm. The reasonableness of this value, considering that the fumed silica particles have a mean diameter from 7 to 40 nm, further corroborates our interpretation. It is worth noting that to our knowledge an experimental estimation of δ is lacking up to now. Indeed, as discussed before, only few simulative works estimated this thickness to be about 0.2÷0.3 nm.

---

[c] We estimated the different O_2 contents in the fumed silica types by the investigation of the Raman line peaked at about 1550 cm^{-1} (not reported here), which is attributed to the luminescence activity of the O_2 molecules embedded into the silica network excited by the IR laser source of the used Raman spectrometer [139].

Conclusions and suggestions for further investigations

In this Thesis we reported an experimental investigation on the structural properties of the silica network and on their modifications induced by thermal treatments. These studies were carried out by using two kinds of silica systems: bulk and fumed silica. In the former case, a wide set of bulk silica materials (both natural and synthetic) differing in the production methods and in the impurities content was considered. In the second case, six fumed silica types, characterized by different mean diameters of the silica nanoparticles, from 7 to 40 nm, corresponding to specific surface from 380 to 50 m^2/g, were used. We primarily used the Raman and EPR techniques; however, important information related to the structural properties of the silica network were also obtained by IR and time resolved photoluminescence measurements.

In the following, we summarize the main results we obtained and their interpretations, whereas in the last part of this section some suggestions for future investigation on the considered topics will be proposed.

The strong hyperfine structure of the E'_γ center, probing the local arrangement of the silica network in the range-II order was investigated by EPR spectroscopy in a set of various bulk silica materials of different commercial origin, γ-ray irradiated in the dose range 0.1÷100 kGy (see Section 4.1). Concomitantly, by Raman spectroscopy we studied the D_1 and D_2 lines probing mean features of the silica network in the range-III order. Our study allowed us to point out that the splitting of the strong hyperfine structure, as well as the amplitude of the D_2 Raman line, show a relevant material-to-material variability. Notwithstanding, we showed for the first time that these two experimental features, and consequently the structural properties of the range-II and -III orders, are intimately related to each other independently of the material type (natural or synthetic), production method and impurity content, as for example OH groups.

In order to deepen the relation between the properties of the range-II and -III orders of the silica network, we gradually modified the structural properties of a given bulk silica material, by isothermal treatments at 1000 °C from few up to hundreds minutes (see Section 4.2). Probing again the splitting of the E'_γ center strong hyperfine structure and the amplitude of the D_2 Raman line in different treated samples, β-ray irradiated at 90 kGy, we showed that the changes of these features induced by thermal treatments not only occur in a correlated way but, moreover, they have the same data trend that characterizes the different untreated bulk silica materials before investigated. These results, from one hand, further corroborate the conclusion that the structural properties of the range-II and -III orders of the bulk silica network are related to each other and, from the other, demonstrate that these properties strongly depend on the history of the material. Our findings, besides to shed light on the structural modification mechanisms of the bulk silica materials, may play an important role from a more applicative point of view, because they should be useful to check and produce bulk silica samples with specific structural features. To further explore these topics, it could be interesting to extend the investigation to different temperature ranges. This can elucidate what specific “driving force” governs the structural modifications and to what extent the range-II and -III order interconnection holds.

As regards the fumed silica, in Section 5.1 we clearly evidenced that all the considered types of this material are characterized by Raman features (R-, D_1 and D_2 lines) extremely different from those observed in the bulk silica materials. In particular, these differences are much more pronounced on increasing the specific surface or, in other words, on decreasing the primary particles size. These findings, ascribed to a structural network of each fumed silica nanoparticle more stressed than that of bulk silica, allowed us to point out that a direct relation between the uncommon properties of fumed silica and their nanometric nature exists.

By isochronal thermal treatments of two hours in the range 100÷1000 °C, we found that the differences between the Raman spectra of fumed and bulk silica are removed for the R-line, whereas they become more pronounced for the D_2 line. We showed that our results can be interpreted in terms of a shell-like structural model of the particles. In this scheme, a surface-shell, characterized by strong structural strains, and a core-shell, with a network more relaxed but in any case different from that of bulk silica, exist for each particle.

It is worth noting that a structural difference for the surface and inner part of the silica nanoparticles was previously suggested by few simulative and experimental works [39, 40, 81]; however, for the first time we described in details this model, proved its validity and proposed a simple explanation of the reason for which the network of a primary particle organizes itself in a shell-like structure. By this model, we pointed out that the thermal treatments modify in different ways the core- and surface-shell. Indeed, the structural modifications of the core-shell start to relax for $T \geq T^{\star}$, where $T^{\star} \leq 700$ °C depends on the fumed silica type. At T=1000 °C, the network of this part of the particles appears the same in all the fumed silica types and is consistent with that of bulk silica materials (the strains are completely relaxed). On the other hand, the initial strong structural strains of the surface-shell do not relax in the range of the considered temperatures; on the contrary, they become more marked around $T \sim 700$ °C. We ascribed this effect to the formation of small-membered rings, originated by the mutual interaction of surface silanol groups. Under this scheme, we suggest that the sintering effects (build up of particle-to-particle linking) could take place only for $T \geq 700$ °C and do not modify the whole volume of the particle but only the surface-shell.

The validity of the shell-like model was further corroborated by the investigation of the blue luminescence band of the fumed silica (see Section 5.2). We found that the amplitude of this signal, excited in a wide energy range from the visible up to UV and characterized by a lifetime of ns order, increases with the specific surface. Considering that the blue band has never been found in bulk silica materials, our results evidence for the first time the existence of an intrinsic relation of this emission activity with the size of the silica nanoparticles. In particular, this result allowed us to point out that the amplitude of the blue band arises from two different contributions: a geometrical one, related to the fact that the point defects responsible for the blue emission are mainly localized into the surface-shell, and a structural one, strictly connected with the different structural properties of each fumed silica type. For this latter contribution, we suggest that these luminescence point defects are induced in the surface-shell more efficiently in the samples having a more strained structure, that is the fumed silica types characterized by a smaller size of the particles.

Moreover, by the study of the emission as a function of the excitation energy as well, as of the PL decay monitored at different emission energies, an uncommon wide inhomogeneity of the blue band was evidenced. This emission property makes the silica nanoparticles an extremely versatile system both for basic studies of inhomogeneity effects in solid systems and for several optical applications such as down converter displays.

Finally, the shell-like model was successful in the explanation of the induction resistance of the E'$_\gamma$ centers by irradiation of the fumed silica. Indeed, as discussed in Section 5.3, we unambiguously demonstrated that the low concentration of these point defects is not due to the oxygen excess in the particles, as suggested in some works [37, 81–83], but it is originated from the fact that the stable E'$_\gamma$ centers are induced mainly in the core-shell and the (core-shell volume)/(surface-shell volume) ratio decreases on increasing the specific surface. This conclusion arises from the observation that the E'$_\gamma$ center concentration linearly decreases on increasing the specific surface. Besides, by simple considerations we obtained that the radiation sensitivity of the network of the core-shell is similar to that of the bulk silica materials.

Some of the possible interesting future extensions of this Thesis work could be the exposure of the fumed silica to higher irradiation doses than those considered here, in order to induce a sufficient concentration of E'$_\gamma$ centers. This should make detectable its strong hyperfine structure and should allow to check the correlation between range-II and -III order properties in these materials. Furthermore, it would be intriguing to study the structural modifications induced by irradiation, already evidenced for bulk silica materials but never investigated in nanometric materials. The effects of irradiation are also interesting in order to investigate the formation of point defects and their connection with emission properties of fumed silica. Another argument of research could be the investigation of the structural properties and their modifications by thermal treatments of the fumed silica permanently densified. Finally, it would be interesting to elucidate the point defect responsible for the blue band, whose origin is still debated, and to study its radiation sensitivity in view of possible applications. Overall the future investigations should let to extend the knowledge already acquired in bulk silica materials to nanometric ones and to shed light on their analogies and differences both on basic and applicative aspects.

Bibliography

[1] Desa, J. A. E., Wright, J., Wong, J., and Sinclair, R. N. *J. Non-Cryst. Solids* **51**, 57 (1982).

[2] Pacchioni, G., Skuja, L., and Griscom, D. L., editors. *Defects in SiO_2 and Related Dielectrics: Science and Technology.* Kluwer Academic, Dordrecht, (2000).

[3] Devine, R. A. B., Duraud, J. P., and Dooryhe, E., editors. *Structure and Imperfections in Amorphous and Crystalline Silicon Dioxide.* John Wiley and Sons, New York, (2000).

[4] Wyckoff, R., editor. *Crystal Structures.* Interscience, New York, (1951).

[5] Clark, T. M., Grandinetti, P. J. Florian, P., and Stebbis, J. F. *Phys. Rev. B* **70**, 064202 (2004).

[6] Mozzi, R. L. and Warren, B. E. *J. Appl. Cryst.* **2**, 164 (1969).

[7] Zachariesen, W. H. *J.Am. Chem. Soc.* **54**, 3841 (1932).

[8] Zallen, R., editor. *The physics of amorphous solids.* Wiley-Interscience, New York, (1983).

[9] Neuefeind, J. and Liss, K. D. *Ber. Bunsenges Phys. Chem.* **100**, 1341 (1996).

[10] Yuan, X. and Cormack, A. N. *J. Non-Cryst. Solids* **319**, 31 (2003).

[11] Warren, B. E., Krutter, H., and Morningstar, O. *J. Am. Ceram. Soc.* **19**, 202 (1936).

[12] Nalwa, H. S., editor. *Silicon-based materials and devices.* Academic Pres, USA, (2001).

[13] Uchino, T. *Journal of Ceramic Society of Japan* **113**, 17 (2005).

[14] Susman, S., Volin, K. J., Price, D. L., Grismditch, M., Rino, J. P., Kalia, L. K., Vashishta, P Gwanmesia, G., Wang, Y., and Liebermann, R. C. *Phys. Rev. B* **43**, 1194 (1991).

[15] Hehlen, B. *J. Phys.: Condens. Matter* **22**, 025401 (2010).

[16] Devine, R. A. B., Arndt, J., Farnan, I., and Capponi, J. J. *Phys. Rev. B* **35**, 2560 (1987).

[17] Rino, J. P., Ebbsjö, I., Halia, R. K., Nakano, A., and Vashishta, P. *Phys. Rev. B* **47**, 3053 (1993).

[18] Pasquarello, A. and Car, R. *Phys. Rev. Lett.* **80**, 5145 (1998).

[19] Giacomazzi, L., Umari, P., and Pasquarello, A. *Phys. Rev. B* **79**, 064202 (2009).

[20] Galeener, F. L. *Solid State Commun.* **44**, 1037 (1982).

[21] Burgin, J., Guillon, C., Langot, P., Valle, F., Hehlen, B., and Foret, M. *Phys. Rev. B* **78**, 184203 (2008).

[22] Agarwal, A., Davis, M. K., and Tomozawa, M. *J. Non-Cryst. Solids* **185**, 191 (1995).

[23] Galeener, F. L. *Phys. Rev. B* **19**, 4292 (1979).

[24] Kakiuchida, H., Saito, K., and Ikushima, A. J. *J. Appl. Phys.* **93**, 777 (2003).

[25] Tomozawa, M., Hong, J. W., and Ryu, S. R. *J. Non-Cryst. Solids* **351**, 1054 (2005).

[26] Pratsinis, S. E. *Prog. Energy Combust. Sci.* **24**, 197 (1998).

[27] Stark, W. J. and Pratsinis, S. E. *Powder Technol.* **126**, 103 (2002).

[28] Lu, Y., Yin, Y., Li, Z. Y., and Xia, Y. *Nanoletters* **2**, 785 (2002).

[29] Park, J. H., Gu, L., von Maltzahn, G., Ruoslahti, E., Bhatia, S., and Sailor, M. *Nature Mat.* **8**, 331 (2009).

[30] Abe, I., Sato, K., Abe, H., and Naito, M. *Adv. Powder Technol.* **19**, 311 (2008).

[31] Brune, H., Ernst, H., Grnwald, A., Grnwald, W., Hofmann, H., Krug, H., Janich, P., Mayor, M., Rathgeber, W., Schmid, G., Simon, U., Vogel, V., and Wyrwa, D., editors. *Nanotechnology, Assessment and Perspectives.* Springer, Berlin Heidelberg, (2006).

[32] Aitken, R. J., Creely, K. S., and Tran, C. L., editors. *Nanoparticles: an occupational hygiene review.* Sudbury, Suffolk, Grande-Bretagne, (2004).

[33] Kohler, M. and Fritzsche, W., editors. *Nanotechnology, An Introduction to nanostructuring techniques.* Weinheim, Germany, Wiley-VCH, (2004).

[34] Holister, P., editor. *Nanotech: the tiny revolution.* [S.l.] Cientifica, (2002).

[35] Tan, W. H., Wang, K. M., He, X. X., Zhao, X. J., Drake, T., Wang, L., and Bagwe, R. P. *Med. Res. Rev.* **24**, 621 (2004).

[36] Ruan, W. H., Huang, X. B., Wang, X. H., Rong, M. Z., and Zhang, M. Q. *Macromol. Rapid Commun.* **27**, 581 (2006).

[37] Stesmans, A., Clémer, K., and Afanas'ev, V. V. *Phys. Rev. B* **72**, 155335 (2005).

[38] Uchino, T., Aboshi, A., Yamada, T., Inamura, Y., and Katayama, Y. *Phys. Rev. B* **77**, 132201 (2008).

[39] Roder, A., Kob, W., and Binder, K. *J. Chem. Phys.* **114**, 7602 (2001).

[40] Schweigert, I. V., Lehtinen, K. E. J., Carrier, M. J., and Zachariah, M. R. *Phys. Rev. B* **65**, 235410 (2002).

[41] Hoang, V. V. *J. Phys. Chem. B* **111**, 12649 (2007).

[42] Yamada, T., Nakajima, M., Suemoto, T., and Uchino, T. *J. Phys. Chem. C* **111**, 12973 (2007).

[43] Awazua, K. and Kawazoe, H. *J. Appl. Phys.* **94**, 6243 (2003).

[44] Uchino, T., Aboshi, A., Kohara, S., Ohishi, Y., Sakashita, M., and Aoki, K. *Phys. Rev. B* **69**, 155409 (2004).

[45] Hemley, R. J., Mao, H. K., Bell, P. M., and Mysen, B. O. *Phys. Rev. Lett.* **57**, 747 (1986).

[46] Grimsditch, M. *Phys. Rev. Lett.* **52**, 2379 (1984).

[47] Uchino, T., Sakoh, A., Azuma, M., Kohara, S., Takahashi, M., Takano, M., and Yoko, T. *Phys. Rev. B* **67**, 092202 (2003).

[48] Kittel, C., editor. *Introduction to Solid State Physics.* John Wiley and Sons, New York, (1981).

[49] Balanzat, E. and Bouffard, S., editors. *in Materials under irradiation, Eds. Dunlop A., Rullier-Albenque F., Jaouen C., Templier C. and Davenas J.* Trans Tech Publications Ltd pag.7, (1993).

[50] Brukner, R. *J. Non-Cryst. Solids* **5**, 281 (1971).

[51] Brukner, R. *J. Non-Cryst. Solids* **5**, 123 (1970).

[52] Hetherinton, G. and Jack, K. H. *Phys. Chem. Glasses* **3**, 129 (1962).

[53] Arnold, G. W. and Compton, W. D. *Phys. Rev.* **116**, 802 (1959).

[54] Bergna, H. E., editor. *The Colloid Chemistry of Silica. In Advances in Chemistry Series.* JAmerican Chemical Society: Washington DC, Vol. 234, (1994).

[55] Burneau, A., Barrès, O., Gallas, J. P., and Lavalley, J. C. *Langmuir* **1364**, 6 (1990).

[56] Plotnichenko, V. G., Sokolov, V., and Dianov, E. *J. Non-Cryst. Solids* **261**, 186 (2000).

[57] Wang, R. and Wunder, S. L. *Langmuir* **16**, 5008 (2000).

[58] Zhuravlev, L. T. *Colloids Surf. A* **173**, 1 (2000).

[59] Gallas, J. P., Goupil, J. M., Vimont, A. Lavalley, J. C., Gil, B., Gilson, J. P., and Miserque, M. *Langumir* **25**, 5825 (2009).

[60] Anedda, A., Carbonaro, C. M., Clemente, F., Corpino, R., and Ricci, P. C. *J. Phys. Chem. B* **107**, 13661 (2003).

[61] Davis, K. M. and Tomozawa, M. *J. Non-Cryst. Solids* **201**, 177 (1996).

[62] Uchino, T., Kurumoto, N., and Sagawa, N. *Phys. Rev. B* **73**, 233203 (2006).

[63] Aboshi, A., Kurumoto, N., Yamada, T., and Uchino, T. *J. Phys. Chem. C* **111**, 8483 (2007).

[64] Kurumoto, N., Yamada, T., and Uchino, T. *J. Non-Cryst. Solids* **353**, 684 (2007).

[65] Yamada, T. and Uchino, T. *Appl. Phys. Lett.* **87**, 081904 (2005).

[66] Uchino, T. and Yamada, T. *Appl. Phys. Lett.* **85**, 1164 (2004).

[67] Glinka, Y. D. *Phys. Rev. B* **66**, 035404 (2002).

[68] Glinka, Y. D. *Phys. Rev. B* **62**, 4733 (2000).

[69] Wright, A. C. in Pacchioni, G., Skuja, L., and Griscom, D. L., editors. *Defects in SiO_2 and Related Dielectrics: Science and Technology.* Kluwer Academic, (2004).

[70] Silsbee, R. H. *J. Appl. Phys.* **32**, 1459 (1961).

[71] Griscom, D. L. *Phys. Rev. B* **20**, 1823 (1979).

[72] Boero, M., Pasquarello, A., Sarnthein, J., and Car, R. *Phys. Rev. Lett.* **78**, 887 (1997).

[73] Agnello, S., Boscaino, R., Buscarino, G., Cannas, M., and Gelardi, F. M. *Phys. Rev. B* **66**, 113201 (2002).

[74] Kneubuhl, F. K. *J. Chem. Phys.* **1074**, 1960 (1960).

[75] Mashkov, V. A., Austin, W. R., Zhang, L., and Leisure, R. G. *Phys. Rev. Lett.* **76**, 2926 (1996).

[76] Devine, R. A. B. *Phys. Rev. B* **35**, 9783 (1987).

[77] Devine, R. A. B. and Arndt, J. *Phys. Rev. B* **35**, 9376 (1987).

[78] Griscom, D. L. *Nucl. Instr. Meth. Phys. Res. B* **1**, 192 (1984).

[79] Griscom, D. L. *Phys. Rev. B* **51**, 4192 (1980).

[80] Pacchioni, G. and Vitiello, M. *Phys. Rev. B* **58**, 7745 (1998).

[81] Clémer, K., Stesmans, A., and Afanas'ev, V. V. *Mater. Science and Eng. C* **26**, 766 (2006).

[82] Stesmans, A., Clémer, K., and Afanas'ev, V. V. *J. Phys.: Condens. Matter* **17**, 393 (2005).

[83] Stesmans, A., Clémer, K., and Afanas'ev, V. V. *J. Non-Cryst. Solids* **351**, 1764 (2005).

[84] Warren, W. L., Poindexter, E. H., Offenberg, M., and Müller-Warmuth, W. *J. Electrochem. Soc.* **139**, 872 (1992).

[85] Uchino, T., Takahashi, M., and Yoko, T. *Phys. Rev. Lett.* **86**, 5522 (2001).

[86] Lu, Z. Y., Nichlaw, C. J., Fleetwood, D. M., Schrimpf, R. D., and Pantelides, S. T. *Phys. Rev. Lett.* **98**, 285505 (2002).

[87] Stesmans, A., Clémer, K., and Afanas'ev, V. V. *Phys. Rev. B* **77**, 094130 (2008).

[88] Stesmans, A., Clémer, K., and Afanas'ev, V. V. *J. Non-Cryst. Solids* **354**, 233 (2008).

[89] Nakamoto, N., editor. *Infrared and Raman spectra of inorganic and coordination compounds*. J. Wiley and Sons, Inc., (1997).

[90] Ferraro, J. R., Nakamoto, K., and Brown, C. W., editors. *Infrared and Raman spectra of inorganic and coordination compounds*. Academic Press, (2003).

[91] *Molecular spectra and molecular structure*. Van Nostrand, Princeton, NJ, (1945).

[92] Harris, D. C. and Bertolucci, M. D., editors. *The physics of amorphous solids*. Oxford University Press, New York, (1978).

[93] Bransden, B. and Joachain, C. J., editors. *Physics of atoms and molecules*. Addison Wesley Longman limited, (1983).

[94] Weissbluth, M., editor. *Atoms and molecules*. Academic Press, New York, (1978).

[95] Cohen-Tannoudji, C., Dupont-Roc, J., and Grynberg, G., editors. *Atom-photon interactions*. John Wiley and Sons, New York, (1992).

[96] *Infra-red Spectroscopy and Molecular Structure*. Elsevier Publishing Company, Amsterdam, (1963).

[97] Abragam, A. and Bleaney, B., editors. *Electron paramagnetic resonance of transition ions*. Clarendon, Oxford, (1970).

[98] Pake, G. E. and Estle, T. L., editors. *The physical principles of electron paramagnetic resonance*. W.A. Benjamin Inc., Massachussets, (1973).

[99] Weil, J. A., Bolton, J. R., and Wertz, J. E., editors. *Electron Paramagnetic Resonance*. John Wiley and Sons Inc., New York, (1994).

[100] Poole, C. P., editor. *Electron Spin Resonance*. John Wiley and Sons Inc., New York, (1967).

[101] Slichter, C. P., editor. *Principles of magnetic resonance*. Sprinlger-Verlag, Berlin Heidelberg, (1978).

[102] Bloch, F. *Phys. Rev.* **70**, 460 (1946).

[103] Weger, M. *Bell. Syst. Tech. J.* **39**, 1013 (1960).

[104] *Introduction to Molecular Spectroscopy.* McGraw-Hill, (1962).

[105] *Theory and applications of UV spectroscopy.* J. Wiley ans Sons, New York, (1970).

[106] Williams, G. and Watts, D. C. *Trans. Faraday Soc.* **66**, 80 (1970).

[107] Ngai, K. L. *Comments Solid State Phys.* **9**, 127 (1979).

[108] Hetherington, G. *J. Brit. Ceram. Soc.* **3**, 595 (1966).

[109] Basic Characteristics of Aerosil, 4^{th} ed., Degussa, Frank-furt (2001).

[110] Evonik industries online catalog (2010).

[111] Barthel, H., Heinemann, M., Stintz, M., and Wessely, B. *Part. Part. Syst. Charact.* **16**, 169 (1999).

[112] Ferch, H. and Seibold, K. *Farbe and Lack* **90**, 88 (1986).

[113] Mironyuk, I. F., Gunko, V. M., Turov, V. V., Zarko, V. I., Leboda, R., and Skubiszewska-Zieba, J. *Colloids and Surfaces A: Physicochemical and Engineering Aspects* **180**, 87 (2001).

[114] Buscarino G. *PhD Thesis*, Dipartimento di Scienze Fisiche ed Astronomiche, Università degli Studi di Palermo (Italy), (2007).

[115] Buscarino, G., Agnello, S., Gelardi, F. M., and Boscaino, R. *Phys. Rev. B* **80**, 094202 (2009).

[116] Agnello, S., Boscaino, R., Cannas, M., and Gelardi, F. M. *Phys. Rev. B* **64**, 174423 (2001).

[117] García, R. and Pérez, R. *Surf. Sci. Rep.* **47**, 197 (2002).

[118] Giessibl, F. J. *Rev. Mod. Phys.* **75**, 949 (2003).

[119] Seo, Y. and Jhe, W. *Rep. Prog. Phys.* **71**, 016101 (2008).

[120] Buscarino, G., Vaccaro, G., Agnello, S., and Gelardi, F. M. *J. Non-Cryst. Solids* **355**, 1092 (2009).

[121] Vaccaro, G., Buscarino, G., Agnello, S., Messina, G., Carpanese, M., and Gelardi, F. *Eur. Phys. J. B* **76**, 197 (2010).

[122] Geissberger, A. E. and Galeener, F. *Phys. Rev. B* **28**, 3266 (1983).

[123] Buscarino, G., Agnello, S., and A. Parlato, A. *Phys. Stat. Sol. (c)* **4**, 1301 (2007).

[124] Tsai, T. E. and Griscom, D. L. *J. Non-Cryst. Solids* **91**, 160 (1987).

[125] Vella, E. and Boscaino, R. *Phys. Rev. B* **79**, 085204 (2009).

[126] Shin, D. and Tomozawa, M. *J. Non-Cryst. Solids.* **203**, 262 (1996).

[127] Vaccaro, G., , Agnello, S., Buscarino, G., and Gelardi, F. *J. Phys. Chem. C* **114**, 13991 (2010).

[128] Vaccaro, L., Vaccaro, G., Agnello, S., Buscarino, G., and Cannas, M. *Solid State Commun.* **150**, 2278 (2010).

[129] Vaccaro, G., Agnello, S., Buscarino, G., Cannas, M., and Vaccaro, L. *in press on J. Non-Cryst. Solids* .

[130] Buscarino, G., Ardizzone, V., Vaccaro, G., Agnello, S., and Gelardi, F. M. *J. Appl. Phys.* **108**, 074314 (2010).

[131] Morrow, B. A. and McFarlan, A. J. *J. Phys. Chem.* **96**, 1395 (1992).

[132] Wang, L. S., Nicholas, J. B., Dupuis, M., Wu, H., and Colson, S. D. *Phys. Rev. Lett.* **78**, 4450 (1997).

[133] Harkless, J. A. W., Stillinger, D. K., and Stillinger, F. H. *J. Phys. Chem.* **100**, 1098 (1996).

[134] Xu, C., Wang, W., Zhang, W., Zhuang, J., Liu, L., Kong, Q., Zhao, L., Long, Y., Fan, K., Qian, S., and Li, Y. *J. Phys. Chem. A* **104**, 9518 (2000).

[135] Inai, S., Harao, A., and Nishikawa, H. *J. Non-Cryst. Solids* **353**, 510 (2007).

[136] Young, G. J. *Journ. Colloid Sci.* **13**, 67 (1958).

[137] Zhuravlev, L. T. *Langmuir* **3**, 316 (1987).

[138] Hosono, H., Ikuta, Y., Kinoshita, T., Kajihara, K., and Hirano, M. *Phys. Rev. Lett.* **87**, 175501 (2001).

[139] Skuja, L. and Guttler, B. *Phys. Rev. Lett.* **77**, 2093 (1996).

List of related papers

1. G. Vaccaro, S. Agnello, G. Buscarino, L. Nuccio, S. Grandi and P. Mustarelli, " ^{29}Si attribution of the 1.3 mT hyperfine structure of the E'$_\gamma$ centers in amorphous SiO_2"
   J. of Appl. Phys., **105**, (2009), 093514.

2. G. Buscarino, G. Vaccaro, S. Agnello and F. M. Gelardi, "Variability of the SiOSi angle in amorphous SiO_2 probed by electron paramagnetic resonance and Raman spectroscopy"
   J. Non-Cryst. Solids, **355**, (2009), 1092.

3. G. Vaccaro, G. Buscarino, S. Agnello, G. Messina, M. Carpanese, and F. M. Gelardi, "Structural properties of the range-II and range-III order in amorphous SiO_2 probed by electron paramagnetic resonance and Raman spectroscopy"
   Europ. Phys. J. B, **76**, (2010), 197.

4. G. Vaccaro, S. Agnello, G. Buscarino, and F. M. Gelardi, "Thermally Induced Structural Modification of Silica Nanoparticles Investigated by Raman and Infrared Absorption Spectroscopies"
   J. Phys. Chem. C, **114**, (2010), 13991.

5. G. Buscarino, V. Ardizzone, G. Vaccaro, S. Agnello and F. M. Gelardi, "Atomic force microscopy and Raman investigation on the sintering process of amorphous SiO_2 nanoparticles"
   J. Appl. Phys., **108**, (2010) 074314.

6. L. Vaccaro, G. Vaccaro, S. Agnello, G. Buscarino and M. Cannas, "Wide range excitation of visible luminescence in nanosilica"
   Solid State Commun. **150**, (2010) 2278.

7. G. Vaccaro, S. Agnello, G. Buscarino, M. Cannas, L. Vaccaro, "Structural and luminescence properties of amorphous SiO_2 nanoparticles"
   in press on *Journal of Non-Crystalline Solids.*

8. G. Buscarino, V. Ardizzone, G. Vaccaro, and F. M. Gelardi, "Sintering process of amorphous SiO_2 nanoparticles investigated by AFM, IR and Raman techniques"
   in press on *J. Non-Cryst. Solids.*

Acknowledgments

It is hard to find the right words to express my thanks to the people who have been very helpful to me both from scientific and human point of view during this three years; I hope to not forget anyone.

First of all, I would like to express my sincere gratitude to Dr. Simonpietro Agnello, who has been my supervisor since my Master's Thesis. He not only provided me with many helpful suggestions, important advices and constant encouragement during all the time of the course of this work, but he also shared with me his experience and enthusiasm for research, improving my scientific consciousness.

I am also indebted to Dr. Gianpiero Buscarino for all the time he spent with me during the innumerable scientific discussions we had and for the fundamental contribute that he gave to my research activity as well as for proofreading my thesis.

I would like to express my gratitude to Prof. Franco Mario Gelardi for his relevant hints in the preparation of many scientific activities.

Special gratitude goes to Dr. Lavinia Vaccaro and Prof. Marco Cannas not only for stimulating and useful discussions but also for their contribute in the time resolved luminescence experiments.

I would like to thank Prof. Roberto Boscaino for his irreplaceable role as head of the Laboratory of Amorphous Materials Physics (LAMP). During the numerous meetings he shared his vast knowledge and experience with all the members of the research group.

Also many tanks go to the other members of the LAMP group for the stimulating discussions and numerous ideas: Antonino Alessi, Michele DAmico, Fabrizio Messina, Eleonora Vella, Giovanna Navarra and Laura Nuccio.

I thank also Prof. Maria Li Vigni for proofreading this thesis and for her critical comments and corrections. I am also grateful to Prof. Takashi Uchino who has reviewed this work.

I am grateful to Gianluca Napoli and Giacomo Tricomi for the technical assistance

during my experiments. I also thank E. Calderaro and A. Parlato of the "Dip. di Ingegneria Nucleare" of Palermo for taking care of the γ-ray irradiations, R. M. Montereali and G. Messina for the β-ray irradiations at the Frascati Reaserch Centre of the ENEA and D. G. Sporea for the β-ray irradiations of the National Institute for Laser, Plasma and Radiation Physics of Magurele, Romania.

Finally, I would like to express my heartiest thanks to my family and friends for encouragement during these years, without whom this work would have been impossible.

Gianfranco